Copyright

by

Ian Seth Ladner

2018

The Dissertation Committee for Ian Seth Ladner Certifies that this is the approved version of the following Dissertation:

MECHANICAL CHARACTERIZATION OF TWO-PHOTON POLYMERIZATION SUBMICRON FEATURES

Committee:

Michael A. Cullinan, Supervisor

Sourabh K. Saha

Wei Li

Kenneth M. Liechti

Carolyn C. Seepersad

MECHANICAL CHARACTERIZATION OF TWO-PHOTON POLYMERIZATION SUBMICRON FEATURES

by

Ian Seth Ladner

Dissertation

Presented to the Faculty of the Graduate School of

The University of Texas at Austin

in Partial Fulfillment

of the Requirements

for the Degree of

Doctor of Philosophy

The University of Texas at Austin

December 2018

Dedication

I dedicate the work in this thesis to my family. Your continued motivation and support kept me moving forward. You will always be my lifelong inspiration.

Acknowledgements

This document was prepared as an account of work sponsored by an agency of the United States government. Neither the United States government nor Lawrence Livermore National Security, LLC, nor any of their employees makes any warranty, expressed or implied, or assumes any legal liability or responsibility for the accuracy, completeness, or usefulness of any information, apparatus, product, or process disclosed, or represents that its use would not infringe privately owned rights. Reference herein to any specific commercial product, process, or service by trade name, trademark, manufacturer, or otherwise does not necessarily constitute or imply its endorsement, recommendation, or favoring by the United States government or Lawrence Livermore National Security, LLC. The views and opinions of authors expressed herein do not necessarily state or reflect those of the United States government or Lawrence Livermore National Security, LLC, and shall not be used for advertising or product endorsement purposes.

Funding:

This work was performed under the auspices of the U.S. Department of Energy by Lawrence Livermore National Laboratory under Contract DE-AC52-07NA27344 and by the University of Texas at Austin under subcontracts. Funding was available from LLNL's LDRD project 16-ERD-047. Document release # LLNL-TH-761202.

Abstract

Mechanical Characterization of Two-photon Polymerization Submicron Features

Ian Seth Ladner, Ph.D.

The University of Texas at Austin, 2018

Supervisor: Michael A. Cullinan

Two-photon polymerization (TPP) is promising method for additively manufacturing nanoscale structures with complex geometries. For example, TPP has been used to fabricate very high strength-to-weight lattice structures that can be used in a variety of biomedical and aerospace applications. However, one of the major factors limiting TPP as a true manufacturing technique is the uncertainty in how printing parameters affect the mechanical properties of the materials produced at the voxel level. Therefore, the purpose of this thesis is to characterize the scale dependent effects of speed, power, and post curing methods on TPP resists. In order to achieve this purpose, a custom MEMS tensile tester was designed, fabricated, and calibrated for direct integration into the TPP process with resolution and range capable of measuring <200 nm wide voxel lines. Direct integration was accomplished by applying stiction constraints to the suspended elements and fabricating anti-stiction features under the device layer. The load and displacement stages were measured to have a 100 nN and 1.5 nm resolution, respectively, using digital image correlation.

The MEMS tensile tester was used to determine the material properties of TPP voxels written at low and high speeds. High speed voxels were fabricated with line widths varying from 196 nm to 444 nm by increasing the laser power. Both speeds were post processed with three different curing methods. The improvement in elastic modulus from high speed to low speed writing was a determined to be factor of ~2.1. However, it was also found that a UV post cure with radical generators could be used to produce matching material properties between the two writing speeds. That trend is critical for being able to increase the throughput of TPP without scarifying the performance of the fabricated materials. Finally, a strong size effect was found in these TPP materials with a non-linear increase in the elastic modulus (from 3.92 – 6.54 GPa) occurring when the TPP line width was decreased from 444 nm to 196 nm for the UV with radicals post cure condition.

Table of Contents

List of Tables

List of Figures

Chapter 1: Introduction and Background

1.1 INTRODUCTION

As two-photon polymerization (TPP) continues to grow from a research tool to a largescale fabrication method, accurate mechanical characterization of how writing parameters change properties on a material level becomes necessary. Currently, TPP applications in photonics [1], nano/microstructures [2]–[4], and bioengineering [5], [6] that make use of TPP's submicron features could be improved by linking the writing parameters to features size and material properties. Unfortunately, due to difficulties associated with the handling and the scale of TPP structures, most characterization methods used to evaluate TPP resists measure the mechanical large fabricated structures instead of individual voxels. Therefore, traditional material characterization methods for TPP confound the material response of the TPP resists with the structural response of the fabricated structure in ways that make it difficult to extract the mechanical properties of the TPP materials themselves. For example, in compression testing, nanoindenters compress 3D structures which exposes trusses to bending, tension, and compression so a structural model of the truss is needed in order to extract the material properties of the TPP revisits [7]. More uniform loading is produced in bending tests of bulk cantilever [6], [8], but measuring bulk structures cannot account for additional the polymerization that occurs in the structure due to the proximity effects [9].

Microelectromechanical systems (MEMS) tensile testers offer the potential to overcome the limitations of the traditional structural characterization methods by directly measuring the material properties of an individual TPP voxel, or volume pixel. MEMS tensile testers have been demonstrated to work with multiple nanomaterials and can have nanometer displacement resolutions and Nano newton force resolution [6], [10]–[12][13],

which is ideal for mechanical testing of TPP voxels. However, the integration of a MEMS tester into the TPP writing is difficult because the tester must be able to survive being placed into the liquid resin and solvent baths. The purpose of this research is, therefore, to design a MEMS tensile tester for direct integration with the TPP printing process, and to use that tester to conduct parametric studies on the impact of printing parameters on TPP resist properties at the voxel level.

Characterizing the material properties at the voxel scale is critical in determining the tradeoff between write speed, power, and feature size in TPP materials. Current TPP structural trend of aim for the lowest speed and highest power possible to drive up the degree-of-conversion (DC) [14] , which is related to the crosslinking of the polymer, in TPP structures in order to make them stiffer and stronger. However, low speed/high power writes produce larger lines than high speed/low power writes and nanomaterials often show size effects where decreasing feature size improves that material properties of the structures [2], [3], [5], [15]–[17]. There is, therefore, a tradeoff between the write speed/degree-of-conversion and the size effects that must be captured in order to optimize the TPP process. By determining if size effects are present in TPP writing, the writing parameters can be tuned to achieve a specific voxel size and the corresponding mechanical properties (i.e. elastic modulus, yield strength, etc.) however, without capturing this size effect, the current empirical approaches of continually increase writing powers until a specific performance metric is met is the only approach available which leads to sub-optimal build parameters. Therefore, in order to capture the size effect and link writing parameter, size, and material properties to enable deterministic design, it is necessary to conduct parametric studies of writing parameters at the voxel level.

The steps to achieve the material characterization at the voxel level are:

1. To determine a method of integration for writing TPP voxels on the MEMS tensile tester.
2. To design, fabricate, and calibrate the tester to achieve nm and nN level resolution measurements over μm and μN ranges for variations in specimen stiffness.
3. To characterize the effects of writing speed, power, and post curing conditions on the material properties and size effect trends in TPP resists.

A prime example for the impact of this work is the gradient density foams for either hydrodynamic instabilities [18] or isentropic barrier in high energy density physics (HEDP) [19]. Gradient density foams use the beam width and spacing to vary the density of the structure by orders of magnitude as shown in Figure 1.1. However, the finished part tapers with decreasing density as a result of a variation in shrinkage during development. One possible solution would be to increase the elastic modulus to improve stiffness at the same voxel size by adjust speed and power as the density decreases. Additionally, lower densities structures may be achievable with a size effect relationship guiding the selection of writing parameters.

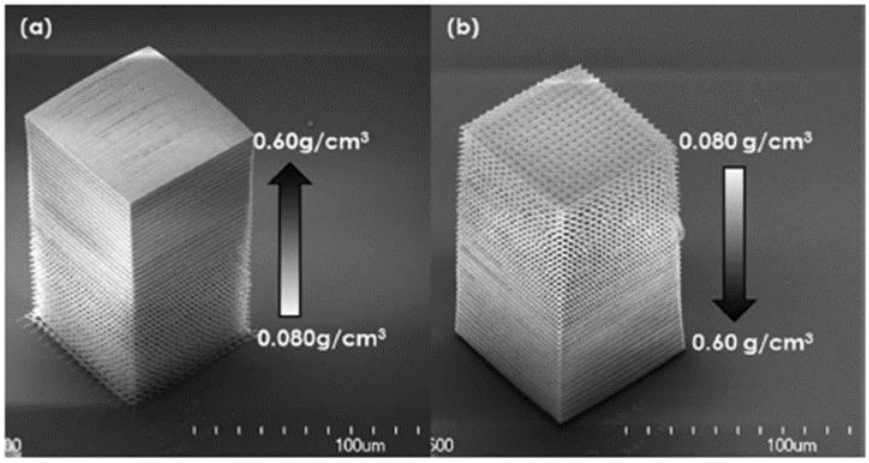

Figure 1.1: TPP gradient density foam for high energy density physics (HEDP) with (b) highlighting failure at the stitch due to residual stress in the part [19].

1.1.1 Outline of Thesis

This thesis focuses on mechanical characterization of TPP structures using a MEMS tensile tester. This chapter introduces this topic, provides background on the mechanisms of TPP, current characterization methods and trends, examines tensile testing methods for nanomaterials with a focus on MEMS tensile testers, and discusses why mechanical characterization of TPP structures was selected for this project. Chapter 2 presents the design of a MEMS tensile tester with nm and nN resolution for direct integration with the TPP process. Chapter 3 presents the microfabrication and custom packaging for the tester. Chapter 4 presents the calibration procedure, experimental setup, and the measured results for the effects of speed, power, post cure, and size on the mechanical properties TPP resists. Finally, the conclusion, improvements, and possible applications of this research are presented in Chapter 5. One application uses results from the degree of conversion/size relationship to improve the elastic modulus and yield strength of a commercially available resist by modifying the resist to produce thinner voxel at higher power.

1.2 TWO-PHOTON POLYMERIZATION BACKGROUND

TPP is a 3D additive manufacturing process which utilizes the nonlinear nature of two-photon absorption (TPA) to print features below the diffraction limit. TPA is the simultaneous absorption of two photons to excite an atom or molecule from a low energy state to an excited energy state. The energy at the excited level is equal to the sum of the two photons as shown in Figure 1.2. This absorption method results in an absorption rate of energy proportional to the square of light intensity, which is pivotal in reaching the sub-diffraction limit feature sizes [20]. TPA was first predicted by Marie Goeppert-Mayer in 1931; however, it was not demonstrated until 1961 after the advent of the laser [21]. This

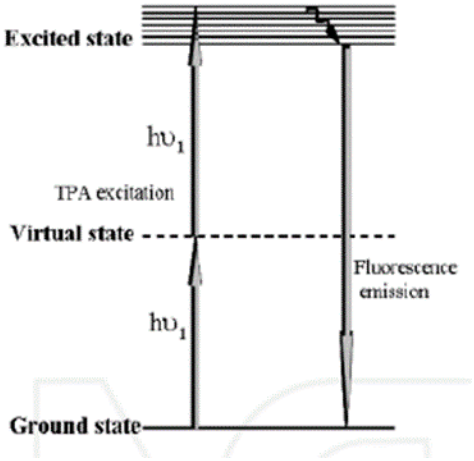

Figure 1.2: Schematic of two-photon absorption [21].

is because ultra-fast lasers were the first instruments to produce the TW level intensities in the time scale required to excite two photons simultaneously [20].

1.2.1 Mechanism of TPP

With the advent of the femto-second laser, the photochemical process in TPP is achieved by tightly focusing the beam with a high numerical aperture (NA) objective into a small volume of photosensitive material. TPA occurs in the small volume when two near-infrared (NIR) photons are absorbed simultaneously by the photoinitiators (PIs) as shown in Equation 1.1-1.3. The absorption energy raises the PIs to an excited state (PI^*) and decomposed to radicals (R), which initiate the reaction. Once generated, radicals combine with the monomers (M) to form monomer radicals (RM) and continue to propagate. When two pairs of monomer radicals combine, the photo-polymerization process is terminated [20], [22].

$$PI \longrightarrow PI^* \rightarrow R\cdot + R\cdot \quad 1.1$$

$$R\cdot + M \rightarrow RM\cdot \rightarrow RMM\cdot \cdots \rightarrow RM_n\cdot \quad 1.2$$

$$RM_n \cdot + RM_m \cdot\!\!\rightarrow RM_{n+m}R \qquad 1.3$$

When the laser is focused into the photosensitive material, the relationship between the power density and the Gaussian light intensity, *I*, is written as

$$-\frac{\partial I(r,z)}{\partial z} = \beta I^2 \qquad 1.5$$

where the density is a function of the *r* (radius from the laser axis) and *z* (length from the focal plane), β the two-photon absorptivity of the material. From this equation, first notice the density has nonlinear dependence on *I* which allows TPP to create focal points smaller than the diffraction limit. This is illustrated in Figure 1.3 where the intensity squared curve decreases the cross-sectional area with large enough intensities. Second, the density is directly related to two-photon absorptivity which is weak process. This requires intensities into the TW/cm^2 range to achieve polymerization threshold [9]. If the threshold increases, the dashed line in Figure 1.3 would move up, further decrease the cross-section, and producing sub-diffraction features size. This relationship enables TPP to write features in the submicron regime where size effects are traditionally encountered.

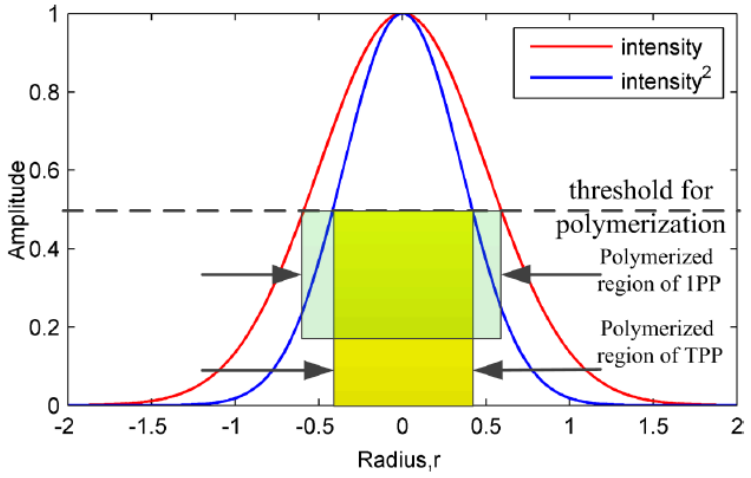

Figure 1.3: Distribution of light intensity for a Gaussian beam with bounding boxes drawn to the intersection with the intensity and squared intensity. The square intensity relationship for TPP shrinks area exposed to a large enough intensity to polymerize [20].

1.2.1 Additive Manufacturing

Additive manufacturing for TPP uses a 780 nm Ti:sapphire laser operating at 80 MHz with pulse lengths of ~100 fs or faster which provides the high intensity source required for TPA [9]. Integrated beam transport optics guide the laser from the source to the high numerical aperture (NA) optic in order to focus it into the photoresist volume. Combining both the fs laser and high NA objects, the intensity reaches polymerization threshold at the focal point where the non-linear intensity results in a voxel below the diffraction limit of the system. Depending on the lens configuration, the objective is brought into contact with either immersion oil or photoresist.

The focal point of the beam is controlled by either scanning the beam in-plane with a galvanometric scanner with a piezo stage for Z motion or by keeping the focal point fixed and moving all three-axes with the piezo stage. An illustration of the 3D path is shown in Figure 1.4. The tradeoff between the two stages is speed versus range. With the galvanometer controlling the beam path, it can achieve speeds above 20 mm/s over a 140 x 140 μm^2 range. Piezo scanning mode slows down to 100 µm/s over 300 x 300 μm^2 range by moving the stage instead of beam. The piezo stage is used in both modes in order to achieve millimeter scale parts by stepping in a direction and overlapping or joining adjacent structures, a process commonly referred to as stitching.

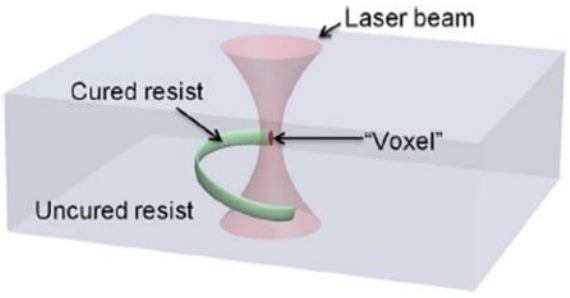

Figure 1.4: Illustration of the laser writing in a continuous 3D path [9].

Microstructures are modeled in either a standard CAD software or custom coding structures in the software packages, such as DeScribe for the Nanoscribe GT laser lithography system. The CAD files are exported as STL files, imported by the systems software package, sliced into layers along the z axis, and printed layer-by-layer. In the custom coding approach, the geometry constructed is not sliced which makes continuous writing in 3D space possible. This is advantageous for structures where the slicing distance may be relatively large compared to the feature size.

After the structures are polymerized, the substrate is placed into the propylene glycol monomethyl ether acetate (PGMEA) developer to remove non-polymerized resist. This step is followed by an isopropyl alcohol (IPA) solvent bath to remove any remaining resist and developer residue from the surface of the substrate and polymerized structure. The fabricated structure is dried either in air or with critical point drying to complete the process.

1.3 CHARACTERIZATION OF TPP STRUCTURES

1.3.1 Introduction

Several methods of characterization and studies of TPP materials are presented in this section. The most common method is for testing TPP materials is compression with a nanoindenter of 3D lattice structures [2], [3], [23], [24]. Other methods include bending with a nanoindenter or AFM [6], [8], a custom push-to-pull printed structure [4], [25], and most recent a MEMS tensile tester [26]. Researchers have used these methods to show elastic modulus and yield stress increasing with increasing power [8], [14], [23] and decreasing write speed [6], [14]. Most of these methods measure structural, not material, behavior of lattices or bulk materials. Kraft *et al.* [4], [25] and White *et al.* [26] present methods that are capable of studying the TPP voxels which fall within the submicron

regime, but they are limited due to structure or range/resolution. Building upon their demonstrations, a new material characterization method with improved range and resolution is presented in this thesis.

1.3.2 Need for A Submicron Characterization Method

Submicron characterization methods enable research into the effects of printing parameters and resist chemistry on the material properties of TPP resists. With this method, material properties can be isolated from structural properties. Parametric studies can be conducted with writing speed and power and compared to the structural tests to determine if the trends agree/disagree and how much of the trend is a function of material size. Researchers can correlate material properties to printing parameters to deterministically design structures instead of taking an iterative approach.

Parametric studies of post processing conditions, such as thermal cure by Kraft *et al.* [25] and UV cure with radicals by Oakdale *et al.* [23], have shown improvements in yield strength and elastic modulus which are attributed an increase in degree of conversion (DC). DC is related to the crosslinking of the polymer and traditionally measured by Raman spectroscopy to detect the consumed carbon by measuring the intensity of the C=C bond [14], [23]. By comparing bulk trends to size effect trends, researchers may gain an understanding into the cross-linking of single voxels and the sensitivity of the material properties to resist chemistry. This could result in improved material properties and smaller feature sizes which would be applicable for high density forms [18], [19] and photonic crystals [1] where resolution is limited by the structure's rigidity during the drying process.

One of the dominant challenges for a submicron scale testing method is sample handling. Testing methods have been designed to completely remove sample handling from the equation with compression testing or printing the testing structures. This thesis

will further examine TPP characterization methods and explore nanomaterial characterization techniques to determine a possible solution capable of testing submicron features without sample handling.

1.3.3 Current TPP Characterization Methods

1.3.3.1 Compression

The first and most common characterization method is compression test via nanoindentation [2], [3], [14], [23]. In these studies, different versions of nanoindenters are used to compress lattice structures of different materials with load resolution into the nanonewton range. Load and displacement data from the nanoindenter is used to calculate hardness and reduced elastic's modulus, E_r. Elastic modulus, E, can be calculated from E_r with Equation 1.6

$$\frac{1}{E_r} = \frac{(1-\nu)}{E} + \frac{(1-\nu_i^2)}{E_i} \tag{1.6}$$

where ν is the Poisson ratio of the TPP polymer, ν_i is the Poisson ratio of the indenter, and E_i is the indenter Young's modulus.

Jiang *et al.* [14] compressed solid cubes and collected Raman data to capture an increase in E and hardness with an increase in DC and showed a higher sensitivity to increasing power than decreasing speed. This trend is expected with DC being related to the cross-linking of the polymer. Oakdale *et al.* [23] expanded the scope to include a post UV-curing process. In his study, E and σ_c (compressive yield stress) improve linearly with structure density and UV-curing increases performance in both categories.

When calculating E in Equation 1.6, ν is assumed constant for all printing parameters, which may limit the accuracy when going from feature widths in the 100 nm range at writing threshold to the +500 nm range at maximum power. Additionally, the

lattice structures will produce bending and stretching loads on different struts making material characterization even harder to differentiate from the structural properties of the written systems.

1.3.3.2 Bending

In order to remove Poisson ratio and conduct single variable testing, Cicha *et al.* [8] and Zhang *et al.* [6] used the nanoindenters to bend cantilever structures, as shown in Figure 1.5.a, to measure the Elastic modulus directly. By solving a tradition fixed-free beam equation, the *E* is

$$E = \frac{FL^3}{3Iy} \tag{1.7}$$

where *F* is the load, *L* the beam length, *I* the moment of inertia, and *y* the displacement. In this case, the load and displacement data are used to calculate the bending stiffness of the cantilever beam at different powers by Cicha *et al.* and speeds by Zhang *et al*.

In Cicha *et al.*, cantilever beams were printed with constant writing speed of 650 μm/s and geometry while the print power was increased from 9 – 25 mW. An image of the cantilevers is in Figure 1.5.a. The results from the experiment showed a positive relationship between *E* and power, similar to the compression studies [8]. Zhang *et al.* printed cantilever beams with constant power of 15 mW and speed ranging from 200 – 600 μm/s at 100 μm/s steps [6]. Speed shows a negative relationship which follows the DC trend from Jiang *et al.* [14].

Just like the compression tests, this method is limited to larger parts. Additionally, the solid structures may be damage by writing conditions due to the proximity effect [9]. However, the parts are small enough to be sensitive to other printing parameters, such as writing direction, hatch and layer spacing, and hatch angle which makes separating the material properties from the print structure properties difficult [24].

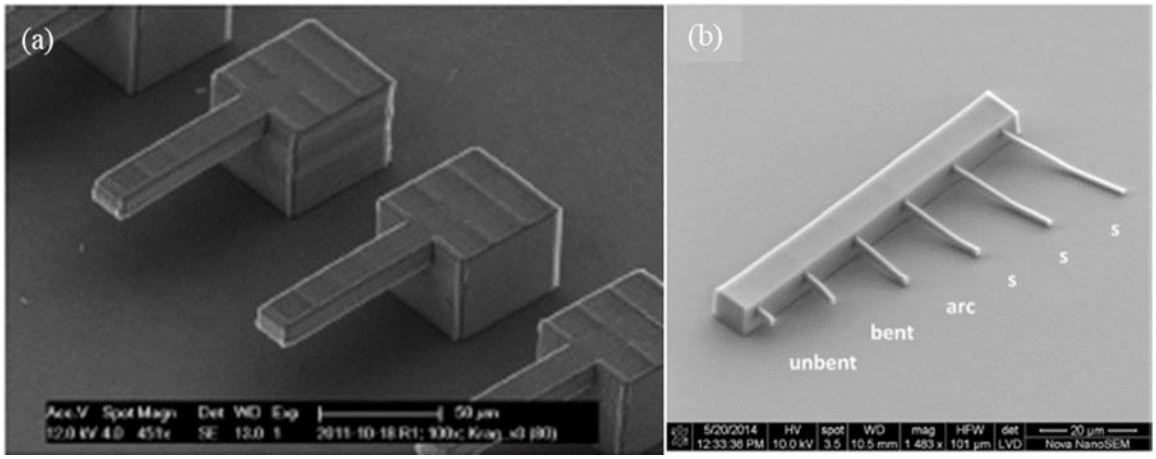

Figure 1.5: (a) Solid cantilever beams for bending tests [8] and (b) single voxel beams for stiction study [6].

Zhang *et al.* also used capillary forces to bend single voxel cantilever beams. Capillary forces result from the drying of a liquid, and the elastic modulus can be calculated by comparing the elastic strain energy in the beam and the adhesive surface energy bend beams. Two bending conditions are used to calculate the modulus based upon an 'arc' shaped bend with just the tip of the beam pinned and an 's' shape bend with a flat portion after the pin, see Figure 1.5.b. The Elastic modulus for each case, E_{arc} and E_s, is

$$E_{arc} = \frac{16\gamma \cos\theta_c \, s_{arc}^4}{3t^3h^2} \tag{1.8}$$

$$E_s = \frac{4\gamma \cos\theta_c \, s_s^4}{3t^3h^2} \tag{1.9}$$

where γ is the liquid surface energy, θ_c is the liquid contact angle, s_{arc} is the length of the beam to the arc contact point or s_s the length of the beam to the 's' contact point, t is the beam thickness, and h is the vertical gap between the beam and the substrate [6].

While simple, this method requires a proper characterization of θ_c for each TPP resist tested. An SEM will be needed for defining the arc condition and measuring the length to contact point but this is difficult because electron irradiation can damage the samples and impact the accuracy of the measurement.

1.3.3.3 Tension

Two groups have demonstrated tensile measurement on TPP structures. Bauer and Kraft *et al.* [4], [25] designed a push-to-pull tensile tester with a hexagon frame and a single voxel written as a dog bone across the middle, shown in Figure 1.6.a. A nanoindenter is used to apply a compressive force to the top surface while the corners of the hexagon act as pin joints and bend outward to generate a tensile load at center of the hexagon. The tensile force, F_t, is applied to the single voxel printed between pins. Assuming an ideal pin joint, the force is

$$F_t = \frac{\Delta F}{\tan \phi(y)} \tag{1.10}$$

φ is the angle between the test bar and the frame which is a function of the displacement, y. Stress – displacement data is generated from ΔF_T and change in full dog bone length. The total dog bone length and flexure in the frame result in large uncertainties in this measurement.

This method was used to determine the effects on varying the time and temperature of post print thermal curing [25]. Thermal cures at 200°C performed better than 250°C, but there is no clear trend for time. The test does show an improvement of 2.5 times for elastic modulus, a factor of 10 increase in failure strength, and a factor of 5.6 in hardness.

Jayne *et al*. demonstrated direct integration between MEMS and TPP to study the stiffness for different writing speeds and resists [26]. A folded spring structure was printed between a fixed pad and a MEMS on-chip actuator, as shown in Figure 1.6.b. In this arrangement, the spring constant for four different parameters were calculated by measuring the displacement of the capacitor driven stage. The displacement resolution was 300 nm.

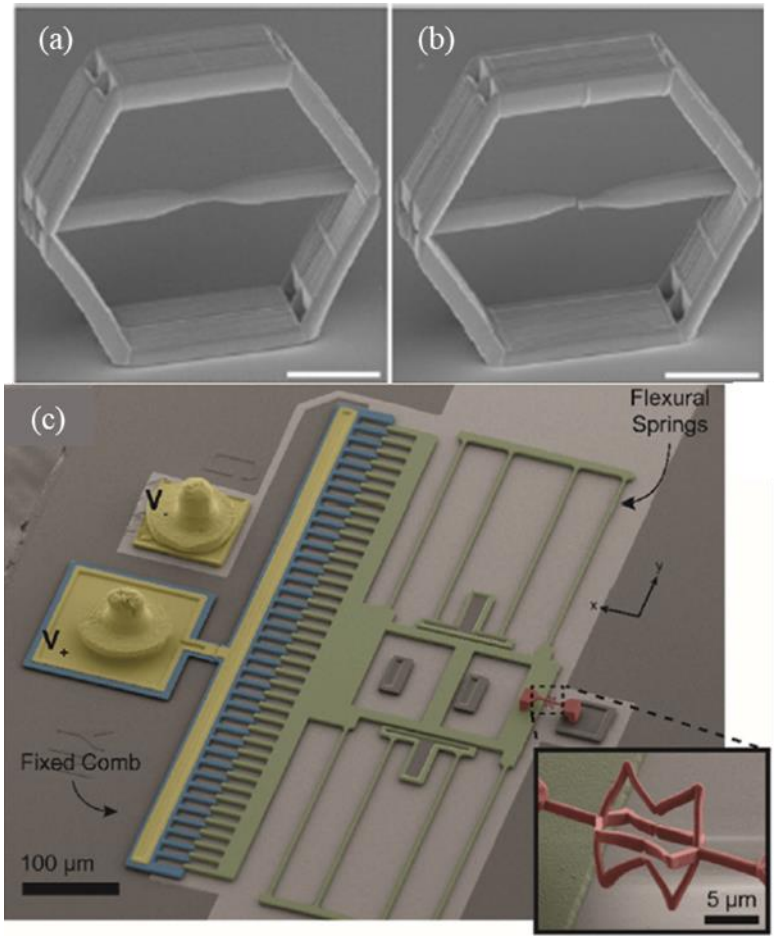

Figure 1.6: The Push-to-pull TPP tensile tester with a (a) solid and (b) fractured voxel [4] and (c) the MEMS based tensile tester [26].

Both of these methods are able to characterize material properties by measuring single voxel features. However, the push-to-pull sensor is limited by the ideal pin joint condition, angle measurement, alignment of the nanoindenter, and the potential for hysteresis in the hexagon structure after large strains. The style of MEMS tensile tester selected requires an actuator stiffness close to the part stiffness which limits the maximum load and stain and requires feedback control scheme to maintain a constant strain rate. Therefore, neither of these methods is ideal for measuring the material properties of TPP voxels.

1.3.3.4 Comparison

A summary of the current characterization methods is presented in Table 1. The table compares the required part size, measurable material properties, and limitation. Compression testing offers high resolution with commercial nanoindenters and AFM as the loading mechanism; however, they are all limited to measuring 3D structures and the reduce modulus which assumes the Poisson's ratio is constant. Bending utilizes the same high resolution nanoindenters and AFM, and it is capable of measuring structures down into the 5 μm x 1 μm cross-sectional area. Elastic modulus is calculated directly from the bending equation, but it is still measuring structural properties. The capillary force approach to bending allows for measurements of single voxel parts, but it is limited by the measurement method of the beam length and user defined arc condition. The push-to-pull tensile tester has a high resolution actuation method with the nanoindenters and measures elastic modulus of the material by uniaxial tensile loading of a single voxel but it is hampered by the ideal behavior of the pin joint assumption and angle measurements at high strains. The MEMS tensile tester also conducts a tensile test on a voxel structure with a displacement resolution of 300 nm. However, this tester design is limited by the measurement method to low stiffness springs or structures.

Method	Specimen Size	E calculation	Limitation
Compression [ref – Oakdale, L Zhang]	100 x 100 μm^2	$\frac{1}{E_r} = \frac{(1-\nu)}{E} + \frac{(1-\nu_i^2)}{E_i}$	Specimen size Assume constant ν
Bending [ref – cicha, S Zhang]	μm^3 solid beam	$E = \frac{FL^3}{3Iy}$	Specimen size
Stiction [ref – S Zhang]	Single voxel	$E_{arc} = \frac{16\gamma \cos\theta_c \, s_{arc}^4}{3t^3h^2}$ $E_s = \frac{4\gamma \cos\theta_c \, s_s^4}{3t^3h^2}$	Measurement accuracy
Push-to-pull [ref – bauer, schroer]	Voxel dog bone	$E \approx \frac{\Delta F_t}{\Delta L}\left(\frac{l_i}{A_i}\right)$ $F_t = \frac{\Delta F}{\tan\phi(y)}$	Ideal pin connection Uncertainty in ΔL
MEMS tensile tester [ref – Jayne]	Voxel spring	$E = \frac{k\Delta x}{A_c \Delta L}$	Load cell stiffness Measurement resolution

Table 1.1: Summary of specimen size, elastic modulus calculation, and limitations for the current characterization methods.

The main takeaway from the comparison is tensile testing offers the best accuracy for material characterization of a single voxel but that the two methods currently used, push-to-pull and MEMS tensile tester, have limitations from the behavior of deforming joints to the low stiffness requirements for the tensile tester. This means there is still a need for a high resolution, tensile characterization method independent of structures and with a large range. One possible resource is to investigate characterization of other nanoscale materials, such as thin metal films, nanowires, and electrospun polyacrylonitrile (PAN) nanofibers.

1.3.4 Nanoscale Tensile Testing Methods

Material characterization methods for micro- and nanoscale materials have been in development since the 1950s when S. S. Brenner conducted tensile tests on micron scale metal whiskers [15]. The methods vary based upon actuation, measurement methods, and desired resolution, but tend to fall into two categories: AFM tip-based and MEMS based.

1.3.4.1 AFM Tip-based

One of the key challenges to tensile testing at the nanoscale is sample handling and manipulation, which is traditionally done with an AFM or nanomanipulator. To reduce the processing steps and take advantage of the commercially available AFM cantilevers, researcher developed methods to use the AFM as an actuator and/or a load cell. The approach is to attach a low stiffness AFM cantilever to a piezoelectric actuator, which offer both nm resolution and μm range. The AFM is guided to the sample where focused ion beam (FIB) deposition bonds the sample to the tip. At this point, the AFM can act as the actuator and the specimen's stiffness can be determined by measuring the displacement of the AFM tips.

To utilize the AFM cantilever as a load cell, an additional form of actuation is required. Yu *et al.* [27] conducted the first *in-situ* SEM tensile test of a multiwalled carbon nanotube with a pair of AFM cantilevers. The load cell had a very low stiffness, < 0.1 N/m. The actuator AFM was very rigid. During loading, the SEM was used to capture images, such as the one in Figure 1.7, to measure the displacement of the specimen and load cell AFM.

A second approach taken by Hoffmann *et al.* [28] was to actuate the specimen's substrate. This case took advantage of vertically grown ZnO nanowires, which do not require sample manipulation if isolated on the substrate. The AFM cantilever was

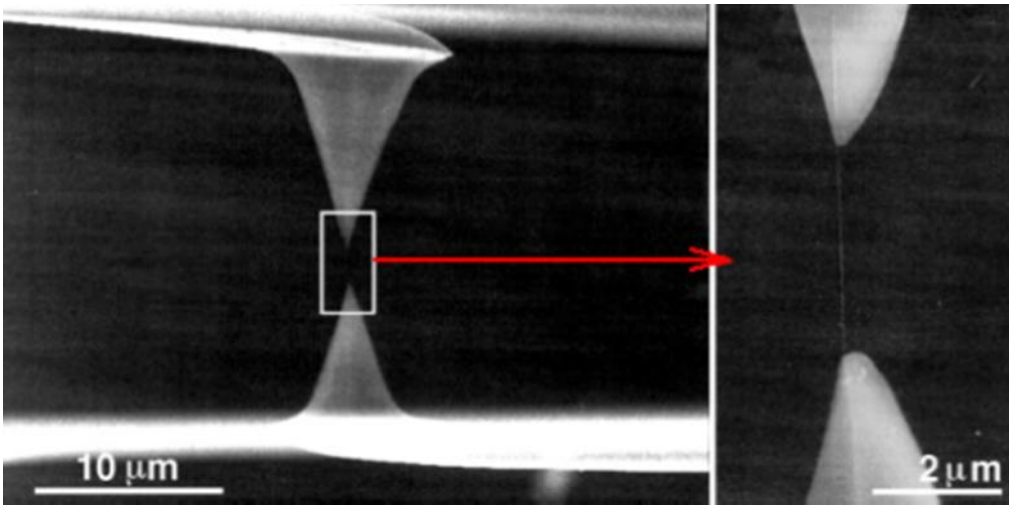

Figure 1.7: AFM tensile test with a multi-wall CNT between two AFM tips [27].

mounted onto a piezoelectric actuator for positioning only. Once the nanowire was bonded onto the tip, the sub-nanometer resolution actuator moved the substrate away from the AFM tip. SEM images were captured to measure the deflection of the AFM tip.

The challenge with using AFM tips for tensile tests is the induced bending moment by misalignment or large deformations in the AFM beams. Misalignment of the AFM is function of sample preparation and operator precision, which can be limited in the case of vertically aligned samples. However, even with a perfect alignment, large deflections of the AFM cantilever will introduce bending at the bond point of the specimen due to a rotation at the tip. This can be limited by increasing the stiffness of the cantilever, but this will lead to a tradeoff condition between bending and resolution.

1.3.4.2 MEMS Tensile Tester

Much like AFM cantilevers, microfabricated devices can achieve very high resolutions by tuning the flexure size and design for the load cell. Additionally, a microelectromechanical system (MEMS) based tester can offer on-chip techniques to

decrease mis-alignment errors for external loading, offer on-chip actuation methods with thermal and electrostatic, and on-chip sensing to replicate a macro-scale tester [13], [15]. Several designs will be presented in the Section 1.4.3.

1.3.4.3 Sample Handling/Manipulation

The main challenge for both methods is the sample handling and manipulation. With the emergence of the AFM and nanomanipulators/nanoindenters, specimens could be grown on one substrate and gently harvested and moved to the testing apparatus. Additionally, methods were developed with the manipulators as the loading mechanism which did not require handling the sample. The advantage of moving to a separate testing apparatus is the freedom for researchers to modify the actuation and measurement methods based upon the material and desired testing environment.

In addition to manipulation, some researchers have demonstrated co-fabrication of the specimen with the testing apparatus. This has been demonstrated with thin films [29], [30] and with TPP [4], [25], [26]. Jayne *et al.* [26] printed the TPP specimen directly onto the MEMS tensile tester, which completely removes sample handling from the process. However, it exposes the suspended features to stiction failure methods. In this thesis, the impacts of stiction are tensile tester design are presented.

1.4 PRIOR ART

1.4.1 Structural Trends in TPP

The structural studies presented in Section 1.3 show early results in key trends for the writing speed, power, and post cure effects on material properties and degree of conversion, DC. DC is a measure of the number of carbon-carbon double bonds (C=C) consumed during polymerization to form carbon-carbon single bonds (C–C) which is

related to the cross-linking of the polymer. Jiang *et al.* used Raman microspectroscopy to show that DC increases with decreasing speed and increasing power, as shown in Figure 1.8.a. This is attributed to the laser absorption having a squared power relationship and a the dose being reciprocal to writing speed [14]. Compression testing showed increasing modulus and hardness for increasing DC, Figure 1.8.b. The power trend has also been captured with [8], [31] and speed by [6], [26].

Oakdale *et al.* [23] also used compression testing, but on octet lattice structures at a high writing speed of 10 mm/s. In order to produce structural stable parts, Oakdale added a UV flood exposure in an IPA solution with photoinitiators as a post-fabrication curing process. The UV exposure excited the photoinitiator to generate radicals via single photon absorption, and the DC increased by 40 – 60% after just 10 minutes. The increase in DC led to a greater than 50% increase for both elastic modulus and yield strength of the structure.

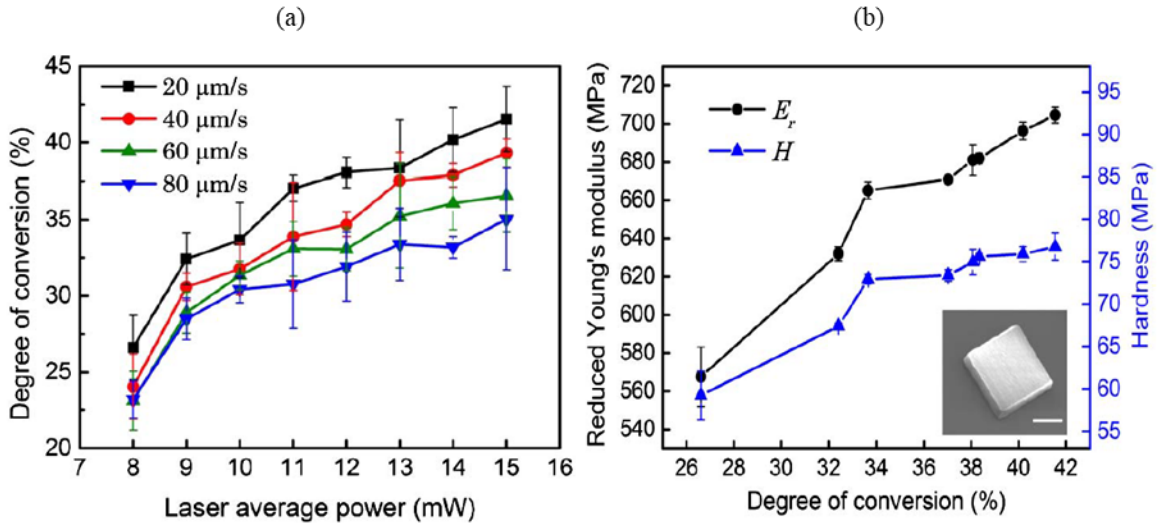

Figure 1.8: (a) Degree of conversion versus writing power for low speed writing and (b) modulus and hardness versus DC [14].

These three trends will be explored at the material level in this thesis. However, DC was not be captured in this work due to the voxel width, but it will be requested in Section 5.3. Additionally, a UV only post cure will be added to determine the impact of the radical generators.

1.4.2 Size Effects in Nanomaterials

The size effect in a material is a length scale effect where materials properties, such as strength, increase with decreasing size due to external and internal length scale effects. External length scale effects are related to the specimen size and internal length scale effects are related to the length scales of the microstructures [17], [32], [33]. For external length scales, macroscale specimens are orders of magnitude greater than the respective microstructure; however, for thin films, nanotubes, or TPP structures, the smallest feature size is potentially the same order of magnitude as the microstructure. In this region, the feature sizes are approaching the intrinsic lengths directly tied to mechanical properties, such as elastic modulus and failure due to the presence of a crack shown in Figure 1.9. Additionally, for 1D materials the surface-to-volume ratio increases with decreasing size raising the sensitivity to surface.

The internal length scale effects capture the micro- or nanostructures interaction with dislocations. For crystalline materials, the relationship for strength is represented by the Hall-Petch relationship where yield strength increases with decreasing grain size of the material. Additionally, as the grain size, and specimen size, decrease the size and probably of defects and dislocations are reduced. However, once the grain size passes 100 nm the rate of change decreases until around 10 nm where the yield strength starts to decline. This inverse Hall-Petch effect has been verified experimentally and with molecular based

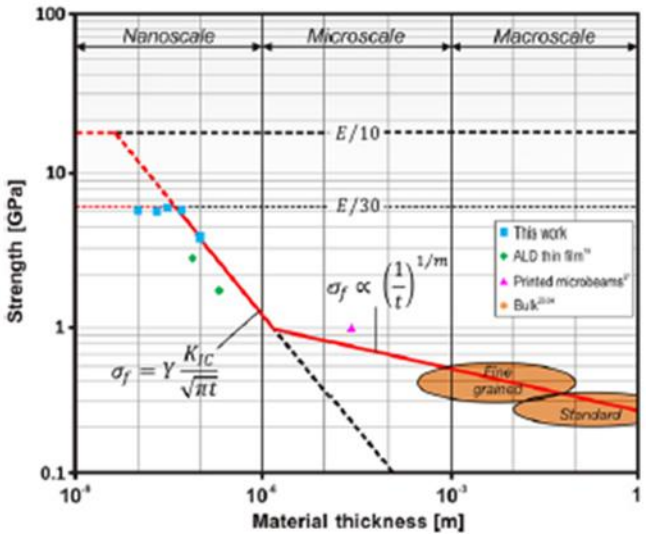

Figure 1.9: Strength versus material thickness for alumina. As the feature size approaches the critical crack length, the rate of increase for the strength increases [4].

simulations, but the underlying mechanism is still under defined. The small size of the grain leads to a decrease in ductility and modulus [17].

When considering TPP, the external scale effects are easy to determine with the voxel widths ranging from 100 – 500 nm. The internal effects are related to the degree of conversion, and contribute to highly cross-linked polymers behaving like crystalline materials. Additionally, due to the cross-sectional area, writing path, and potential polymer length, the directionality of the polymer chains should also be considered [25]. These scaling effects make it likely that size effects are present in TPP structures.

1.4.3 MEMS Tensile Testers

1.4.3.1 MEMS Tensile Tester Types

In the field of MEMS tensile testers, there are three general design types: 1) on-chip actuation with external load and elongation measurement, 2) external actuation with

on-chip load measurement, and 3) both on-chip load actuation and measurement which are illustrated in Figure 1.10 [13]. Type 1 has the advantage of a truly fixed point on the chip to clamp the specimen and simple design, however the lack of real-time load measurements and required continuous calibration of the actuator pose major drawbacks. Type 2 integrates an on-chip load measurement making real-time measurements possible, but the major advantage is that these devices can be integrated with commercially available actuators. This remove any complexity from MEMS actuator design and calibration. However, the assembly of the external actuator is tedious and prone to misalignment errors in- and out-of-plane [34].

Type 3 is modeled after the traditional macroscale tensile tester with a load cell and actuator on opposite ends of mounting clamps for true *in situ* measurements. The challenge presented with this approach is the significantly increased design, fabrication, and calibration complexity. In addition, devices which use deposited polysilicon for structural layers may have residual stresses deposition that can cause out-of-plane bowing or varying heights along the central shuttle and between the two clamp tips, skewing results [10]. However, since its first demonstration by [35], the type 3 tensile-tester-on-a-chip has been a more common design scheme with varying actuation methods, sensing resolutions of <30 nN [10], [12], [36] and <1 nm [35], [37], [38], and fabrication methods.

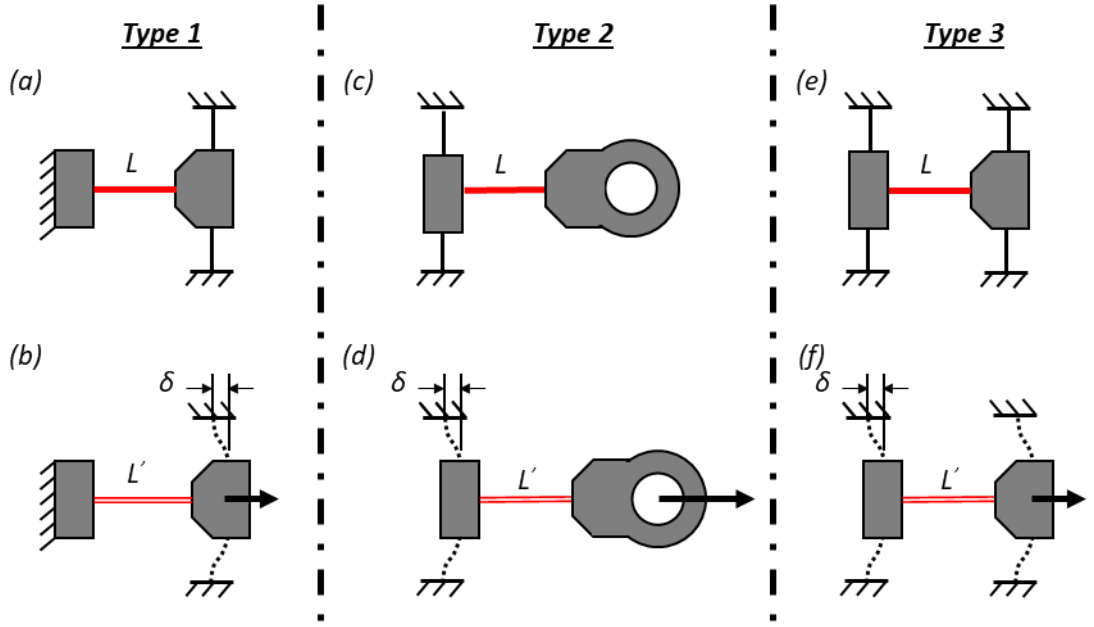

Figure 1.10: Diagrams of the three tensile tester types. Type 1 uses an on-chip actuator in (a) and (b). Type 2 measures the load on-chip from an external actuator in (c) and (d). Type 3 measures and generates the load on-chip in (e) and (f).

1.4.3.2 External Actuators

External actuators are traditionally piezoelectric actuators attached to AFM beams or a nanomanipulator which either hooks into a hole in the device layer or is glued into position. This actuation takes advantage of commercially available piezoelectric actuators with resolution in the nN range. While the piezoelectrical actuator provides the displacement, the load and displacement are measured with features on the chip. Naraghi *et al* [12] used this approach to test electrospun polyacrylonitrile (PAN) nanofibers. A displacement resolution of 50 nm was achieved by capturing regions on the load cell, the displacement cell where the actuator is connected, and a fixed point on the device in a single image. The challenge with this approach is misalignment errors when connecting the actuator.

Haque and other researchers [39] addressed this challenge by adding ‘U’ shaped flexure between the structure of the device and the actuator mounting pad. The flexures between the device and the actuator pad deform whenever the actuator is misaligned. Fixed-guided flexures on the device restrict the out-of-plane motion from impacting the direction of the load on the specimen. Further improvements were made by disconnecting the displacement shuttle to decrease the bending load on the shuttle. These devices, shown in Figure 1.11, were used to measure nanoscale thin films inside an SEM and TEM.

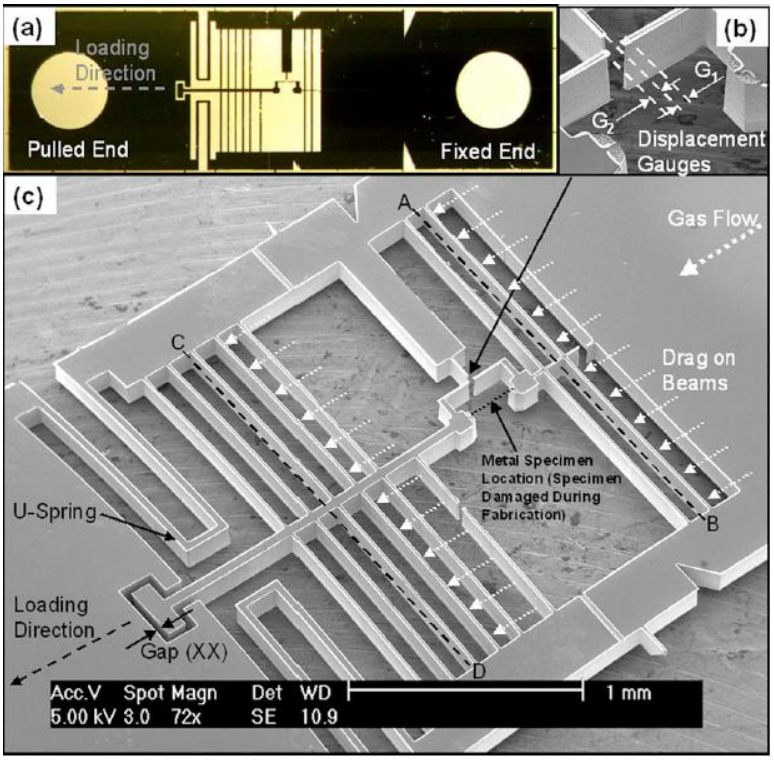

Figure 1.11: Externally actuated MEMS tensile tester with ‘U’ springs and disconnect between actuator connection and displacement stage [39].

1.4.3.3 On-chip Actuators

On-chip actuation is traditionally accomplished with either comb drive or thermal actuators, as shown in Figure 1.12. Comb drive actuators are driven by electrostatic force created between parallel plates under a bias. This actuation method produces force control actuation with large displacements (> 10 μm) and limited force (typically hundreds of micronewtons). Kiuchi *et al.* [40] used comb drives with between 1000 to 5000 capacitive fingers to study carbon nanowires. This work presented both co-fabrication and the use of displacement amplification with a gain of 100 times. In the seminal work for on-chip sensing, Zhu and Espinosa [41] developed both a force control tester with capacitor and a displacement control with a thermal actuator. The capacitor actuators have been used to study several thin films and carbon nanomaterials [13].

Thermal actuators are traditionally used in cases where high force or displacement control is required. When an electrical bias is supplied to the inclined beams, the current is converted into heat through Joule heating. As the beams increase in temperature, volumetric expansion generates the displacement control actuation with limited range (less

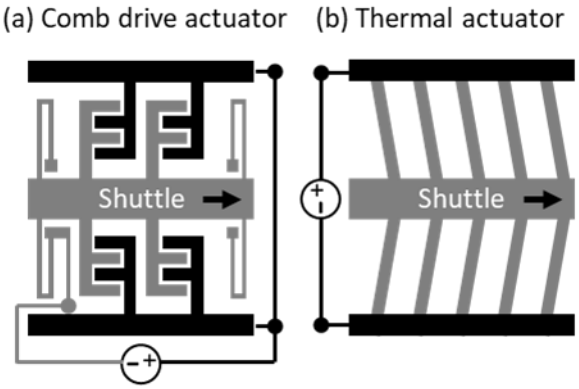

Figure 1.12: Schematics of (a) Comb drive actuator where the black fixed fingers pull the grey shuttle and (b) thermal actuator where thermal expansion of the grey beams push the shuttle.

than 10 μm) but large maximum forces (up to tens of millinewtons), due to the stiffness of actuator. This actuation method has been used by several groups to demonstrate variations in fabrication methods from Poly-MUMPs with Espinosa *et al.* [10], [42] to SOI-MUMPs with Cheng *et al.* [43]. Pierron *et al.* [38] used the displacement control attribute of the thermal actuator for fatigue testing of Au ultrathin films.

Since TPP structures have shown viscoelastic behavior [44], thermal actuation is chosen for this tensile tester for its ability to be displacement controlled and produce a constant strain rate with loading range into the tens of millinewtons. This will limit the maximum strain in the test, but the length of the voxel can be reduced to increase the strain if desired.

1.4.3.4 External Load/Displacement Measurements

External methods for measuring load and displacement are as simple as tracking the position of the load cell and displacement tip from one image to the next through a process called digital image correlation (DIC). Methods exist to manually track the position by counting pixels, but the work is tedious and limited by the operator. By applying DIC algorithms, the measurement accuracy from image to image can be sub-pixel. This method has been widely used within the tensile test community with optical systems and SEM/TEM. Naraghi *et al* [12] used a focused ion beam (FIB) to mill random patterns onto the load, displacement, and chip regions to improve the resolution compared to the smooth surface of the fabricated device. The limitation of DIC is the field of view (FOV) must include elements from the load cell, displacement shuttle, and a fixed region.

Saif *et al.* [39] added reference features within a small FOV next to improve the systems resolution, shown in the top left corner of Figure 1.11. Similar design schemes have been demonstrated by D Zhang *et al.* [11]. By reducing the size of the shuttle and

positioning the support of the flexure near the tip, this method of sensing can be applied to most designs. For this design, it is put in place to increase the resolution during the calibration phase.

1.4.3.5 On-chip Sensing Methods

On-chip sensors are traditionally piezoresistive beams or variations of capacitive sensing. Piezoresistive beams utilize the piezoresistive effect in silicon or polysilicon to convert mechanical strain into a change in electrical signal. As the beams deform, the relative change in electrical resistance varies with respect to relative change in strain, and the ratio is determined by the material's gauge factor [45]. Previous designs have demonstrated the feasibility of piezoresistive sensing with Z-shaped thermal actuator beams [46]. Tradeoffs in piezoresistive sensing are noise levels and temperature sensitivity in the output electrical signal and the fixed value of the gauge factor which limits the resolution of the sensor.

Capacitive sensing, on the other hand, is traditionally insensitive to temperature and can reduce electrical noise through plate arrangement [13]. For a basic MEMS capacitive sensing, one plate of the capacitor is fixed while the second moves with the shuttle increasing or decreasing the gap between the two plates, or fingers. Figure 1.13 illustrates the multiple variations that have been reported in MEMS tensile testers, parallel plate [37], tri-plate [11], and full differential [10]. The basic configuration is shown in Figure 1.13.a where the total capacitance is sum of the capacitance on both sides for the fixed fingers. The tri-plate differential capacitor, Figure 1.13.b, shifted the second set of parallel capacitors to produce an easily manufactured differential capacitor, increasing the gain, range, and reducing the parasitic capacitance. To further increase the resolution of the sensor, a differential measurement can be made with each set of capacitors shown in Figure

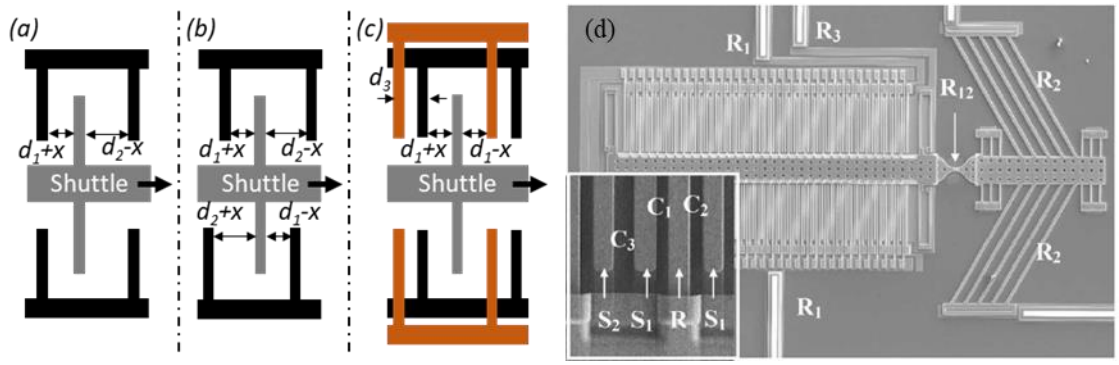

Figure 1.13: Schematics of (a) tradition capacitive sensor, (b) tri-plate for differential across the shuttle, and (c) full differential on each side of the shuttle. (d) Espinosa *et al* [10] tensile tester with full differential sensors.

1.13.c, which adds the fixed capacitance across d_3 to the measurement. An example of Espinosa *et al* thermal actuator and differential sensor is shown in Figure 1.13.d.

1.5 SCOPE

1.5.1 Technical Approach

In order conduct size dependent material testing on TPP resist, an instrument or characterization method must be developed that tackles the handling challenge of submicron, polymer features and has the range and resolution to measure specimens with a range of material properties. As discussed in the background section, the current characterization methods have determined the effect of printing parameters on structural properties, but studying the materials properties at the submicron minimum features size have been limited. The purpose of this thesis is to characterize the effects of printing parameters and size on TPP material properties.

In order to study submicron features, the MEMS tensile tester has been designed and fabricated to be directly integrated with a TPP AM process. As seen in Figure 1.14, the device is composed of a thermal actuator and two differential capacitor sensors with extended tips for printing the structure. Once packaged, a drop of the TPP photoresist is placed onto the MEMS tester and loaded into the TPP instrument. A microscope objective is raised into contact with the droplet. The femtosecond laser scans to print the structure between the suspended tips. A series of solvent baths remove the unpolymerized resist and residue from the tester. Once dry, structure is loaded with uniaxial tension while displacement and load data are captured.

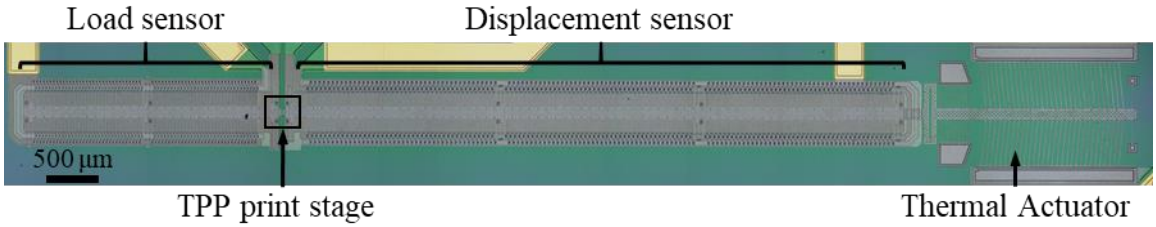

Figure 1.14: Custom MEMS tensile tester for direct integration with TPP.

1.5.2 Material Testing: Writing Parameters and Size Effects

The material tests in this thesis are designed to capture the effect of writing speed, writing power, post cure method, and size effect on the material properties of a commercially available TPP resist, ID-Dip. The first test is conducted at low-speed (100 µm/s) and high-speed (10 mm/s) with a line width of 377 nm to capture the change material properties when increasing throughput. The line width is maintained by increasing the write power with the write speed. Additionally, the low- and high-speed parts are studied with three post cure conditions, no cure or Green, UV cure only, and UV with radical generators, to determine the effect of additional photocuring after writing.

In the second set of experiments, speed is held constant at 10 mm/s while power is varied to change the voxel widths from 150 – 425 nm. Five different line widths are tested with no cure, or green, and UV with radicals. The addition of post cure conditions improves the ability of the study to capture both size and power effects. In the green case, variations in performance can be attributed to a change in cross section or a change in degree-of-conversion due to changes in power. For the UV cure with radical generators, the additional DC from post curing can also be studied with respect to size and initial DC by comparing the trends captured in the green condition.

An additional experiment is run to compare the impact of post cure conditions and elasticity. With the potential for non-linear elastic and viscoelastic behavior in polymer materials, the traditional linear regime of a tensile tester will not be enough to determine the elastic limit. An additional tensile test is used to load and unload the same part with continuously increasing maximum displacement. The elastic limit can be determined by measuring when a plastic shift in the load cycle occurs.

Chapter 2: MEMS Tensile Tester

2.1 Introduction

Uniaxial tensile testing of individual voxels is required to characterize the process parameters and size dependent of mechanical behavior for TPP resists. Most techniques employ compression testing of 3D structures to avoid handling the sub-micron features. In this chapter, the design, fabrication, and calibration of a MEMS tensile tester capable of direct integration with two-photon lithography is presented.

The focus of the design is on a displacement-controlled MEMS tensile tester with integrated load cells and displacement sensors compatible with the repeated submerging in photoresist/solvents and drying required for TPL. This is important for the development of new photoresists because it allows researchers to study the effects of writing conditions such as speed and power and processing conditions such as post curing on the mechanical properties of the photoresist at the voxel scale. Currently, those parametric studies are conducted with the compression and bending of 3D structures [2], [6]–[8], [14], [23] due to the handling challenge at print scales of hundreds of microns. However, these types of tests study structural properties and a material characterization method is required in order to guide custom resist development. The development of the MEMS tensile tester presented in this chapter will enable researchers to characterize the mechanical properties of TPL resists by testing individual voxels and determine chemistry formations to tune material properties. The design presented in this chapter build upon the tensile tester prior art presented in Section 1.4.3.

2.2 Need and Description

The MEMS tensile tester presented in this chapter is designed to measure the load and elongation of submicron wide voxels with nm and nN resolution by directly integrating

the tester with the TPL process. Sensing methods are implemented on both sides of the voxel specimen to capture the displacement with sub-nanometer to nanometer resolution. The two-sensor approach improves the accuracy of the strain measurement. Additionally, a displacement control actuator provides strain-rate independent loads into the hundreds of μN to study the plastic behavior of voxels with a range of stiffnesses.

In direct fabrication of voxels on the tensile tester, shown in Figure 2.1, a droplet of photoresist is placed onto the tester and it is loaded into a Nanoscribe GT laser system. The dip-in lithography (DIL) mode raises a microscope objective into the resist droplet and a femtosecond laser writes the tensile specimen across the contact pads of the tensile tester. Solvent baths are used to remove the unexposed photoresist and residue before drying in air. The tensile tester is designed to prevent failure due to surface adhesion and capillary forces generated during the printing process.

With this approach, TPL structures, whether single voxel lines or complex 3D structures, can be printed directly onto the tensile tester. Once the structure is printed and the excess material is cleaned away, the tensile tester can apply uniaxial loading at a defined strain rate or frequency to measure the mechanical properties of the resist such as elastic modulus, yield stress, and ultimate tensile strength. Studies can then be conducted to determine the impact of writing conditions and chemistry on the resist's material properties

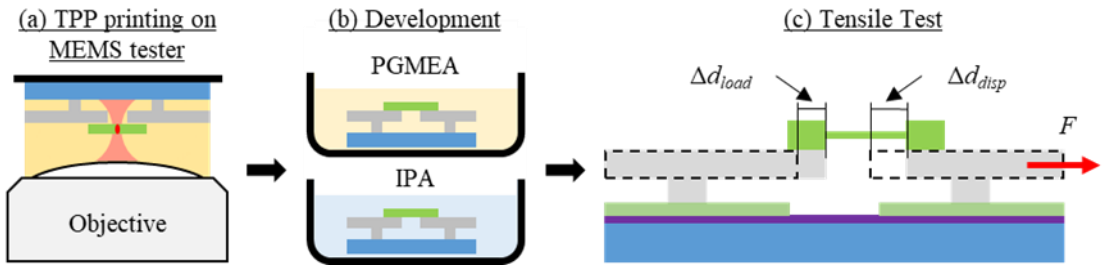

Figure 2.1: Schematic of the process integration of a MEMS tensile tester with TPL [47].

while quantify the scale dependent trends. Overall, this approach should result an improved understanding of the material properties for TPP resists that can be used to create deterministic structure designs and resist chemistries tuned for desired material properties.

2.3 FUNCTIONAL REQUIREMENTS

In order to study printing parameters, the MEMS tensile tester must be able accurately characterize voxels 100 nm – 500 nm in width and integrate directly with the TPP process. With a voxel height between 2.5 [19] – 4 [20] times the width and previously reported elastic moduli of 0.8 – 2.34 GPa [4], [23], [25], the resulting in axial stiffnesses for 10 μm long voxels range 3.5 N/m to 160 N/m. That range of stiffnesses could be measured by several testers with different load cell/sensor stiffnesses or a single tester designed with a stiffness for close to the maximum, 160 N/m, and a load resolution equal to 0.1% strain for the lowest stiffness structures being measured, 35 nN. The displacement resolution is less than or equal to 0.01% strain, 1 nm, based off of previous tensile testers. The force and displacement range are set to achieve 15% strain at the maximum stiffness 160 N/m to capture plastic behavior and possibly failure. The functional requirements are list in Table 2.1.

Outside of range and resolution, the MEMS tensile tester is designed to remove sample handling to prevent any possible damage to the voxels. Two options are available:

Force		Displacement		Structure Stiffness
Resolution	Maximum	Resolution	Maximum	
35 nN	250 μN	0.25 nm	1.5 μm	~ 140 N/m

Table 2.1: Summary of functional requirements for the MEMS tensile tester.

print on an unreleased or a released tester. An unreleased tester will drastically reduce the possibly of failure due to capillary forces from the TPP resist and development process. However, the printed part will be exposed to hydrofluoric acid and the etched silicon dioxide, and the testers will be single use. A released tester can be reused once the voxel has been broken or etch away; however, the suspended features will be exposed to capillary forces and potentially fail. In order to replicate the traditional development procedure, the released tester will provide more relevant data for comparison. In order to use this method, the tester is designed to prevent stiction, or static friction.

2.4 MECHANICAL DESIGN

The MEMS tensile testers in this work is based off of Type 3 designs with the addition of an on-chip displacement sensor. Figure 2.2 is a CAD model tensile tester with the load sensor, displacement sensor, thermal actuator with heat sinks beams, and print stage at the tip of each sensor. Thermal actuation is selected to achieve the high force requirements and displacement control to maintain a constant strain-rate throughout the test [13], [15]. The load and displacement sensors are a surface micromachined differential capacitors which are used to measure the specimen elongation with sub-nm to nm resolution. In this arrangement, stress and strain data are measured electronically, freeing all optical measurements to monitor the deformation behavior of the specimen, as shown in Figure 2.2.b. Additionally, material characterization with this sensor pair can be expanded from elastic modulus, yield strength, and toughness to strain-rate dependent behavior such as fatigue and dynamic behavior for viscoelastic materials.

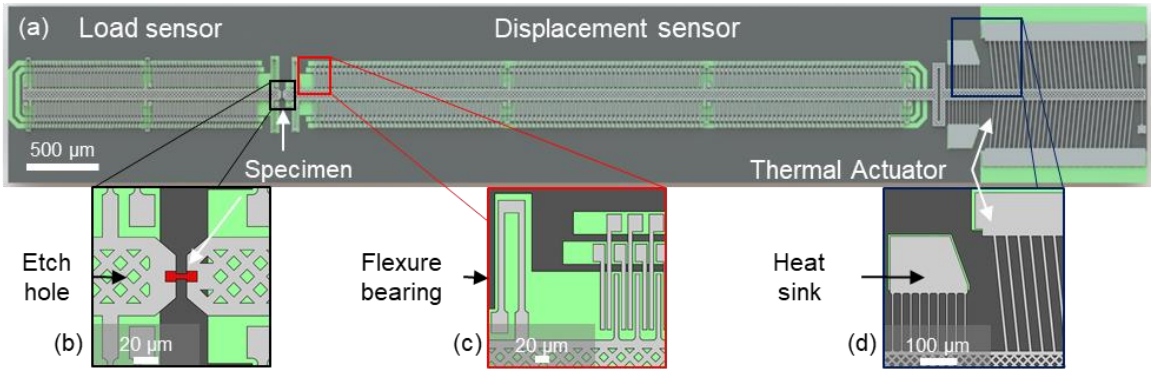

Figure 2.2: (a) CAD model of the MEMS tensile tester with closeups on (b) the specimen at the sensor tips, (c) the flexure bearing and capacitor fingers, and (d) the thermal actuator and heat sink beams.

2.4.1 Stiction

Stiction is a failure mode common in MEMS devices where drying after the wet release etch produces capillary forces large enough to permanently adhere the suspended structures to the substrate. Traditionally, MEMS devices may only encounter this failure mode once during the release etch; however, this MEMS tensile tester will be repeatedly exposed photoresist and solvents in order to achieve process integration. To prevent failure, a robust stiction analysis is conducted on all of the suspended structures. The two dominant sources of stiction in this application are capillary forces and surface-to-surface adhesion forces, as shown in Figure 2.3. Pull-in voltage, the electrostatic force great enough to pull to capacitive fingers together, is also considered during the design of the differential capacitors.

Mastrangelo and Hsu [48] developed the characteristic equations for both capillary and surface adhesion stiction, the elastocapillary and peel number respectively. The elastocapillary number, N_{EC}, determines if the elastic energy in the suspended geometry is greater than the applied capillary forces. Equation 2.1 is the N_{EC} for a cantilever beam

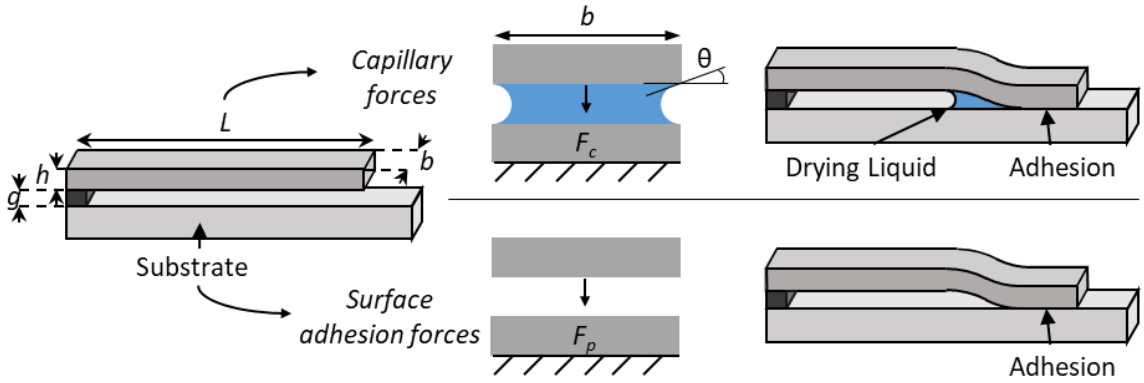

Figure 2.3: Illustration of the two dominant stiction modes with capillary on top and surface adhesion on bottom. Image adapted from [49].

$$N_{EC} = \frac{2Eg^2h^3}{9\gamma_l \cos\theta_c L^4(1 + h/b)} \tag{2.1}$$

where E is Elastic modulus, g the vertical gap between the beam and the substrate, h the beam height, γ_l the liquid surface tension, θ_c the liquid contact angle from 0 – 90 degrees, L the beam length, and b the beam width.

Even when not exposed to capillary forces, stiction can result from surface-to-surface adhesion represented by the peel number, N_P. Surface-to-surface adhesion occurs when a suspended structure comes in contact with a fixed surface, such as the substrate or capacitor fingers, and the adhesion forces prevent elastic forces from separating the surfaces. N_p for a cantilever beam is

$$N_P = \frac{3Eg^2h^3}{8\gamma_s L^4} \tag{2.2}$$

where γ_s is the solid surface tension. For both numbers, if $N > 1$ the beam will remain free, and if $N < 1$ the beam will be pinned. For designing suspended features, the Equation 2.1 and 2.2 are rewritten with $N = 1$ to determine the critical length, L_{crit}, where stiction will occur.

$$L_{crit,EC} = \sqrt[4]{\frac{2Eg^2h^3}{9\gamma_l \cos\theta_c(1+h/b)}} \tag{2.3}$$

$$L_{crit,P} = \sqrt[4]{\frac{3Eg^2h^3}{8\gamma_s}} \qquad 2.4$$

These equations are used to size the geometry of the thermal actuator beams, capacitor fingers, and geometry and placement of the flexure bearings suspending the load and displacement sensors, Figure 2.2. For the thermal actuator beams and flexure bearings, a fixed-fixed conditions is applied by scaling $L_{crit,EC}$ by 2.9 and $L_{crit,P}$ by 2.5 [50].

The placement of the flexure bearings is studied to prevent the millimeter scale shuttle from pinning. In addition, anti-stiction dimples, or hemispherical structures, are added at 60 μm, along the length of the shuttle to reduce the surface contact area where surface adhesion would occur. This is illustrated in Figure 2.4. The dimples are approximately 4 μm wide and 0.75 μm deep. Stiction analysis is conducted with a fixed-fixed boundary condition to determine the maximum spacing between the dimples to prevent the shuttle from adhering to the surface. Fixed-fixed is not an exact match for the boundary condition so safety factors should be adjusted accordingly [51]. For the shuttle 70 μm wide and 8 μm thick device layer, a dimple spacing of 60 μm results in a safety factor of 6.8. Dimples are also added at the end of the flexure bearing.

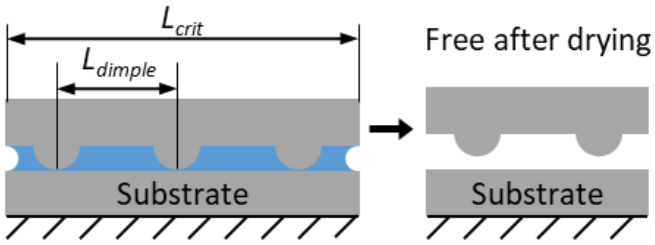

Figure 2.4: Illustration of dimples reducing the contact area of the shuttle.

2.4.2 Lumped Mechanical Model

Before designing any of the mechanical elements, a lumped mechanical model, shown in Figure 2.5, is created derive the displacement and force balance equations. The equations are used to determine the required displacement of the load sensor and force and displacement of the thermal actuator system, which includes the displacement sensor stiffness.

These equations are

$$x_{load} + x_s = x_{TA} \quad (2.5)$$

$$K_{load}x_{load} = K_s x_s \quad (2.6)$$

$$K_s x_s + K_{TA}x_{TA} = F_{TA} \quad (2.7)$$

where x is the displacement and K is the stiffness of the load sensor, *load*, specimen, *s*, and thermal actuator, *TA*, respectively. F_{TA} is the force produced by the thermal actuator. As seen in Equation 2.6 and 2.7, an estimate of the K_S is required in order to complete the mechanical design. K_S is 140 N/m for this design. The initial value of K_{load} is set to be 166.7 N/m since the maximum force on the specimen is 250 μN and the maximum elongation of the specimen, x_S, is 1.5 μN from the functional requirements.

With a polymeric test specimen, displacement control is critical to maintain quasi-static strain rates of 10^{-3} to 10^{-4} [12], [52], [53]. To do this, the design of the thermal actuator optimized for the maximum loading condition. In the unload condition, the only

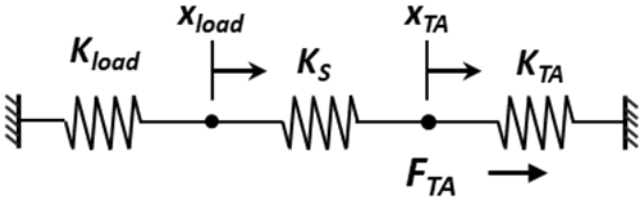

Figure 2.5: Lumped mechanical model.

resistive force is the thermal actuator itself. Solving Equation 2.7 at $F_{TA} = 0$ and substituting with Equation 2.6, x_{TA} can be written as a ratio of stiffnesses

$$x_{TA} = -\frac{K_s x_s}{K_{TA}} = -\frac{K_{load} x_{load}}{K_{TA}} \quad 2.8$$

The impact on x_{TA} by x_S or x_{load} can be reduced to ≤1% by designing K_{TA} to be ≥ 100 times the sum of K_s and K_{load}. Of course, this is a design goal, which may be limited by other goals such as the 15% desired strain.

2.4.3 Load Sensor Stiffness

The load sensor stiffness element is a double parallelogram flexure bearing where the stiffness is used to convert the sensor displacement into a force. This design is selected to limit out-of-plane motions to the tens-of-nanometer range which is critical for maintaining uniaxial loading on submicron scale features. As presented in the previous section, the initial value of K_{load} is 166.7 N/m which was found by dividing the maximum force by the maximum displacement of the specimen. K_{load} must also consider the displacement resolution of $\Delta d \leq 0.25$ nm to meet the load resolution of ≤ 35 nN. Those values result in $K_{load} = K_S = 140$ N/m. Using the same or similar displacement resolutions for both sensors can simplify the design process. Matching the two stiffnesses is a traditional approach in MEMS tensile tester design; however, it will limit the maximum force to 210 μN. For this design, K_{load} falls near the middle at 150 N/m because of capacitor geometries. Beam geometries are selected with a safety factor ≥ 1.5 of L_{crit} to prevent stiction to the substrate.

2.4.4 Thermal Actuator

The thermal actuator design for this tester balances the high force and displacement required to reach approximately 15% strain on the voxel. A chevron style thermal actuator

is selected with pairs of beams at an incline angle, θ, to direct the motion of thermal expansion with a fixed-guided boundary condition. A schematic of the structure and the free body diagram are shown in Figure 2.6. The force generated by a thermal actuator is

$$F_{TA} = 2N_{TA}EA_{TA}\alpha\Delta T \sin\theta \qquad 2.9$$

where N_{TA} is the number of beam pairs, E the Elastic modulus, A_{TA} the cross-sectional area of the beam, α the thermal expansion coefficient, ΔT the average beam temperature, and θ the incline beam angle [54].

The stiffness of the thermal actuator, K_{TA}, is

$$K_{TA} = 2N_{TA}\left(sin^2\theta\frac{EA_{TA}}{L_{TA}} + cos^2\theta\frac{Eb_{TA}^3h_{TA}}{L_{TA}^3}\right) + K_{disp} + K_{HS} \qquad 2.10$$

where L_{TA} is the beam length, b_{TA} the beam width, h_{TA} the beam height, and K_{HS} and K_{disp} the stiffnesses for the displacement sensor flexure bearings and heat sink beams. The sine and cosine terms in Equation 2.10 account for the axial and bending stiffnesses in the x axis and y axis, respectively. The double parallelogram flexure bearings used for the load sensor are also used for the displacement sensor to maintain the low out-of-plane, fixed-guided constraint at the tip. However, these bearings act solely as support structures for the shuttle because the stiffness of the thermal actuator beams dominate the overall stiffness. Heat sink beams are added between the displacement sensor flexure bearings and thermal

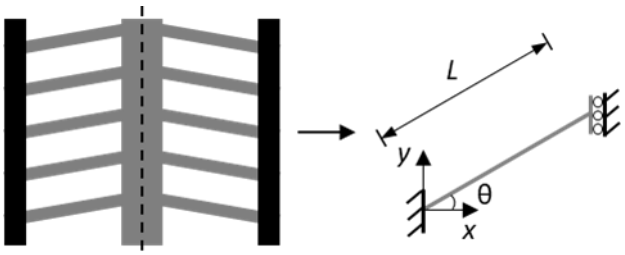

Figure 2.6: Schematic of a chevron beam thermal actuator and single beam free-body diagram with the fixed-guided boundary condition.

actuator beams, Figure 2.2.d, to reduce the temperature of the shuttle. The K_{disp} and K_{HS} equations are

$$K_{disp} = 2N_{disp}\frac{Eb_{disp}^3 h}{L_{disp}^3} \quad 2.11$$

$$K_{HS} = 2N_{HS}\frac{Eb_{HS}^3 h}{L_{HS}^3} \quad 2.12$$

where N is number of beam pairs, b the beam width, h the beam height, and L the beam length for each stiffness respectively.

2.4.4.1 Design Constraints

The thermal actuator is constrained by material selection, stiction, and beam buckling. The device layer is polysilicon, which has a recrystallization temperature 850°C [55]. During recrystallization, the resistivity of the polysilicon will change and require a new calibration curve to be generated. To account for this behavior, ΔT_{max} for the thermal actuator is constrained to 525°C.

A fixed-fixed boundary for stiction analysis is applied to displacement sensor and heat sink beams. The 70 μm width of the shuttle is also included in the length. As the dimensions of the beams are adjusted, the minimum value of $L_{crit,EC}$ and $L_{crit,P}$ sets the maximum beam length. Given the number of beams needed for the thermal actuator, a more accurate boundary condition is a plate instead of a beam. The scaling factors are 3.25 and 4.7 for elastocapillary and peel respectively [56]. $L_{crit,min}$ with a safety factor of 2 is 442.5 μm.

For Zhu *et al* [41], the key variable for improving displacement without large sacrifices in force is θ. However, there is a critical limit at 5° where beam buckling is induced. Beam buckling occurs when the compressive force in the beam passes a critical load and becomes unstable. From Figure 2.6, the fixed-guided boundary condition of the

thermal actuator restricts the free expansion of the beam in the x axis and generates compressive force along the beam length. The critical buckling force for a beam is

$$P_{cr} = \pi^2 \frac{EI_{min}}{L^2} \quad 2.13$$

where I_{min} is the minimum moment of inertia of the beam cross section. Assuming free motion of the thermal actuator, i.e. specimen and load sensor stiffness do not prevent motion, the compressive axial force of the beam is

$$R_x = \alpha \Delta T E A \frac{\cos\theta}{\frac{AL^2}{12I_{min}} sin^2\theta + cos^2\theta} \quad 2.14$$

where $AL^2/12I$ is the axial to bending stiffness ratio [41]. A minimum safety factor of 2 is set in this design to account for constrained motion by the printed part and variations in beam dimensions during fabrication.

2.4.4.2 Electrothermomechanical FEA Model

An electrothermomechanical finite element analysis (FEA) simulation is used to generate the beam thermal profile, in- and out-of-plane displacement, and the temperature at the sensor tips across the full operating range of temperatures. The model was built and run in ANSYS 17.0. The material properties for the polysilicon device layer are summarized in Table 2.2. The coefficient of thermal expansion, α, is listed at room temperature. To capture the temperature dependent behavior, a table was generated using

$$\alpha = \left(3.725[1 - exp(-5.88 \times 10^{-3}[T - 125])] + 5.548 \times 10^{-4}(T)\right) \times 10^{-6} \quad 2.15$$

where T is the temperature in Kelvin [57]. Residual stresses that may be introduced during fabrication are not included in this simulation since annealing cycles in the fabrication process used for doping should relieve the stress [45].

A room temperature boundary condition, 22°C, of the silicon chip is applied to the base of the thermal actuator, heat sink beams, and displacement sensor flexure bearings. A

Parameter	Units	Value	Reference
Elastic modulus	GPa	170	[54]
Poisson's ratio	-	0.22	[54]
Thermal conductivity	$W/m^{-1}K^{-1}$	34	[57]
Coefficient of thermal expansion	K^{-1}	2.5×10^{-6}	[57]
Resistivity	Ω·m	8×10^{-6}	[54]

Table 2.2: Summary of polysilicon material properties used in the electrothermomechanical simulation.

voltage source is applied to one side of the thermal actuator with the opposite side set to 0 V to generate the current path for Joule heating. Voltage is increased by 0.2 V steps up to 1.2 V with an average beam temperature calculated to range from 33°C to 412°C. A voltage-to-temperature curve fit is used to set the maximum voltage to 1.364 V to achieve an average beam temperature of 525°C and tip displacement of 3.52 μm. The temperature distribution and in-plane displacement for the thermal actuator at 1.364 V are shown in Figure 2.7.

The simulated results are within 2% of the analytical $x_{TA} = 3.45\ \mu m$ at $\Delta T = 525°C$. The maximum orthogonal (Z-axis in Figure 2.7) and normal (Y-axis in Figure 2.7) out-of-plane displacements are 0.076 nm and 1.6 nm which are negligible when compared to the width and height of the voxels. The normal displacement at the tip is attributed to the temperature raise of 2.5°C at the displacement shuttle tip. This small ΔT_{tip} will limit any thermal effects on the polymer specimen during testing.

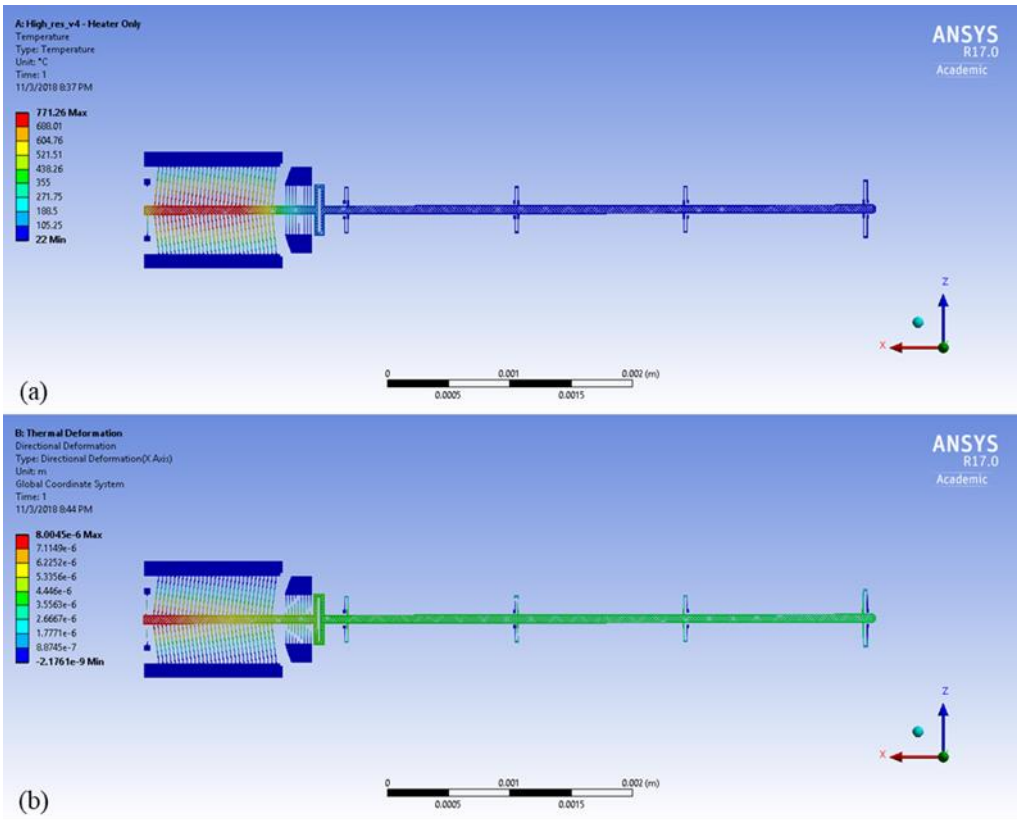

Figure 2.7: Temperature distribution and in-plane displacement from the thermal actuator to the tip of the displacement sensor.

2.4.4.2 Thermal Management System

In order to maintain the room temperature boundary condition in the previous section, a passive thermal management system was designed. A 1D steady-state conduction thermal resistance model was developed from the thermal actuator beam through the air, silicon chip, heat spreader in the package (see Section 3.2), and into a heat sink to determine the thermal resistance of system. The model shown in Figure 2.8 also uses Artic MX-4 thermal paste to reduce the contact resistance between separate components. The conduction equations are

$$q_{air} = \frac{Sk_{air}A_{air}(T_{TA} - T_{sub})}{g} \quad 2.16$$

$$q_{si} = \frac{k_{si}A_{si}(T_{sub} - T_2)}{L_{chip}} \quad 2.17$$

$$q_{Al} = \frac{k_{Al}A_{Al}(T_3 - T_4)}{L_{Al}} \quad 2.18$$

$$q_{paste} = \frac{k_{paste}A_{paste}\Delta T}{L_{paste}} \quad 2.19$$

$$q_{HS} = \frac{(T_5 - T_{HS})}{R_{HS}} \quad 2.20$$

where q_i the heat across the layer, k_i the thermal conductivity, A_i the cross-sectional area, T_i the surface temperature, L_i the length of the heat path, g the height of the air gap below the thermal actuator beams, and S the beam shape factor [57], [58].

A simplified shape factor for the rectangular cross-section beam is

$$S = \frac{h}{b}\left(\frac{2g}{h} + 1\right) + 1 \quad 2.21$$

where h and b are the height and width of the beam [57], [58]. L_{chip} is the silicon equivalent thickness for the silicon nitride, silicon, polysilicon, and silicon oxide layers on the chip. A list of material properties and dimensions is presented in Table 2.3. The maximum air gap between the device and the substrate, g, is 3.5 μm, which is set by fabrication constraints.

Figure 2.8: 1D thermal resistance model from the temperature at the thermal actuator beams, T_{TA}, to the surface temperature of a heat sink, T_{HS}.

Material (Units)	Thermal Conductivity (W/m·K)	Length (μm)	Area (mm^2)
Air	0.026	3.5	0.026
Silicon	300	900	6
Arctic MX-4 paste	7	20	6,14.28
Aluminum	237	1.62×10^3	14.28
Copper	400	-	-

Table 2.3: Material properties and dimensions for the 1D thermal resistance model.

The substrate boundary condition, T_{sub}, from the FEA model is solved for using the equilibrium conditions at the substrate

$$2N_{TA}q_{air} = q_{si} + q_{Al} + 2q_{paste} + q_{HS} \quad 2.22$$

where $2N_{TA}$ scales the conduction through air by the thermal actuator beams. The resistance of the heat sink, R_{HS}, can be solved

$$R_{HS} = \frac{R_{air}(T_{sub}-T_{HS})}{2N_{TA}(T_{TA}-T_{sub})} - \left(R_{si} + R_{Al} + 2R_{paste}\right) \quad 2.23$$

where T_{TA} is the average temperature of thermal actuator beams, T_{HS} the surface temperature of the heat sink, and R_i is the thermal resistance for each layer in the form of $L_i/(k_iA_i)$. Values of R_{HS} are determined to keep $T_{sub} \leq 323\ K$ with $T_{TA} = 798\ K$. From Figure 2.9, R_{HS} values need to be less than 14 K/W, 7 K/W, and 1 K/W for $T_{HS} = 278, 288,$ *and* $298\ K$, respectively.

While traditional finned or fan cooled heat sinks can reach resistances in these ranges, the size required to reach the T_{HS} are too large for the test setup (See Calibration section). However, heat pipes which use a liquid-to-vapor phase change to enhance heat transfer can reach resistances as low as 0.1 K/W and move the heat away from the source freeing space for a large sink. A heat pipe is a vacuum sealed metal pipe with a wicked structure surrounding the inside diameter and a working fluid. As illustrated in Figure 2.10, as the high temperature side of the copper pipe heats up it (1) exceeds the working

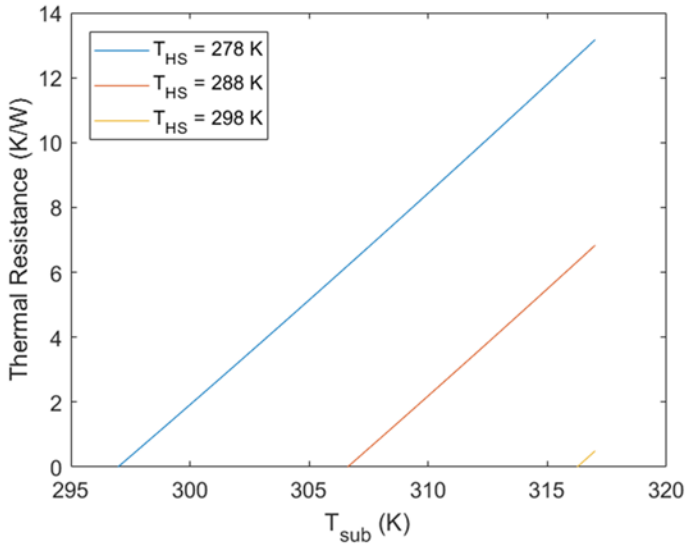

Figure 2.9: Required thermal resistance for the heat sink, R_{HS}, at three different boundary temperatures *278 K*, *288 K*, and *298 K*.

temperature and the water evaporates, (2) the vapor flows toward the low temperature side and (3) condenses into the wick, and (4) the liquid water wicks back towards the hot side, and the process is repeated. Phase change heat transfer and wicking structures allows for thermal resistances < 0.1 K/W even with a cross-sectional profile less than 10 mm thick.

A thin heat pipe, a copper mount, and a condenser block are added to the thermal resistance model in place of the heat sink. The copper mount acts as the package heat sink and connects to the heat pipe. On the heat pipe, the package is the high temperature side and a 3D printed ABS condenser block is the low side. Again, thermal paste is used between each structure to reduce thermal contact resistance. The updated thermal resistance model is used to 1) determine the heat conducted through the heat pipe, 2) select a commercially available heat pipe, and 3) size the condenser wall thicknesses and chamber volume to maintain a T_{sub} = 303 K with the chamber filled with ice for 1 hour.

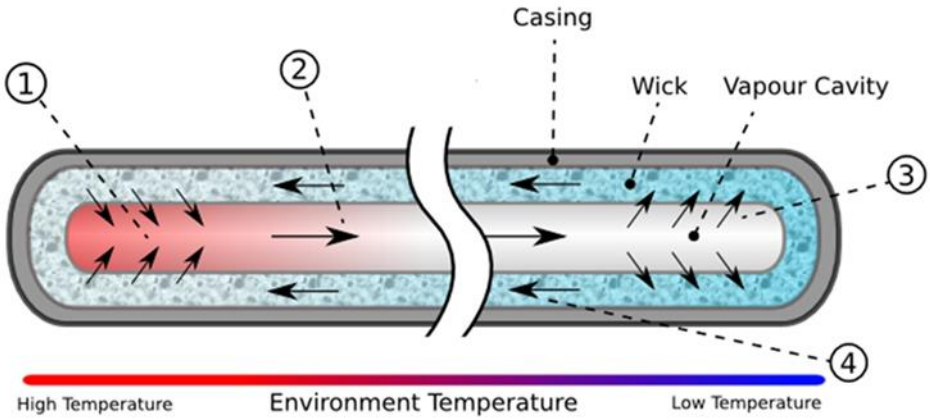

Figure 2.10: Illustration of the phase change heat path within a heat pipe [59]. At (1) the high temperature source evaporates the liquid water, and the vapor begins to flow to the low temperature side in (2). Once at the low temperature side, the vapor condenses and is absorbed by the wicking material (3), which pulls the liquid water back to the high temperature side. The phase change cycle continues until a steady-state condition is met or the low side temperature cannot condense.

Using Equation 2.22, the heat pipe power rating needs to be greater than 2.5 W. A 200 mm long, 10 mm wide, and 4.5 mm thick heat pipe is selected to fit within the setup constraints and allow for a 75 mm long condenser. The approximate resistance is 0.178 K/W. The wall thickness between the heat pipe and ice is 2 mm. The chamber volume is approximately 60 mL. With the low side temperature around 278 K, the efficiency of the heat pipe will reduce. Assuming a 50% reduction, T_{sub} increases to 303 K, or 30°C. While this value does not match the room temperature boundary condition, the resulting T_{tip} increase can be bounded to twice the FEA value at 5°C.

2.4.5 Results

The thermal actuator design has 30 beam sets that are each 320 μm long, 8 μm wide, 8 μm tall, and a 6° incline angle. With $K_{disp} = 1.4\ kN/m$ and $K_{HS} = 1\ kN/m$, the total stiffness of the thermal actuator unit is $K_{TA} = 25.9\ kN/m$. This results in a displacement-controlled

stiffness percentage around 1.16%. At $\Delta T = 525°C$, the unloaded actuator produces 89.6 mN of force. When loading a constant $K_S = 140\ N/m$, the load sensor stiffness deforms 1.66 μm or 250 μN, and the displacement sensor travels 3.44 μm providing 17% strain to a 10 μm voxel. The stiction and buckling safety factors are ≥ 1.2 and 7.3 respectively. A 200 x 10 x 4.5 mm^3 copper-water heat pipe and 3D printed condenser provide the thermal management system to keep the sensor tip temperature below 35°*C* during testing.

2.5 CAPACITIVE SENSOR DESIGN

The MEMS tensile tester in this design uses on-chip sensing capabilities for the load and displacement of the voxel. On-chip sensing generates high speed and accurate real-time measurement data while enabling additional techniques, such as optical monitoring of the sample, to quantify the behavior of the voxel during the test. In order to achieve the desired range and resolution, surface micromachined style differential capacitors are used for the gain and low parasitic behavior. The sensors are designed to connect to the MS3110 IC capacitive readout from Irvine Sensors. Previous researchers have demonstrated a noise floor of 0.5 mV [42] and the potential for ≤ 1 nm displacement resolution. Additionally, a design for a lock-in amplifier circuit is presented in this section. The lock-in amplifier allows for a larger range of sampling frequencies and the potential for a lower noise floor at slower sampling rates.

2.5.1 Surface Micromanufacturing Capacitor Design

The on-chip sensors for this design are surface micromachined style differential capacitors. This style of sensing is selected for a 5 times higher gain than the traditional parallel plate design and at least double the density of the tri-plate design. Each capacitive unit, shown Figure 2.11, consists of one moving finger attached to the central shuttle, *M*,

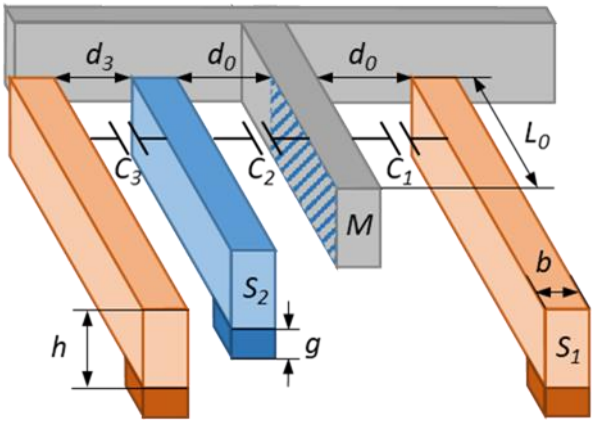

Figure 2.11: Schematic of differential capacitor with labels. The blue gradient pattern on the M beam represents the initial overlap area, A_1.

and two stationary fingers, S_1 and S_2. Initially, the gaps between the moving finger and the stationary fingers are equal, d_0. As the shuttle is displaced, one gap increases and the other decreases generating a change in capacitance, ΔC, proportional to the change in displacement, Δd.

$$\Delta C = 2n\varepsilon l_o h \frac{1 + 2(C_3/C_0)}{d_0^2} \Delta d \qquad 2.24$$

where n is number of differential units, ε the permittivity of air, l_o the overlap length, h the finger height, C_3 the capacitance between the fixed fingers S_1 and S_2, and C_0 the capacitance between M and S at d_0 [54].

The individual capacitance values from Figure 2.11 are

$$C_1 = n\varepsilon \left(\frac{A_1}{d_0 + \Delta d} + \frac{A_2}{g} + 0.65 \frac{A_1}{h} \right) \qquad 2.25$$

$$C_2 = n\varepsilon \left(\frac{A_1}{d_0 - \Delta d} + \frac{A_2}{g} + 0.65 \frac{A_1}{h} \right) \qquad 2.26$$

$$C_3 = n\varepsilon \left(\frac{A_1}{d_3} + 0.65 \frac{A_1}{h} \right) \qquad 2.27$$

where A_2 is the overlapping area of the stationary capacitors, S_1 and S_2, and the substrate below, g the vertical gap between the base of the fingers and the substrate, and h the finger height. The first term in C_1 and C_2 is the capacitance between S_1 (S_2) and M, the second

term is the capacitance between S_1 (S_2) and the substrate, and the third term is the fringe effect for S_1 (S_2). The capacitance between S_1 and S_2 is the first term in C_3 [54].

The design of the capacitors starts with examining the functional requirements, mechanical design, and sensing electronics to determine the ΔC and Δd. As presented in the load sensor stiffness design, selecting the same or similar sensing resolution as the desired displacement resolution can simplify the design process. For this design the load sensor and displacement sensor Δd are 0.2 nm and 0.25 nm respectively.

With the displacement resolution, the next parameter from Equation 2.24 is ΔC. ΔC set based off noise approximations and the measurement range. The minimum value of ΔC is 0.09 fF, which is the output noise value at the lowest cutoff frequency for the MS3110 IC, 500 Hz. While Espinosa has reported values as low at 0.05 fF [42], the more common limit is 0.1 fF [37], [38]. This value will be set the minimum ΔC. The maximum value of ΔC is set by examining the sensor range from the mechanical design section, the input capacitance range of the sensing electronics, and the output voltage range.

The maximum displacement for each sensor from the Section 2.4.5 is 1.66 μm and 3.44 μm for the load and displacement sensor respectively. With a resolution of 0.2 nm and 0.25 nm, the number of measurements for the load and displacement sensor are 8300 and 13,760 respectively which will result in the total ΔC read by the electronics. However, due to the differential design, the total ΔC will be captured by increasing C_1 and decreasing C_2 or vice versa. So, the sum of the sensor capacitance values must not exceed the 9.75 pF maximum input capacitance range for the MS3110 IC, but this also includes C_3, the on-chip capacitances for tuning the output voltage, and any uncancelled parasitic capacitance values. A safe assumption would be to assign 2 pF for the on-chip capacitors and 2 pF for parasitic capacitance of the package leaving 5.75 pF of the input remaining. A simple approach is to divide the value by 3 which results in maximum ΔC values of 0.23 fF for

the load sensor and 0.14 fF for the displacement sensor. Of course, checks are put into place during the design to prevent exceeding this value.

The voltage range and gain from the sensing electronics are checked to determine what output voltages is required to meet the measurement range for each sensor. 3.5 V is the maximum listed sensing range for the MS3110 IC, and that results in a 0.42 mV and 0.25 mV voltage floor for the load and displacement sensor respectively. Using the 0.42 mV load sensor voltage floor and the minimum ΔC = 0.09 fF, the maximum gain required is 4.7, which falls into the optimized range of 0.26 – 6.84 range at ΔC = 0.09 fF.

From the comparison, an initial value of ΔC will set in the middle at 0.115 fF. The remain variable for the capacitor design are finger geometry and number of differential pairs. Just like in the mechanical design, the first step is to analyze the sources of stiction and develop dimension limits.

2.5.1.1 Stiction

There are three sources of stiction for the capacitor fingers: 1) pull-in voltage, 2) capillary forces, and 3) surface-to-surface adhesion. Pull-in voltage occurs when the applied voltage results in an electrostatic force greater than the stiffness of the finger. The pull-in voltage, V_p, equation is

$$V_p = \sqrt{11.9 \frac{E d^3 b^3}{\varepsilon L_{fb}^4}} \tag{2.28}$$

where E is elastic modulus, d the gap between fingers, b the finger width, ε the permittivity of air, and L_{fb} the total length of the folded beams. With the MS3110 IC, the applied voltage of 2.25 V will displace, or pull-in, a capacitive finger by 0.285 μm. This value is added to the maximum displacement from the mechanical analysis and acts as the minimum value of d_0 to prevent pull-in during testing [50].

Capillary and surface adhesion are accounted for by determining the fixed-free $L_{crit,EC}$ and $L_{crit,P}$ from out-of-plane forces, finger and substrate, and in-plane force, finger and neighboring finger. $L_{crit,P}$ sets the maximum finger length due to out-of-plane forces. This value is used to set the length of the exterior stationary finger, S_1 in Figure 2.11. Fabrication constraints are used to set the maximum length of the interior finger, S_2, to be 30 μm shorter than S_1, and for the maximum overlap length, l_0, to be 12 μm less than S_2. This condition quickly drives the capacitor finger height, h, from an initial value of 2 μm up to 8 μm and the vertical gap, g, up to 2.5 μm. Both values are set by fabrication constraints presented later in this chapter. Safety factors for the out-of-plane stiction are set to 1.5.

Lateral stiction is used to set the minimum for finger width, b, and the capacitor gaps, d_3 [49]. d_0 is also evaluated for stiction; however, the displacement range is used to set that value. For the in-plane case, Equation 2.3 and 2.4 are modified as follows: g is the smaller value of d_0 or d_3, h is b, and b is h. The safety factor for the in-plane stiction is set to 1.5 for IPA.

The vertical stiction limitation on l_0 limit $\Delta C \approx 0.1$ fF, which can only be achieved through large increases the number of capacitive units. A plot in Figure 2.12 shows how the number of units dramatically increase the footprint, and shuttle length, to achieve a desired ΔC and for a given Δd. The increase in shuttle length leads to a re-evaluation of the stiffnesses in the mechanical design section and results in an iterative process.

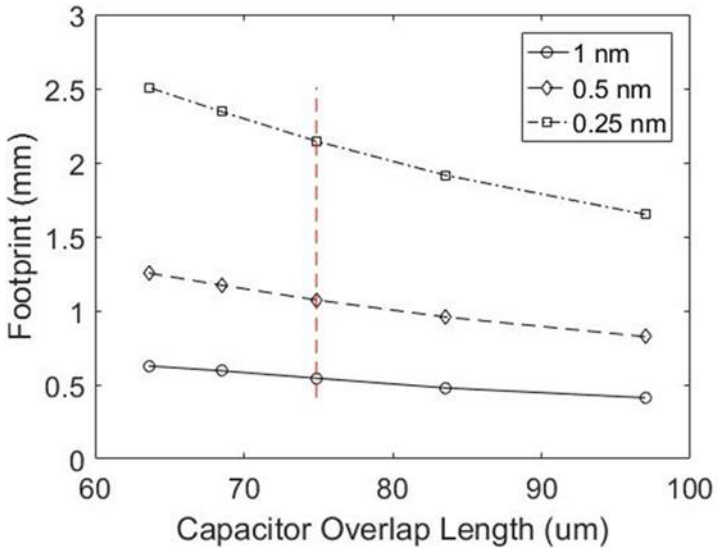

Figure 2.12: Sensor footprint vs. number of capacitor units to achieve $\Delta C = 0.1\ fF$ at Δd values of 0.25 nm, 0.5 nm, and 1 nm. The red line represents a selected overlap length.

2.5.2 Sensing Electronics

The sensing electronics for this study are selected or designed to have low noise and high sensitivity to measure and apply the sub-fF capacitance changes. The two most common circuits in literature are the MS3110IC capacitive readout from Irvine Sensors and an AC integrator with a lock-in amplifier. The MS3110IC is specifically designed for differential measurements with low capacitance resolution, 4 aF/rtHz, and to be placed in close proximity of the device to lower noise and increase response time [54]. The lock-in amplifier circuit prevents signal integration with the feedback resistor and achieves low noise by providing a reference signal of the same frequency [60]. Both circuits will be evaluated in this thesis.

2.5.2.1 MS3110 IC Capacitive Readout

The MS3110 IC is a commercially available differential capacitive circuit design for low noise MEMS sensing applications. The circuit shown in Figure 2.13 supplies alternating square wave signal to the fixed-fingers of the capacitors and returns the signal through the moving shuttle. Two on-chip capacitors, CS1 and CS2, allow the user to either balance the capacitance or tune the output voltage, V_o. The signal is amplified and filtered and amplified again before output the signal. The first amplifier uses a feedback capacitor, and the second is a buffer.

From the MS3110 IC circuit, the output voltage, V_o, is

$$\Delta V_o = \frac{G_{buffer} V_{2.25}}{C_f}[(CS2 - CS1) + \Delta C] \qquad 2.29$$

where G_{buffer} is the buffer gain of 2 or 4, $V_{2.25}$ the supply voltage to the capacitor and amplifier reference, and C_f the tunable feedback capacitor. The gain can be tuned from 0.2315 – 6 V/pF for the optimized range. As presented in an earlier section, this range will work for both sensors.

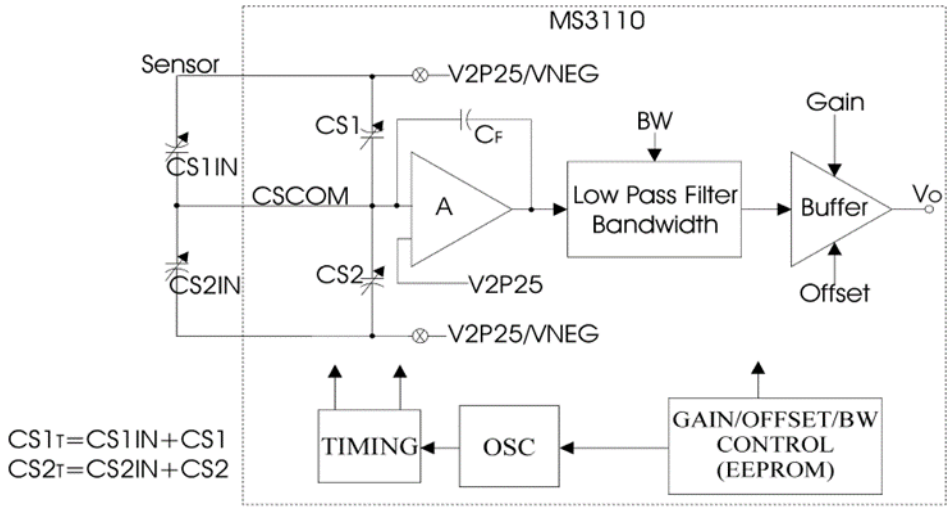

Figure 2.13: Diagram MS3110 IC circuit where CS1IN and CS2IN represent the differential capacitors from the on-chip sensors [61].

2.5.2.2 Lock-in Amplifier

The second method for measuring the change in capacitance of the load and displacement sensor is an AC integrator paired with a lock-in amplifier. An LTspice circuit show in Figure 2.14. The circuit design was supplied by Jason Gorman of the National Institute of Standards and Technology. David Cayll, a member of Dr. Cullinan's lab, selected components and built the circuit at the University of Texas at Austin.

For the lock-in amplifier, the output voltage, V_o, is

$$V_o = \frac{V_{ref}\Delta C}{2C_f} \tag{2.30}$$

where V_{ref} is the AC voltage supplied to the sensors and C_f the feedback capacitor. With the addition of a feedback resistor, R_f, the op-amp behaves as an AC integrator and provides an additional gain to V_o based on the cutoff frequency, ω_c. The equation for the ω_c is

$$\omega_c = \frac{1}{R_f C_f} \tag{2.31}$$

R_f is set to be 160 kΩ to balance ω_c with thermal noise. With C_f = *10 pF*, the gain from the integrator is 32 dB. Similar to the on-chip capacitors of the MS3110 IC, a custom integrator circuit allows for tuning by changing the magnitude of R_f, C_f, and V_{ref}.

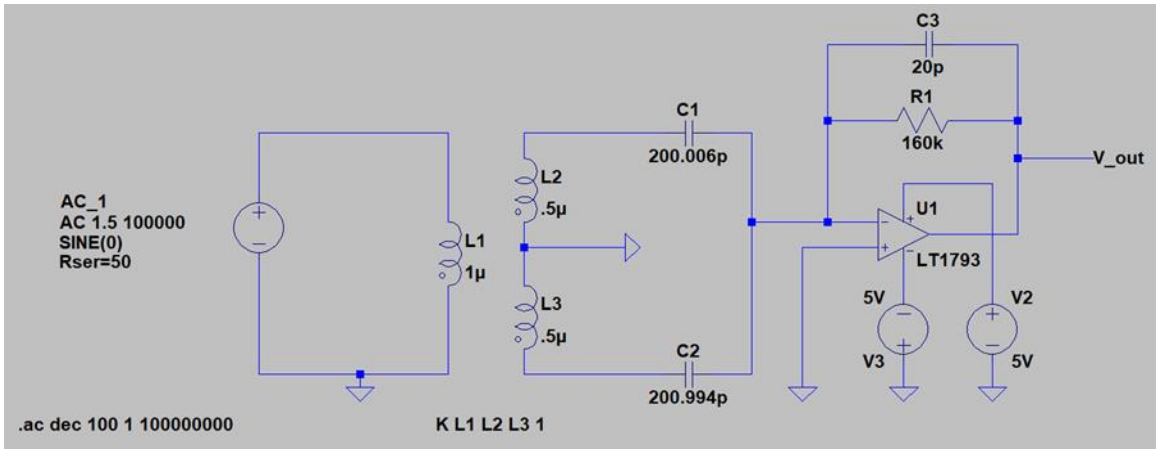

Figure 2.14: LTspice circuit of the AC integrator portion of the circuit. A Magnetics SP-67 transformer supplies the reference voltage to C_1 and C_2.

2.5.3 Results

The resulting sensors are both designed to achieve a $\Delta C = 0.1\ fF$. This is because the stiction and fabrication constraints limited the design to low sensitivity variables: n, b, d_0, and d_3. All fingers are 8 μm thick and are suspended 2.5 μm above the substrate. Load sensor fingers are 5 μm wide and have an overlap length of 83 μm. The 126 capacitive units result in $C_1 = C_2 = 0.55$ pF with $d_0 = 2.5\ \mu m$ and $C_3 = 0.31$ pF with $d_3 = 3\ \mu m$. Displacement sensor fingers are 6.5 μm wide and have an overlap length of 80 μm. The capacitor values of the 252 capacitive units are $C_1 = C_2 = 0.96$ pF with $d_0 = 4\ \mu m$ and $C_3 = 0.59$ pF with $d_3 = 3\ \mu m$. The sum of the capacitors for both sensors are well within the allotted 5.75 pF. In- and out-of-plane stiction SF are 1.5 with the peel number limiting out-of-plane geometry, l_o, and elastocapillary limiting the in-plane geometry, b, d_0, and d_3.

2.7 Fabrication Constraints

Fabrication constraints are used to set minimum and maximum values for geometry of the device. For this work, the constraints are minimum gap size, minimum feature size, and polysilicon device layer thickness. The minimum gap size is set to 2.0 μm by the MA6 contact aligner at the Microelectronics Research Center, MER. This value will limit the gap size between the capacitor fingers, d_0 and d_3, and the width of the fingers, b. The minimum feature is set to 5 μm to increase fabrication yield [54]. The time required for the layer deposition and doping process limit the polysilicon thickness to 8 μm. Deposition at MER is limited to 1 – 1.1 μm to prevent damage to the tube furnace gaskets, which take 8.5 hours. Every 2 layers, the wafer is doped at 1050°C and cleaned which takes an additional 7 hours and brings the minimum time for 2 layers to 24 hours. The 8 μm maximum was selected to finish the layer within a single work week to allow for

monitoring and consultation from the MER technicians. In the case of tube damage, technicians could clean the quartz tube over the weekend to minimize process downtime.

2.8 DESIGN RESULTS

The design of the MEMS tester tensile is an iterative cycle between the mechanical and sensing capacitor design. The flowchart of the design process is shown in Figure 2.15. Prior to the iteration process, material properties, operating conditions, and safety factors are set. Material properties for the polysilicon device layer are E = 170 MPa and $\alpha = 2.5*10^{-6}$ [54], [57]. ΔT for the thermal actuator is fixed to 525°C to limit recrystallization. ΔC resulted in 0.1 fF to exceed the output noise value of 0.09 fF at the lowest cutoff frequency for the MS3110 IC, 500 Hz, and stay within the input capacitance range of the MS3110 IC. Safety factors for buckling, out-of-plane and in-plane stiction of the fingers, flexure bearings and thermal actuator, and dimple spacing are 1.5, 2, and 3 respectively. With the fixed values set, the iteration process begins.

With the design approach above, the tensile tester is designed with the performance in Table 2.4. Figure 2.16 shows a fabricated voxel tensile tester. The device layer thickness and air gap reach the maximum values set by the fabrication constraints of 8 μm and 2.5 μm to prevent out-of-plane stiction of the capacitive fingers. The voxel tensile tester design is driven by the required force and displacement resolution. The thermal actuator design is 30 beam sets of 320 μm long, 8 μm wide, and a 6° incline angle. $\Delta C = 0.1\ fF$ is achieved at $\Delta d_{load} = 0.2\ nm$ and $\Delta d_{load} = 0.25\ nm$ by increasing the number of capacitive units, $N_{load} = 126$ and N_{disp} = 252. The overall scale of the tensile tester is addressed by adding additional flexure bearing at even intervals along the shuttle length of the sensor. Two full sets of flexure bearings are used to support the displacement sensor and one and a half sets of flexure bearings are used to support the load sensor on the voxel tensile tester.

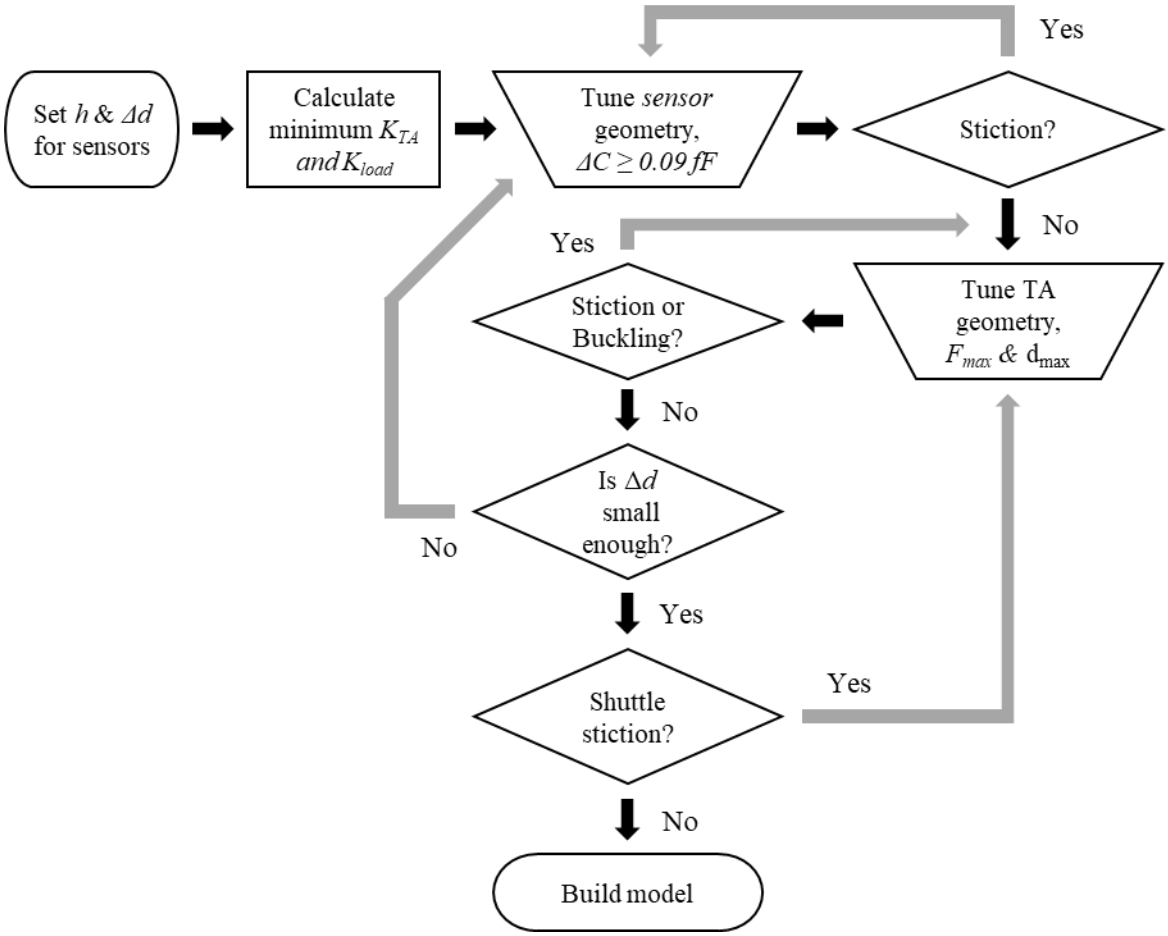

Figure 2.15: Design iteration flow chart.

	Force		Displacement		Structure Stiffness
	Resolution	Maximum	Resolution	Maximum	
Required	35 nN	250 µN	0.25 nm	1.5 µm	~ 140 N/m
Designed	**30 nN**	250 µN	0.25 nm	**3.4 µm**	

Table 2.4: Designed force and displacement range and resolution with the required values.

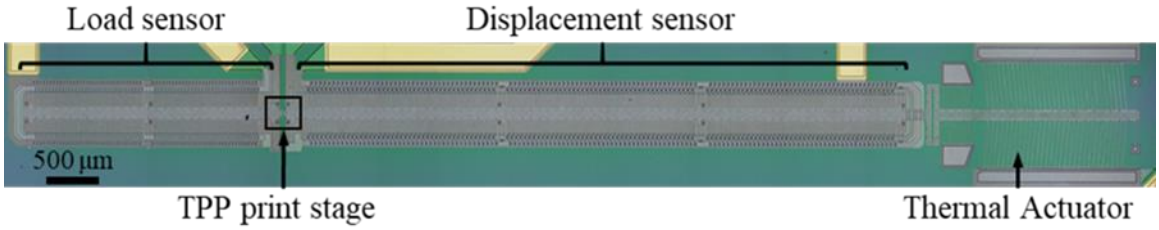

Figure 2.16: Fabricated custom MEMS tensile tester.

Chapter 3 – Microfabrication and Packaging

In this chapter, a detailed micro-fabrication process flow and packaging design for the tensile tester device are presented. The designed 8 μm device layer required a rearrangement of steps in the traditional PolyMUMPs approach used. A custom printed circuit board (PCB) is developed for both simple integration into the Nanoscribe GT laser system and to enable control with a thermal management system. All micro-fabrication was performed in the Microelectronics Research Center (MRC) at The University of Texas at Austin.

3.1 Microfabrication process

The MEMS tensile testers were fabricated using a modified variant of the PolyMUMPs process, which has been developed for multi-layer polysilicon devices. The process starts with a single side polished, 500 μm thick, 100 mm n-type silicon wafer. The process flow is illustrated in Table 3.1. First, a Piranha solution of one-part hydrogen peroxide and two-parts sulfuric acid is used to clean the wafer of any contaminants. After the clean, the wafer is placed into a low-pressure chemical vapor deposition (LPCVD) horizontal tube furnace to deposit a phosphosilicate glass (PSG) layer via phosphorus oxychloride ($POCl_3$). A 30 minute 1050°C anneal in an atmospheric horizontal tube furnace is used to drive in the dopant. These steps increase the dopant level at the surface to reduce the charge feedback from the electrostatic capacitors to the substrate [54]. Next, the wafer is cleaned in the Piranha solution, and the PSG layer is stripped with 1:20 solution of 49% hydrofluoric acid (HF) and deionized water (DI). After the clean, the wafer is placed in an LPCVD nitride furnace and 600 nm of silicon nitride is grown on the wafer. The silicon nitride layer acts as a HF resistant electrical insulator between the tensile tester components and the wafer.

With the wafer preparation complete, a cleaned wafer is placed in a LPCVD furnace, and 1 μm of amorphous silicon is deposited. Amorphous silicon is deposited instead of polysilicon in order to reduce the initial resistivity of the layer [45]. A 200 nm layer of spin-on dopant P509 from Filmtronics is spun on and heated to form a solid dopant film. The spin-on dopant is used instead of the $POCl_3$ due to the > 1 μm doping depth [62]. The wafer is placed into an annealing furnace for 30 minutes at 1050°C to drive in the phosphorous dopant and induce gain refinement and growth to form polysilicon [55]. A buffered oxide etch (BOE) removes the dopant layer after the annealing step. Photolithography with Poly 1 mask is used to pattern the structural and electrical base of the tensile tester and the alignment markers. A deep reactive ion etching (DRIE) is used to remove the unwanted material. The photomasks for this fabrication process can be seen in Appendix A.

With the base complete, the photoresist from Poly 1 is removed with a Piranha clean. A second clean with an HF:DI bath is used to prepare the wafer for thermal oxide growth. The second clean is required to prevent cross-contamination of polymers into the tube furnaces. The wafer is placed in a low temperature oxide (LTO) furnace, and 1 μm of LTO is grown. Photolithography with Oxide 1 mask is used to define a planarization layer. This mask is a negative of the Poly 1 mask with 4 μm to 8 μm larger features to account for misalignment. This step produces a 1 μm layer under the thermal actuator to match the 1 μm layer of polysilicon under the displacement sensor shuttle. This planarization layer limits out-of-plane motion or loading due to the step change between the thermal actuator beams to the displacement sensor shuttle. Reactive ion etching (RIE) is used to remove the unwanted oxide and expose the Poly 1 features. After another cycle of cleaning, a 2.5 μm layer of LTO is grown to create the air gap below the suspended features of the tensile tester. Photolithography is used to pattern the negative version of Oxide 2 mask. RIE

removes the material to expose the contact pads to connect the subsequent polysilicon layer with the Poly 1 layer. Piranha solution is used to remove the photomask.

Prior to the amorphous silicon deposition, photolithography is used to pattern the 2 μm squares holes of the Dimples mask onto the wafer. BOE isotropically etched 750 nm deep hemispheres into the top surface of Oxide 2. After another two cycles of Piranha cleaning, the amorphous silicon deposition and doping process for the 8 μm polysilicon, device layer began. Two 1 μm layers are deposited in a row. The deposition is limited to 1 μm to prevent overloading the seals on the door and gases, which could result in system leaks and variations in material properties. The first layer fills the hemispheres on Oxide 2 to form dimples put in place to reduce stiction under the shuttles. After the second layer, the wafer is removed from the furnace, Piranha cleaned with a HF dip, and the 200 nm spin-on dopant is applied. A 30 minute anneal at 1050°C is used to dope the 2 μm layer, and a BOE removes the dopant layer. This process is repeated three more times to form the 8 μm polysilicon device layer.

In a traditional PolyMUMPS process, the next steps would be to pattern and etch the polysilicon layer, deposit any additional insulating materials, and finish with metallization; however, a traditional second polysilicon device layer is only 2 μm to 3 μm. The large increase in height produces a more challenging surface topography for uniform photoresist layers. This is especially true for the metallization step which utilizes a bi-layer liftoff recipe with a 1 μm thick base layer. In order to improve the layer uniformity, this fabrication process moved the polysilicon patterning and etching steps after the metallization step. This reduces the maximum step change across the wafer to a low density of 2.5 μm holes instead of a high density of 8 μm trenches from the capacitor fingers.

Next, the wafer is cleaned in preparation for a 600 nm deposition in the LPCVD nitride furnace. Photolithography with the Nitride 2 mask is used to pattern features for

electrical insulation and increased adhesion. RIE is used to remove unwanted silicon nitride and open contacts between the polysilicon device layer and the metallization layer. After the photomask is removed and wafer cleaned, a bi-layer liftoff resist with LOR 5A as the base layer is spun onto the wafer. Photolithography with the negative of Gold 1 mask is used to pattern top resist layer. By increasing the development time, the LOR 5A is undercut by less than 1 μm to form a 'T' like structure. Electron beam deposition is used to deposit 10 nm of chromium for adhesion and 300 nm of gold to form the electrical traces and bond pads. During the deposition, the overhang in the 'T' like structures separates the gold on top of the photoresist from the gold on the wafer. The bi-layer resist and unwanted gold are released from the wafer with two baths in Remover PG at 80°C for 2 hours and 30 minutes followed by a 30-minute bath in IPA. Any residue or gold flakes are removed by spraying the wafer with acetone, methanol, and IPA.

With the metallization complete, photolithography with Poly 2 mask is used to pattern the remaining device features: capacitor fingers, shuttles, flexure bearings, thermal actuator beams, and the support structures for the electrodes and bond pads. Alignment of this mask is critical to align the all of the contact pads between the layers and to cover all of the gold to prevent sputtering during plasma etching. DRIE is used to remove the unwanted polysilicon. Control of the etching parameters is critical to maintain desired feature sizes and account for the aspect ratio dependent lag. With all of the tensile tester features defined, a protective photoresist layer is applied and the wafer is diced into individual chips. Alignment markers in the Poly 1 and Oxide 1 layers are used for x-y positioning and rotation correction for the dicing paths.

Individual chips are cleaned with acetone to remove the protective photoresist and 25 minutes in Nanostrip is used to remove the hardened Poly 2 photoresist mask without attacking the gold film. A recipe developed at Tufts is used to remove Oxide 1 and 2 with

a BOE and DI solution. Prior to being placed in the etchant, the chips are submerged in acetone and IPA for 10 minutes each to reduce the probability of bubble formation which would result in localized etch masking. Chips are etched in the BOE:DI solution for 90 minutes and cleaned with another set of 10-minute baths in acetone and IPA. Once dry, the devices are ready for packaging.

Step	Machine	Description	Comment	
1	Undoped Acid Hood C14	Undoped Piranha Clean	Si Wafer (View at sensor tips)	
2	Diffusion Doping $POCl_3$ – MRL	Diffusion doping	PSG Layer	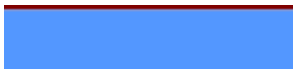
3	Anneal (Doped) – MRL	1050°C Thermal Anneal	Drive-in dopant	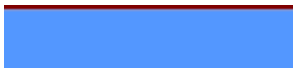
4	Doped Acid Hood C16	BOE etch of PSG		
5	Doped Acid Hood C16	Piranha Clean and HF dip		
6	LPCVD Nitride – MRL	Deposit 600 nm of silicon nitride		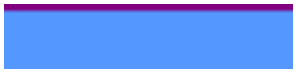
7	Doped Acid Hood C16	Piranha Clean and HF dip		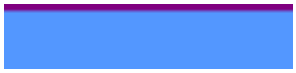
8	LPCVD Amorphous Silicon - MRL	Deposit 1 µm Amorphous Si		
9	Solvent Hood J23	Spin-on 200 nm of P509	Spin-on PSG layer	
10	Anneal (Doped) – MRL	1050°C Thermal Anneal	Anneal Poly-Si	
11	Doped Acid Hood C16	BOE etch of PSG		

Table 3.1: Processing steps for tensile

12	HDMS/Hood L10/MA 6 mask aligner	Lithography	Poly 1, positive	
13	PlasmaTherm DSE	DRIE	Remove 1 µm Poly-Si	
14	Photoresist Acid Hood H14	Piranha Clean	Remove resist	
15	Doped Acid Hood C16	Piranha Clean and HF dip		
16	LPCVD LTO - MRL	Grow 1 µm LTO		
17	HDMS/Hood L10/MA 6 mask aligner	Lithography	Oxide 1, positive	
18	PlasmaTherm II, Right chamber	RIE Oxide Etch	Remove 1 µm LTO	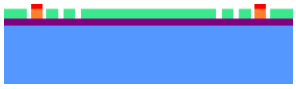
19	Photoresist Acid Hood H14	Piranha Clean	Remove resist	
20	Doped Acid Hood C16	Piranha Clean		
21	LPCVD LTO - MRL	Grow 2.5 µm LTO		
22	HDMS/Hood L10/MA 6 mask aligner	Lithography	Oxide 2, positive	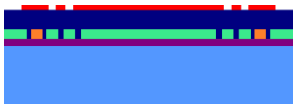
23	PlasmaTherm II, Right chamber	RIE Oxide Etch	Remove 2.5 µm LTO	
24	Photoresist Acid Hood H14	Piranha Clean	Remove resist	

Table 3.1: Processing steps for tensile

25	HDMS/Hood L10/MA 6 mask aligner	Lithography	Dimples, positive	
26	Photoresist Acid Hood H14	BOE Wet Etch	750 nm Hemispheres	
27	Photoresist Acid Hood H14	Piranha Clean	Remove resist	
28	Doped Acid Hood C16	Piranha Clean and HF dip		
29	LPCVD Amorphous - MRL	Deposit 1 µm Amorphous Si	Run twice	
30	Solvent Hood J23	Spin-on 200 nm of P509	Spin-on PSG layer	
31	Anneal (Doped) - MRL	Drive-in dopant anneal	Anneal Poly-Si	
32	Photoresist Acid Hood H14	BOE etch of PSG		
33	Repeat steps 28 – 32 three times		8 µm doped Poly-Si	
34	Doped Acid Hood C16	Piranha Clean and HF dip		
35	LPCVD Nitride - MRL	Deposit 600 nm of silicon nitride		

Table 3.1: Processing steps for tensile

36	HDMS/Hood L10/MA 6 mask aligner	Lithography	Nitride 2, Positive	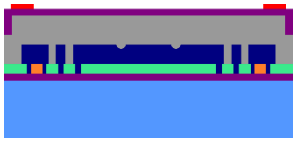
37	PlasmaTherm II, Left chamber	High Poly selectivity Nitride etch	Remove 600 nm Si-Nitride	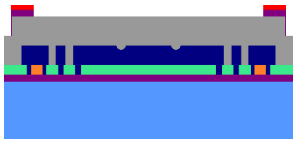
38	Photoresist Acid Hood H14	Piranha Clean	Remove resist	
39	HDMS/Hood L10/MA 6 mask aligner	Lithography – Liftoff pattern	Gold 1, positive 1 µm LOR5A	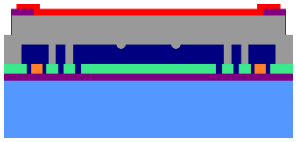
40	CHA #1	E-beam Metal Deposition	10 nm Cr/300 nm Au	
41	Solvent Hood J23	Remover PG Liftoff		
42	Solvent Hood J23	Acetone, Methanol, IPA	Solvent Clean	
43	HDMS/Hood L10/MA 6 mask aligner	Lithography	Poly 2, positive (View at sensor tips)	
44	PlasmaTherm II, Left chamber	High Poly selectivity Nitride etch	Remove remaining Si-Nitride	

Table 3.1: Processing steps for tensile

45	PlasmaTherm DSE	DRIE	Remove 8 µm Poly-Si	
46	Photoresist Hood J23	Protective Layer	Photoresist protective layer	
47	Dicing Saw ACT	Dice wafer	Individual tester chips	
48	Metal Acid Hood G15	Nano-Strip Clean	Remove both photoresist layers	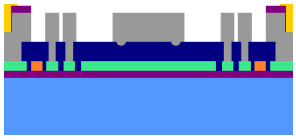
49	Metal Acid Hood G15	BOE:DI Wet Etch	Release Poly 2	
50	Metal Solvent Hood G11	Acetone and IPA Baths	Device Clean	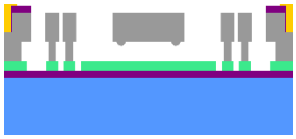
51	March Asher	Ash	Remove solvent residue	

Table 3.1: Processing steps for tensile tester fabrication

3.2 Packaging

A custom package was designed for the tensile tester due to the size, application, and desired thermal behavior. The designed tensile tester chip size is 5.5 x 12.5 mm, which limits the commercially available packages. The total package height must be ≤ 2.5 mm to integrate with the Nanoscribe GT laser system. Finally, the package must have a heat

spreader for connection to an external thermal management system implemented to keep the chip close to room temperature.

Commercially available packages large enough for the tensile tester chips size are dual-inline package (DIP), pin-grid arrays (PGA), and leadless chip carrier (LCC). DIP packaging offers a very close match to the chip size, but the limited number of bond pads would require wire bonding over the tensile tester. This could potentially block the laser during printing or collapse onto the device during drying. PGA packages offer numerous wire bonding configurations with a base of 64 pads on packages large enough for the chip. The height of the PGA, and DIP, exceed the inlet slot of the Nanoscribe due to the pins.

LCC packages meet the chip size, bond configuration, and desired low profile; however, most commercially available LCC packages are alumina. The hardness of alumina rules out machining a hole for a heat spreader. While plastic LCC are available, they are traditionally dummy packages for testing and require custom removal of the capping layer to access the bond pads. With no commercially options available, a custom printed circuit board was designed.

3.2.1 Custom PCB

The custom circuit board (PCB) for the tensile tester is shown in Figure 3.1. This option easily tackles the size of the chip and thickness of the package. The length and width of the PCB were set to 31.75 mm^2 (1.25 in^2) to fit in a custom fabricated Nanoscribe holder at Lawrence Livermore National Laboratory (LLNL). The maximum board thickness was limited to 1.6 mm for a total height of 2.1 mm including the MEMS chip.

The challenge for the PCB was determining the method of connection from the board to the actuator and sensing electronics. The connector needed to be secure with low noise and parasitic capacitance during test, and either be low profile or easy to disconnect.

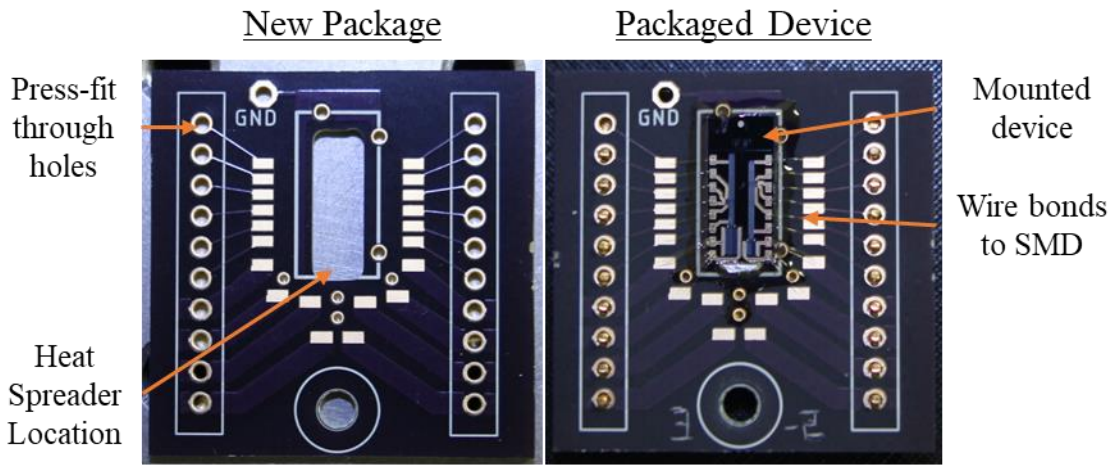

Figure 3.1: Custom PCB package on the left with a packaged device on the right.

An ideal case would be the side contacts similar to the LCC, but those are not available at most commercial PCB manufacturers. The main options with ease of disconnect in consideration are gold plated fingers and through-hole.

Gold fingers have the advantage of being patterned onto the package and a simple connect/disconnect method. However, gold fingers require a large amount of space and complex routing scheme for the available connector slots. Through-hole connections are easy to use, do not require a large amount of space, and have varying pitches. However, repeated applying and wicking solder would increase the probability of damaging the tensile tester chips.

The breakthrough for selecting a connector is press-fit male-male pin headers with the same parasitic capacitance as gold plated fingers. With press-fit pin headers, the need for solder is removed, and the connectors are moved closer to the edge. The chip is centered between the through-hole connectors, but shifted towards the top to allow for additional wires to probe the displacement shuttle. The surface masked designed (SMD) pads are placed symmetrically around the sensors with an easy pitch of 2 mm to limit variations in

wire bond length. Three positioning pins, two on the long side and one on the opposite short side of the chip, are added for chip alignment.

A through-hole of 4 mm by 10 mm is placed under the chip to house the heat spreader (see Figure 3.1). The hole width is limited by the cut path around the alignment pins and the requirement to completely cover the hole with the chip. The long side also has a pin, but the it extends pass the chip on the opposite end until reaching the bond pads to maximize area. A M3 hole is placed near the bottom of the PCB to fix it in place during wire bonding and to connect to the external heat sink. The procedure of mounting and securing the chip onto the package, see Figure 3.1, are presented in Appendix B.

Chapter 4 – Calibration and Material Testing

4.1 Introduction

Structures fabricated using two-photon polymerization need to be characterized at the submicron feature level in order to capture the effects of printing parameters and feature size on material properties since knowing these effects is critical for being able to deterministically design structures and resists for photonics, biology, and high energy physics. Unfortunately, the common characterization techniques currently used only measure structural properties not material properties due to the challenges of handling and manipulating the soft submicron structures. In this chapter, the MEMS tensile tester designed in Chapter 2 is calibrated, and the effects of printing parameters, post processing methods, and feature size on a TPP material are presented in a case study.

The focus of the case study is to determine how printing parameters, such as power and speed, and post processing methods, such as flood UV, effect TPP material properties. These effects are important in biology and photonic applications where researchers are designing complaint structures with calibrated stiffnesses for measuring cell strength [63] and lattices with varying pitch and voxel size to tune the bandgap for photonic crystals [1]. The material property trends presented in this chapter will provide researchers with a guide for selecting writing speed, power, and post cure conditions to achieve a desired mechanical performance and voxel size. The parametric studies presented in this chapter are based off of structural studies presented in Chapter 1 and conducted with the MEMS tensile tester designed in Chapter 2.

4.2 Need and Description

The parametric studies in this section present results on how speed, power, post curing methods, and size impact the material properties of a commercially available resist,

IP-Dip. The material properties and the trends can be applied for the design of complex 3D structures where the properties of each individual printed voxel are critical. Additionally, our understanding of the impact of structural design and features, such as loading mode and nodes, on the mechanical properties of 3D printed TPP structures can be improved by analyzing how the structural trends in the 3D printed structures deviate from the expected trends given the measured material properties.

In addition, one of the challenges for 3D printing is throughput which is limited by writing speed. This is challenging because increasing writing speed has been shown to decrease the mechanical performance of the structures produced. This is because when the speed is changed, the power required to achieve the same voxel size changes due to the change in effective exposure time. However, changing the power also changes the degree-of-conversion which affects the mechanical properties of the line that is written. Therefore, capturing and understanding all of these trends at the material level is needed in order to improve the structural design process.

Another advantage of measuring at the submicron voxel level is quantifying the size effect, which may improve researchers understanding of chemical reactions as the voxel size decreases. Researchers have shown that as degree-of-conversion (DC) improves, whether by decreasing speed or increasing power, so does the strength and modulus of elasticity [19], [23]. DC tracks the reduction in C=C bonding and is related to the crosslinking of the polymer. Post cure methods have shown improved performance from UV or thermal curing is due to increase in DC or crosslinking [23], [25]. Measuring DC at the single voxel level is challenging due to the scale of the part versus the spot size in Raman spectroscopy. By examining the relationship between size, power, and post cure methods, specifically UV, researchers can test the sensitivity of the material properties,

such as *E* or strength, to different changes in the photochemistry. This can result in being able to deterministically design resists to produce strong, thinner voxels.

4.3 CALIBRATION

Calibration of the tensile tester focuses on the thermal actuator displacement calibration curve, tip temperature, load cell stiffness, and the on- and off-chip sensing. The calibration of the differential capacitor displacement sensors is presented in Appendix D. The displacement calibration curve supplies the required voltage to generate a quasi-static strain rate. A value of $2x10^{-4}$ was selected to fall within the $1x10^{-4}$ – $1x10^{-3}$ window set by D638 ASTM standard for plastics [52]. In order to account for variations in geometry across the 100 mm wafer, a displacement calibration curve was generated for each tester. The displacement was measured using digital image correlation (DIC) in NI Vision with a 2.2 nm resolution.

Another important parameter to quantify was the change in temperature at the writing location of the voxel. This was captured using a FLIR 655sc thermal camera and lens to achieve 25 μm/pixel resolution. Accurate calibration of this temperature range is required because polymers have high temperature sensitivity and even small variations will impact the results. Ideally, the test will occur in an isothermal condition, but if temperature changes occur, it is important to bound the values.

In order to accurately measure the force, the load cell stiffness was calibrated using finite element analysis (FEA). Researchers have demonstrated a < 2.5% variance from experimental results using this method [42]. To quantify the overall uncertainty in the stiffness calibration, an additional 3% uncertainty is added on top of the FEA calibration uncertainty to account for potential variations in the material properties of the load cell flexures.

The final stage of calibration is to measure the range and resolution of the load cell and displacement sensor. During calibration, the values of the fabricated capacitors were almost two orders of magnitude greater than the designed values. Consequently, the MS3110 IC capacitive readout was saturated when connected to the sensors. The calibration of the MS3110 IC is presented in Appendix D. One potential way to expand the input capacitance range is with a custom lock-in amplifier circuit, which was presented in Section 2.5.2.2. DIC was used for measuring the load and displacement in the parametric studies presented in this chapter.

4.3.1 Setup

Calibration methods were setup at both LLNL and UT Austin. The displacement calibration curves and MS3110 IC evaluation boards are at LLNL. UT Austin has the FLIR 655sc and custom lock-in amplifier setup in Dr. Cullinan's lab. For the displacement calibration at LLNL, the PCB package was loaded into a custom sensing PCB and positioned under a 100x objective on the Keyence VK-X250 Laser Microscope shown in Figure 4.1. Voltage was applied to the thermal actuator using LabVIEW. LabVIEW sends a voltage to the high current, 1.2 A max, T-Cube LED driver, which supplies a voltage to the thermal actuator. In addition to the max current, the T-Cube LED driver was selected because the maximum current can be set to prevent thermal runaway at high actuator temperatures [64]–[66]. 0.25 V steps were applied to the thermal actuator while Super High resolution (3072 x 2304) images were captured with the CCD color camera on the Keyence microscope. Digital image correlation in NI Vision was used to measure the in-plane and out-of-plane motion with 1.3 nm load and 1.8 nm displacement resolution. The value of

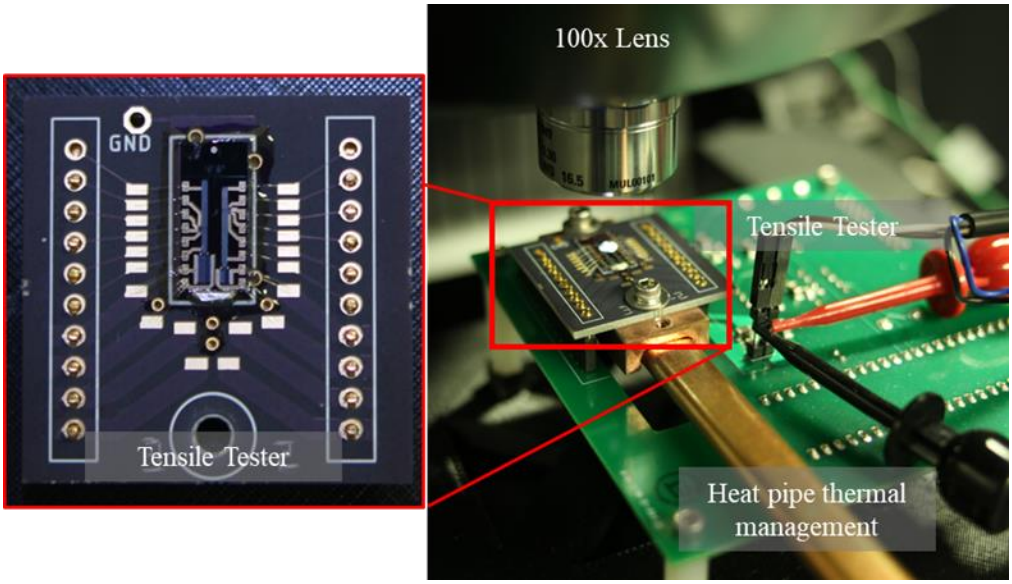

Figure 4.1: DIC calibration setup at LLNL with custom sensing PCB and Keyence VK-X250 Laser Microscope.

the voltage across the thermal actuator is recorded and used in conjunction with thermal imaging at UT Austin for the temperature vs displacement calibration.

Thermal imaging of the thermal actuator and the sensor tips was collected using a FLIR A655sc and a high-resolution lens mounted above the custom sensing circuit, see Figure 4.2. The camera was focused and is able to capture an image of the entire chip shown in the inset of Figure 4.2. Temperature indicators were placed at the center of the thermal actuator, at the displacement sensor tip, and on the silicon nitride layer near the tips for measuring the chip temperature. Images were analyzed to determine temperature at each location and track the change in temperature at the tip as a function of the tip displacement.

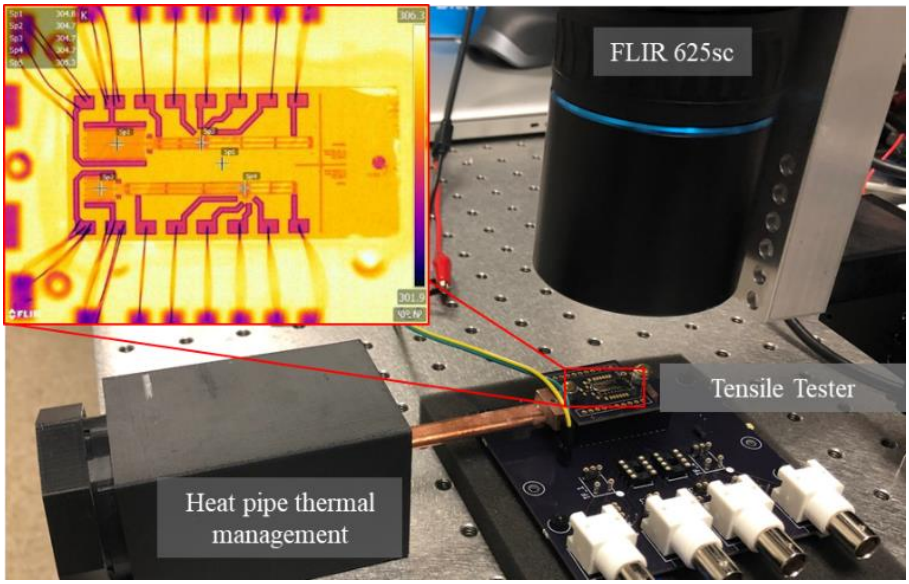

Figure 4.2: Thermal image calibration setup with the FLIR 625sc and an inset of a thermal image with indicators for thermal actuator, tip, and chip temperatures.

The performance of the differential capacitors on both the displacement and force sending stages were investigated with the MS3110 IC at LLNL and the lock-in amplifier circuit at UT Austin. At LLNL, jumper wires are used to connect the PCB package to the MS3110 IC evaluation board shown in Figure 4.3. MS3110 IC custom software was used to tune the supply voltage, the current, and the oscillator frequency to within the specification ranges prior to assigning the gain, cutoff frequency, and the three on-chip capacitor values [67]. The on-chip capacitors were readjusted to set the output voltage once they were connected to the sensors on the chip. Specially designed testers with a polysilicon connection between the two sensors were used during calibration to enable thermal actuation of both sensors without a TPP structure printed onto the tester. The results of this calibration were used to determine the ΔC versus displacement relationship.

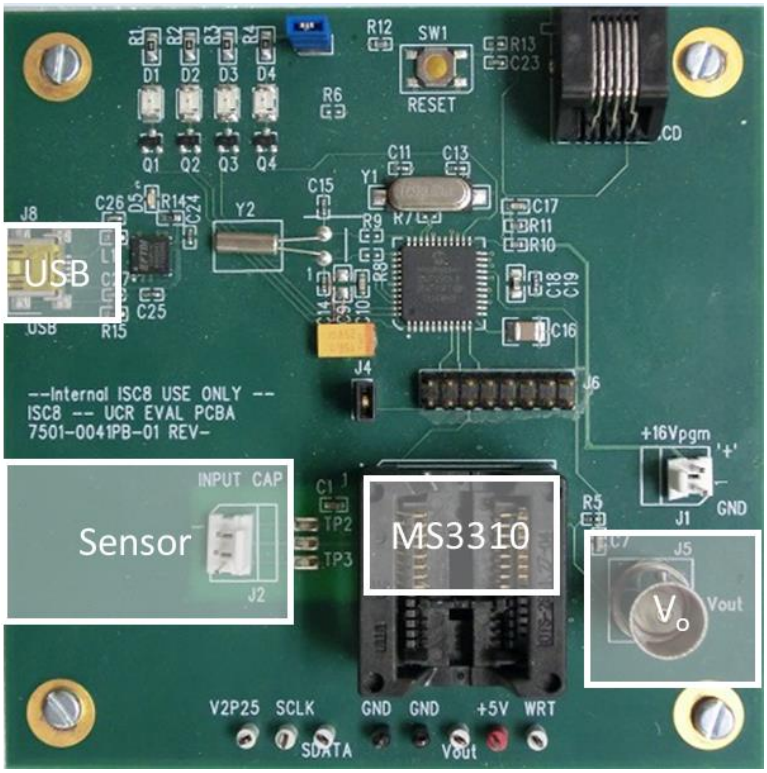

Figure 4.3: MS3110 IC Evaluation Board.

4.3.2 Calibration Procedure

Prior to any testing, the packaged tensile tester was pressed onto the Preci-dip press-fit male-male header pins using a 3D printed jig. Next, the package was mounted to the thermal management heat pipe with a layer of Artic MX-4 thermal paste and secured using two M3 bolts with washers. The unit was connected to the custom sensing PCB and positioned under the microscope lens, as shown in Figure 4.1. LabVIEW was used to provide 0.25 V step input voltages from 0 – 1.75 V to the T-Cube LED driver which then supplies the current to the thermal actuator while the laser microscope captures images of the sensor tips shown in Figure 4.4. The images captured were then analyzed using DIC in NI Vision to measure the in-plane and out-of-plane motion with nm level resolution. The

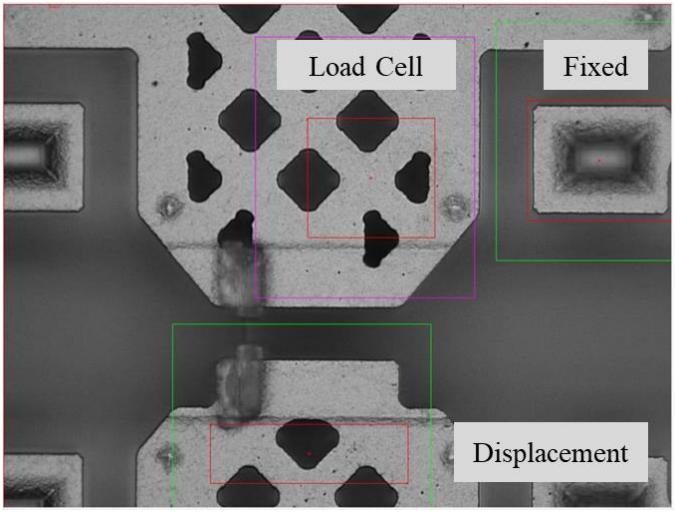

Figure 4.4: Image captured by the Keyence to record load, displacement, and fixed position.

in-plane motion of the displacement shuttle is plotted for each step voltage and a power curve fit is applied to control the voltage with a constant displacement step size. This procedure was repeated for each device prior to testing.

Next the MS3110 IC chips were calibrated using the evaluation board. Without a sensor connected, the supply voltage, current, and oscillator frequency were tuned to 2.25 V ± 0.05 V, 10 mA ± 1 mA, and 100 kHz ± 0.5 kHz, respectively. With a feedback capacitance selected, an on-chip capacitance sweep was used to measure the accuracy of the gain. Those on-chip capacitors, CS1 and CS2, were also used tune the output voltage once the sensor was connected and voltage map was generated to compare to the sensor-less gain. Using the same step input voltages from the displacement calibration, the shuttle was actuated and LabVIEW captured the sensor output voltages from the MS3110 IC board.

At UT Austin, a packaged tester connected heat pipe was loaded into the custom sensing PCB to collect the chip temperature data. With the tester in focus below the FLIR

655sc thermal camera setup, temperature probes were placed at the center of the thermal actuator and on the polysilicon and silicon nitride near the shuttle tips, see Figure 4.2. Thermal actuator voltages matching those recorded during the displacement calibration tests were supplied by voltage supply. The camera was auto-focused after each voltage step and the thermal image was captured. With the variation of materials in the image, calibration images were collected to account for changes in emissivity.

For these calibration images, the packaged tester was placed directly on a hotplate and heated to specified temperatures ranging from 25°C to 100°C with a focus on the 25°C to 50°C range. The temperature was held for 5 minutes to allow the tester and package to reach steady state before the images were captured. This approach results in a more accurate representation of the temperature across the different materials in the tester. These calibration images showed that the placement of the temperature probes on the tester was critical due to the temperature sensitivity of the emissivity of polysilicon [68].

4.3.3 Digital Image Correlation

In this thesis, digital image correlation (DIC) was used to measure the displacement of the load cell and displacement sensor during calibration and material testing. DIC is an image analysis method which locates, measures, and tracks features in a single image or in a sequence of images. Several researchers have used DIC for off-chip sensing of tensile testers as discussed in Section 1.4.3. In this work, DIC was conducted using NI Vision. The script tracked the fixed base of a flexure bearings and the etch holes patterns on each of the sensor tips as shown in Figure 4.4. By tracking a fixed point in each image, instrument drift in the two in-plane axes is eliminated. Drift in the out-of-plane axis is limited by using the auto-focus feature on the Keyence VK-X250 Laser Microscope.

The accuracy of the DIC is based upon the image resolution, the algorithm, the feature tracking method, and the filtering of the image. The laser microscope uses a 16-bit color CCD camera. The system has four different image resolutions ranging from 1024 x 768 up to 3072 x 2304. The two 3072 x 2304 capture modes, Super High and 21.6 million pixel, were investigated in this work. The Super High mode with the 100x lens has a 45 nm/pixel resolution and requires approximately 7 seconds to capture an image. For the 21.6-million-pixel mode, the same Super High image is captured 3 times with minor offsets in the CCD which improves the image resolution to 15 nm/pixel but increase the capture time by an additional 5 seconds/image. However, since DIC algorithms can achieve sub-pixel resolution through a series of integration, the faster Super High mode was chosen for this work.

4.3.3.1 Image Processing

DIC uses image processing algorithms to improve the image quality and analyze the image for feature tracking. In NI Vision, the first step in imaging processing is converting the color image into greyscale. A greyscale image is achieved by applying a filter based on color, hue, saturation, luminance, value, or intensity plane. Once in greyscale, smoothing and transformation algorithms modify the intensity of features across the image to refine edge locations and improve bright-to-dark transition regions. Additional techniques can be used to filter out isolated spots surrounded by regions of the opposite intensity (i.e. dark spot in a bright region).

For image analysis, NI Vision has three different algorithms available: low discrepancy sampling, grayscale value pyramid, and gradient pyramid. The gradient pyramid was selected because it uses filtered edge pixels as tracking features, and it is less sensitive to intensity changes than the grayscale value pyramid approach. This method

requires the largest computational time, but it is outweighed by the improvement in resolution.

4.3.3.2 Feature Tracking

For feature tracking, unique patterns on the moving shuttle surface are needed. The triangle and diamond shaped etch holes added to the device layer to improve the wet release process act as the unique patterns in this study. The rapid transition from the high intensity polysilicon surface to the low intensity hole produces highly repeated reference points. The exact patterns, shown in Figure 4.4, were selected to produce the highest load cell resolution. Additionally, the polysilicon grains for some testers can produce resolvable shifts in intensity which can be captured by the gradient method.

4.3.3.3 Results

For the remaining calibration and material testing section, the DIC script completed the following steps to record the location, lengths, and angles of the displacement shuttle, load cell shuttle, and fixed support on the load shuttle. First, a green plane filter converted the Super High resolution color images into greyscale. A 5 x 5 kernel Gaussian filter smoothed the image to reduce noise due to slight variations in lighting and focal plane. A square transformation followed by a Dilate grayscale morph were used to improve the contrast and brightness of each pixel with respect to their neighboring pixels. Regions on the displacement shuttle, load cell shuttle, and fixed support were tracked using Match Pattern and analyzed using the gradient pyramid algorithm. An example of the initial image is presented next to a process image in Figure 4.5.

To measure the accuracy of the DIC script, a series of images were captured over a 20 minutes period to measure the variance in length and angle measurements. This study

captured both the accuracy of the DIC script, as well as, demonstrated the removal of any drift in the Keyence stage. The resulting uncertainties for the vertical, or in-plane, axis are ±1.8 nm, ±1.3 nm, and ±2.2 nm for the displacement stage position, the load stage position, and the sample elongation, respectively. Across the same set of images, the match patterns drifted 0.95 µm laterally, out-of-plane, and 2.3 µm in-plane. The in- and out-of-plane accuracies are summarized in Table 4.1.

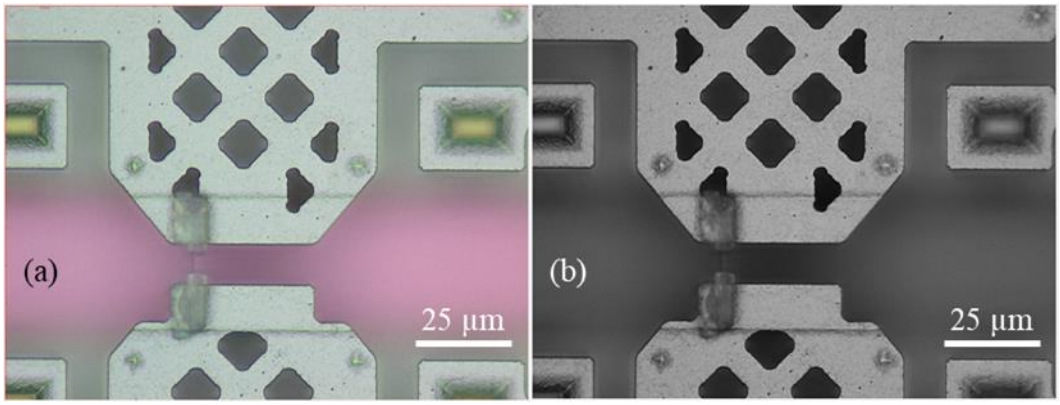

Figure 4.5: A Super High resolution image (a) before any processing and (b) after the smoothing, filtering, and morphing presented above.

	In-plane (Y-axis) (nm)	Out-of-plane (X axis) (nm)	Theta (µrad)
Load	1.25	2.22	27.4
Displacement	1.77	1.83	13.7
Elongation	2.2	1.17	23.7

Table 4.1: Summary of DIC accuracy.

4.4 CALIBRATION RESULTS

4.4.1 Thermal Actuator

The displacement versus thermal actuator voltage and driver voltage versus displacement calibration curves for three devices are presented in Figure 4.6. Devices calibrated in this section come from the same device wafer. Displacement versus thermal actuator voltage demonstrates a non-linear behavior and is fitted with a power curve. When compared to the electrothermomechanical FEA, exponent is within 12.5% of the simulated curve fit. The variation is likely due to the additional losses to the silicon chip through the conduction of heat through the air surrounding the chip. The power curve fit for the driver voltage with respect to shuttle displacement was used in the LabVIEW code to maintain the quasi-static strain rate throughout the test. Deviation from the power curve may occur near the maximum displacement because of transients in the thermal management system. The average values of the scalar and exponent are 1.18 ± 0.023 V/μm and 0.432 ± 0.004 respectively. The uncertainty values result from variations in doping and beam dimensions during the fabrication process.

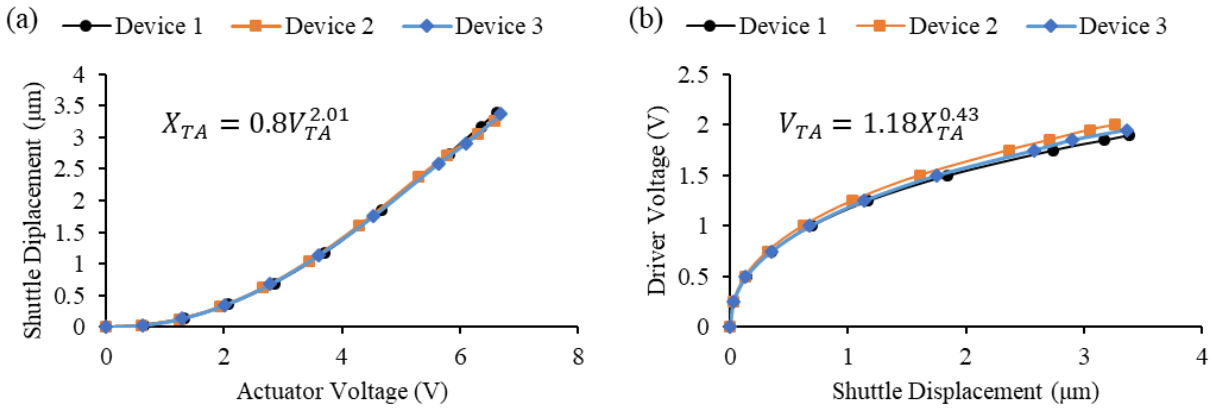

Figure 4.6: (a) Displacement shuttle displacement versus thermal actuator voltage and (b) LED driver voltage vs. shuttle displacement for three devices.

Using the thermal camera setup at UT Austin, the tip temperature at the step actuator voltages for a poly-connected calibration device were measured. To accurately calibrate the temperatures on the chip where a range of emissivity values are present, thermal images were captured using a hot plate to control the temperature from room temperature up to 100°C with a fixed emissivity of 0.95. The temperatures of the hotplate, thermal actuator beams, displacement shuttle, and chip are shown in Table 4.2. The linear curve fit for the chip temperature in Kelvin, $T_{chip} = 1.413 \cdot T_{hotplate} - 122.87$, is used to quantify a maximum ΔT at the shuttle tip.

The results from three cycles of the thermal actuator are shown in Figure 4.7. The errors bars represent variation due to camera calibration range (low or low and high) and time between placing the condenser on the heat pipe and applying the first voltage. The low calibration of the FLIR 625sc is 233 – 420 K, and the high calibration range is 323 – 923 K. Switching from low to high is required to capture the thermal actuator temperatures, but after the first cycle, it was clear the shuttle tip and the chip were not going to exceed the low calibration maximum value. The ΔT_{tip} = 4.81 °C was captured with the same conditions as the material testing. While the value is almost double the value reported from

Hotplate (°C)	Thermal Actuator (°C)	Displacement Shuttle (°C)	Chip (°C)
30	28.6	28.6	29.4
35	31.7	31.7	32.3
40	35.4	35.3	35.7
45	39.3	38.9	39.3
50	42.2	41.7	42.2
75	60.2	60.1	59.8
100	77.8	78.2	77.8

Table 4.2: Hotplate calibration for actuator, displacement shuttle, and chip.

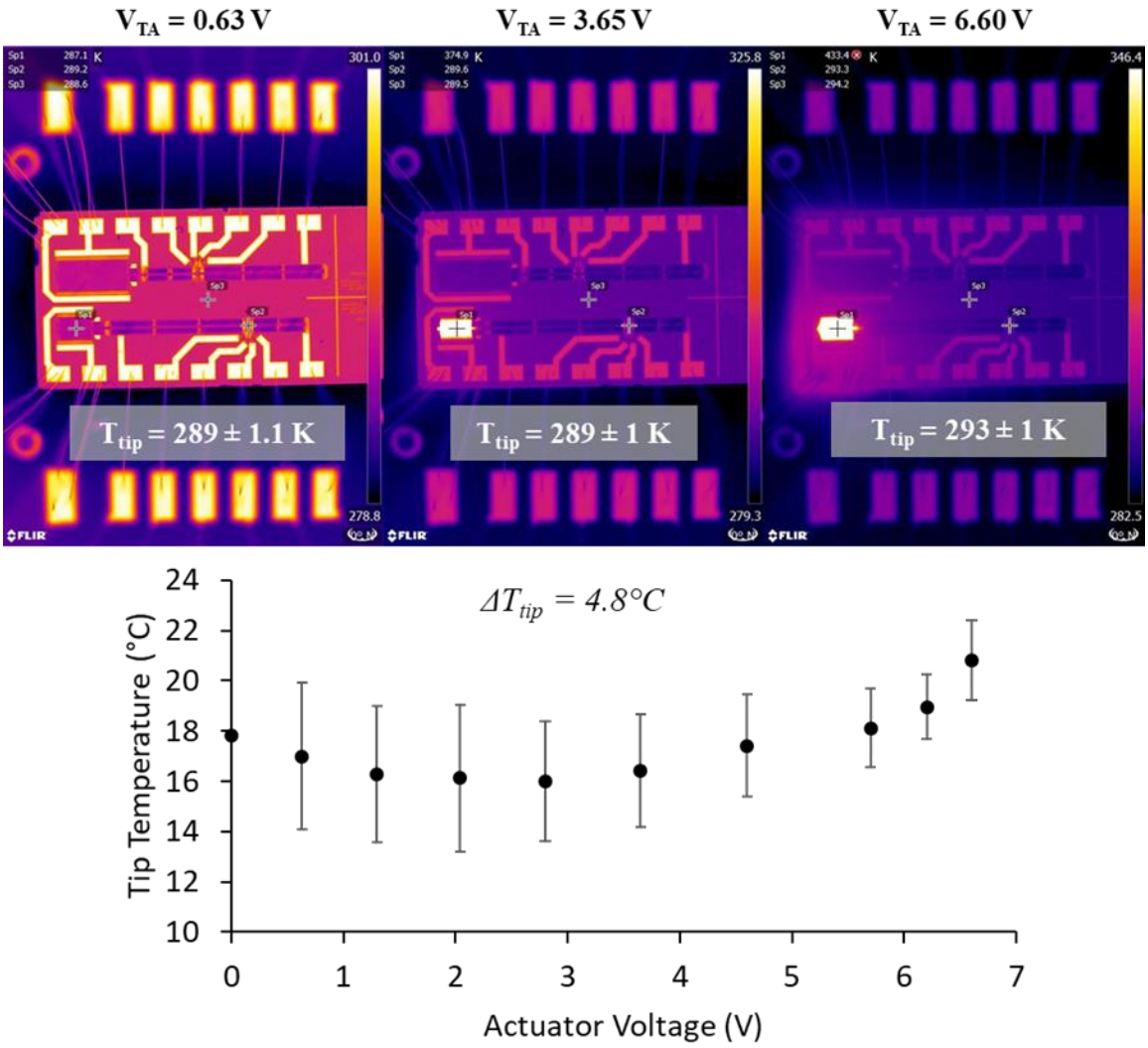

Figure 4.7: Thermal images captured at 0.63 V, 3.65 V, and 6.60 V with the tip temperature plotted across the full thermal actuator voltage range.

FEA, the maximum temperature is less than 24°C which meets the <35°C design requirement for the operation of the chip.

4.4.2 Load Cell Stiffness

The load cell stiffness was calibrated using a simple static finite element analysis (FEA) simulation with a 150 μN load in SolidWorks. While an experimental method is preferred, the FEA models have shown accuracy to within ± 2.5% when compared to experimental data [41]. An additional 3% was added to the uncertainty calculation to account for ± 5 GPa uncertainty in the elastic modulus of the polysilicon which cannot be determined without experimental data. For the FEA model, scanning electron microscopy (SEM) images of the flexure bearing cross-section were captured. An example of the SEM image and a 2D CAD drawing are shown in Figure 4.8. The undercut of the beams is modelled as a fillet with a depth of 500 nm with a height of 3.5 μm to under approximate the values. A sensitivity study was conducted to determine the impact of ± 100 nm variation in the fillet depth. The results show approximately 2% change per 100 nm with a maximum of 9.5% at 500 nm.

The beam length and width were measured using the laser profile mode and 100x objective on the Keyence VK-X250 Laser Microscope. An example of the scan is shown

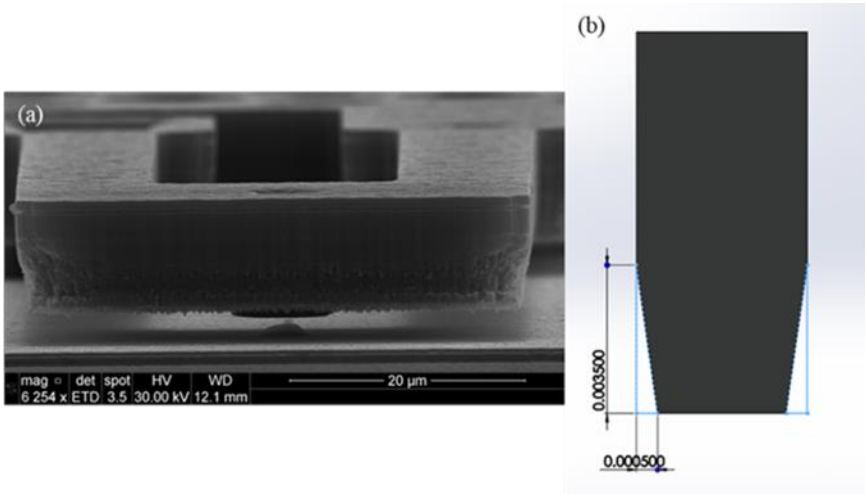

Figure 4.8: SEM and CAD drawing of polysilicon beam undercut.

in Appendix C. The beam length variance is ± 1.07 μm or 0.7% across all devices while the width varied ± 0.54 μm or 11.5% across all devices. With this magnitude of the width variance, the load cell stiffness, K_{load}, was simulated for each device used during tensile testing. The FEA results with a ± 5.5% variance are presented in Figure 4.9 with respect to location on device wafer #3. The estimated K_{load} ranges from 64 – 165 N/m with a designed value of 150 N/m. These variations are actually beneficial due to the large variation in voxel stiffnesses, K_s, observed during testing for different printing conditions.

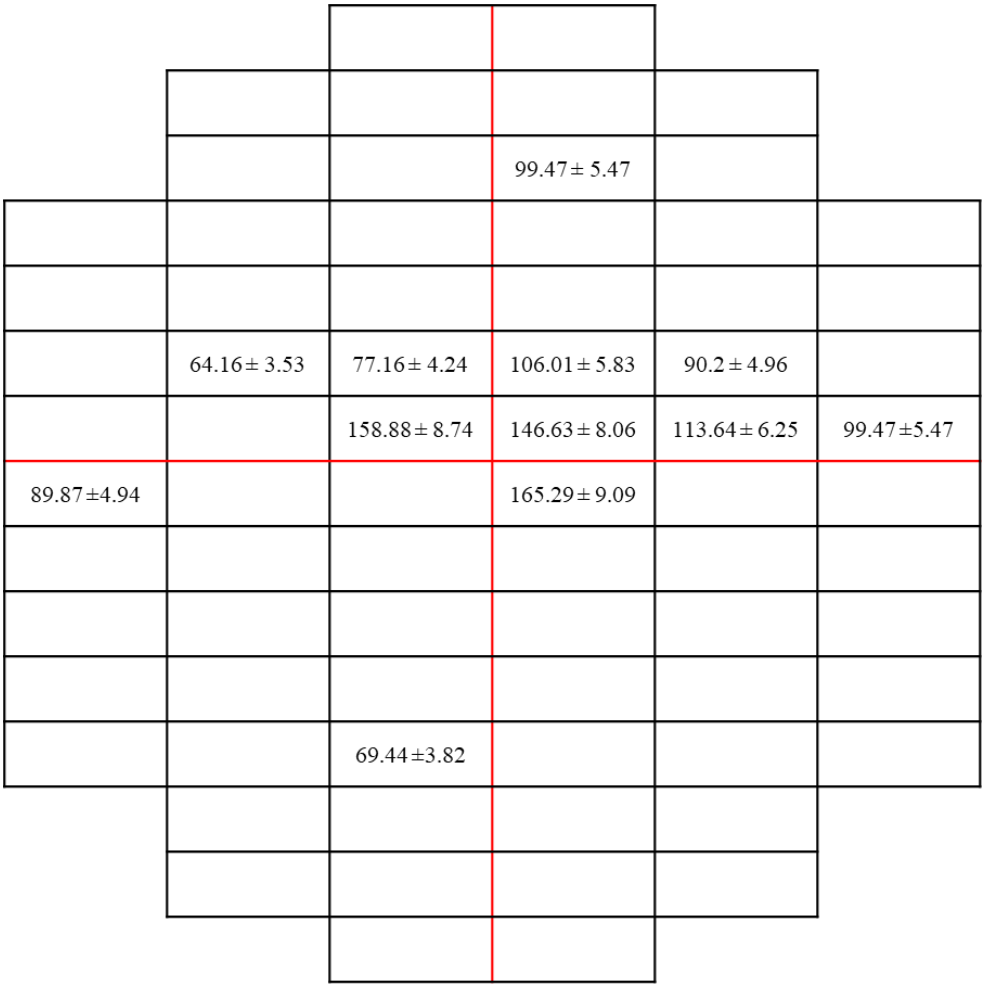

Figure 4.9: Variations of K_{load} across device wafer #3. The red lines represent the central axes of the 100 mm wafer.

4.4.3 Range

The maximum displacement range was measured by a voltage drop across the thermal actuator at high displacements. This drop is due to contact between the moving shuttle fingers and the fixed fingers of the capacitor. The unloaded range of the displacement shuttle is < 3.3 μm. The maximum range for the load sensor was measured with the poly-connected testers for calibrating the load sensor. With that design, the range for the displacement and load sensors were 1.76 μm, which was dependent on the fabricated gap between the capacitive fingers.

The average load sensor stiffness approximated by FEA is 105 ± 33 N/m. Therefore, the average maximum force is 189 ± 59 μN. Table 4.3 summarizes the range of the load cell and displacement stages and the minimum, maximum, and average values for load sensor stiffness.

4.4.4 Resolution

The resolution of each sensor was set based on the accuracy of the DIC script in the drift study, and the variance in K_{load} was accounted for in the load cell resolution. The drift study produced accuracies of ±1.3 nm for the load cell and ±1.8 nm for the displacement sensor. Using the load sensor stiffness values, the average load resolution is 132 ± 7.3 nN and a lowest recorded resolution was 80.5 ± 7.3 nN. The resolution for the displacement and load sensors is presented in Table 4.3.

	K_{load}	Force Range @ 1.76 µm	Force Resolution	Displacement Range	Displacement Resolution
	(N/m)	(µN)	(nN)	(µm)	(nm)
Designed	150	265	30	3.3	0.25
Average	105 ± 33	186 ± 59	132 ± 7.3	3.44 ± 0.14	1.8
Minimum	**64.2 ± 5.8**	113 ± 6.2	80.5 ± 4.4	3.16 ± 0.088	1.8
Maximum	**165 ± 15**	**291 ± 16**	207 ± 11	3.63 ± 0.088	1.8

Table 4.3: Displacement and load range and resolution.

4.5 WRITING PROCESS

The writing process on the MEMS tensile tester was illustrated in Figure 2.1. A small drop of resist is placed onto a packaged MEMS tensile tester, and it is loaded into the Nanoscribe GT Laser system. A 63x microscope objective is brought into contact with the resist, and the focal plane is aligned at tester tips. A galvanometer scans the femtosecond laser to print the support pads and tensile specimen (see Figure 4.10). Once the print is complete, the package is removed from the Nanoscribe and is placed into a series of solvent baths, PGMEA, IPA, and Ethyl Acetate, to remove unpolymerized resist and clean the surround surfaces. The tester is dried in air and connected to the testing setup presented in Section 4.3.1.

For testing the printed structure, voltage is applied to the thermal actuator and the displacement and load on the specimen are captured for analysis using digital image correlation. This data is used to generate engineering stress-engineering strain curves

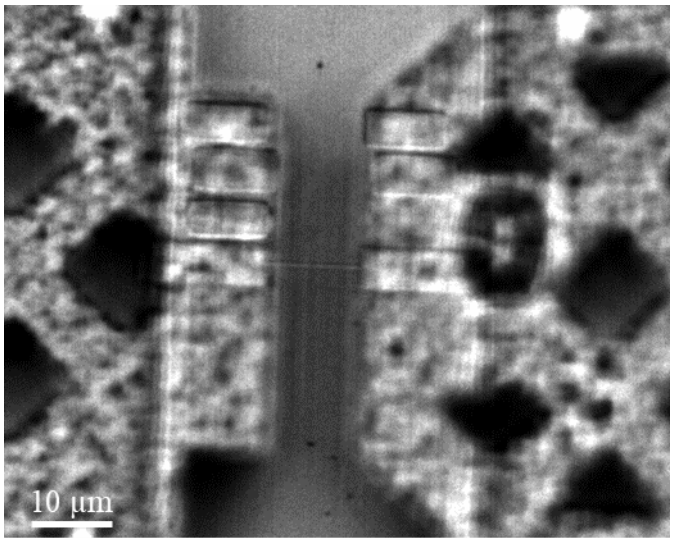

Figure 4.10: Image of the voxel part on the MEMS tensile tester tips while still in the TPP resist.

making it possible to quantified elastic modulus, yield stress, toughness, fracture stress, and elongation at break (for some conditions). For samples that are UV post cured, this post curing step is preformed between the IPA and Ethyl Acetate rinsing steps.

4.5.1 Challenges

The main challenges faced during the printing process were stiction, residue, and debris. The design process for the MEMS tensile tester focused of limiting failure due to stiction; however, mask design and errors in the fabrication process reduced the yield. On the mask design, the 8 μm tall electrodes run to within 25 μm of the suspended features. The placement of these features incidentally pooled the liquid solvent near pivotal points on the shuttle during the drying process and increased the probability of stiction. Additionally, the device wafer used for testing was over etched during the formation of the dimples. A cross-section SEM in Figure 4.11.a shows the fabricated dimples with an

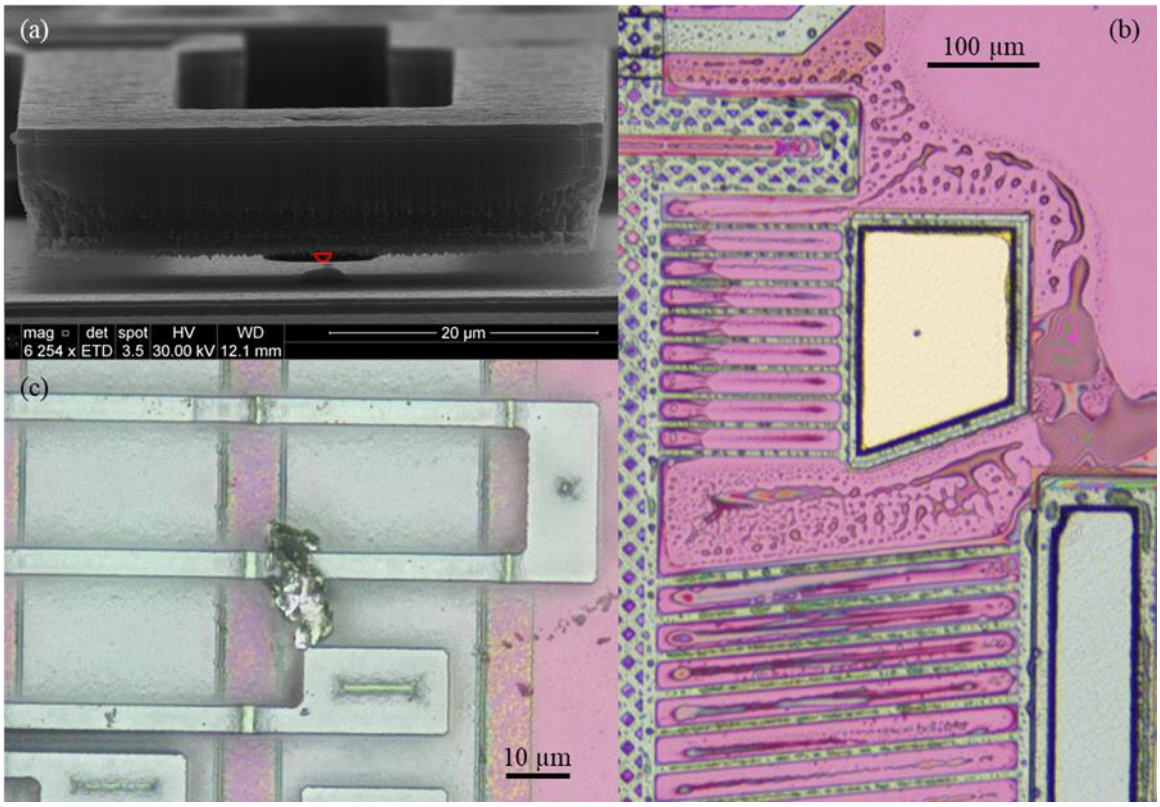

Figure 4.11: (a) SEM image of dimple with an overlay of the desired shape, (b) device failure due to thermal paste residue, and (c) examples of silicon and polymer debris.

overlay of the desired dimples. This increase in surface contact area reduces the safety factor from over 6 to 1 for the load cell and displacement shuttles.

The impact of both of these challenges were reduced by reducing the resist volume, adding Ethyl Acetate to the solvent baths, and changing the package orientation during drying. When initially placing the resist onto the tester, a large volume relative to the device was used. With the increased dimple size, the mass of the resist was enough to induce surface-to-surface adhesion between the shuttle and the substrate below. By switching to a smaller volume, the resist was placed next to the tester and capillary forces moved the resist

onto the shuttles. Ethyl acetate was added to increase the volatility of the drying liquid to limit pooling by the electrodes. Additionally, drying the tester vertically with the electrodes at the bottom utilizes the mass of the drying liquid to guide the liquid away from the tester.

Residue present in these tests also produced stiction type failure. The most common source of residue was the thermal paste. If the epoxy seal around the MEMS chip edge was compromised or if residual paste from a calibration tests were present on the package, residue would travel from the edge of the chip, along the electrodes, and under the tester. Figure 4.11.b shows a failed device due to thermal paste residue. Changes in the packaging process and the type of epoxy reduced the probability of failure due to thermal paste residue.

Additional residue came from unpolymerized resist and a residual film from the wet etching process of the tester. The unpolymerized resist was reduced by increasing the time in PGMEA from the standard 20 minutes to 90 minutes. However, depending on the surface conditions of the tester and the number of times the PGMEA had been used, the 90 minutes was always enough time to remove all of the unpolymerized resist. To reduce the residual film from the wet etching process, a second buffered oxide etch (BOE) and deionized water (DI) bath can be added before the final acetone and IPA cleans. In all residue cases, additional solvent baths were able to reduced or removed residue enough to lead to the re-suspension the shuttles.

The final challenge was debris getting deposited onto the devices in between a moving and fixed feature or on the surface of the device blocking the path of a moving feature. Examples of silicon debris are shown in Figure 4.11.c. Unlike the previous two challenges, there is no clear solution. The silicon debris results from handling the chips. After dicing, the edges have a tendency to chip, and only liquid clean methods are available with no guarantee to move the debris away from the tester before stiction forces pin the

debris. The polymer debris is deposited during writing or in the solvent baths. One possible solution would be to filter the resist before every print.

4.6 MATERIAL TESTING

The parametric studies presented in this section are designed to quantify the effect of speed, power, size, and post curing methods on a commercially available TPP resist, IP-Dip. Low and high speeds writings (100 μm/s and 10 mm/s, respectively) are tested to compare performance under low and high throughput conditions. The power is adjusted to maintain a line width of 377 nm at both speeds to remove any possible size effects. A UV post cure with photoinitiators (PI) is compared to the no post cure or Green state prints. The post cure method tests the sensitivity to additional single photon polymerization, which can increase the degree of conversion independent of printing power [23]. A second test is conducted to determine the size effect by increasing the writing power in order to print voxel widths from 194 nm to 444 nm with the voxel height-to-width ratio ranging from 2.1 – 3.2. A third test measures the elasticity of a 300 nm voxel in the green state and with a UV post cure with and without the PI.

For each test, the voxel length is held constant at 10 μm. The solvent baths time are 90 minutes in PGMEA, 40 minutes total in IPA, and 25 minutes in ethyl acetate. During the UV post cures, the IPA bath is separated into a 30-minute bath and a 10-minute bath where a 365 nm UV flood occurs. The tensile test is done approximately 2 hours after drying. During the test, a nominal strain rate of $2x10^{-4}$ is applied up to a thermal actuator displacement of 3.5 μm. Images are captured in the Super High resolution setting with a 100x objective on the Keyence VK-X250 Laser Microscope. Prior to each capture, the auto-focus is run to limit z-drift during the test. The images are analyzed by digital image correlation (DIC) in NI Vision to generate the force-displacement curve, stiffness, stress-

strain curve, elastic modulus, yield strength at 0.2% offset, toughness, elastic and plastic strain, and failure stress and elongation when applicable.

4.6.1 Outline

The outline for the parametric study is presented in this section. Prior to conducting any tensile testing, a qualitative stiction study similar to with work by Zhang [6] was conducted to estimate trends and select the writing conditions for the 377 nm voxels in the speed test and the 194 – 444 nm voxels in the power tests. After the qualitative stiction tests, the details for the speed, power, size, and post cure tensile tests are presented. The final test presented investigates the elasticity of IP-Dip with and without post curing.

The data process methodology is covered next. The images are processed using DIC to track the position of the load cell and displacement shuttles, as well as, a fixed support for the load cell flexure bearings. Force-displacement curves are generated by calculating the change in the positions with respect to the unloaded image captured before the test starts. Engineering stress and engineering strain data is generated using the voxel geometry and the load cell stiffness from the calibration section. Elastic modulus, and stiffness, is calculated by examining the instantaneous slope and a linear regression fit to determine the elastic regime. Yield strength is measured at the intersection of a 2^{nd} order polynomial fit to the stress-strain curve and 0.2% offset of the elastic modulus linear fit. Toughness is numerically integrated between 0% and 20% strain. Elastic and plastic strain are measured when the unloading curve reaches zero stress. The elastic limit is measured by capturing the onset of plastic deformation in the form of buckling in both the unloading and loading curves.

The parametric study section closes by presenting the results, trends, and potential contributing factors to changes in material properties due to post curing and size effects

from the three studies. Material properties are plotted with respect to writing conditions and voxel line width for characterizing trends and capturing critical transitions for examining the voxel behavior. These trends are compared to the structural tests presented in the introduction. Also, the results are used to hypothesize how the resist photochemistry may be tuned to control material properties with respect to voxel size.

4.6.2 Qualitative Stiction Study

A qualitative stiction study was run to narrow the scope of the parametric studies in this case study. Unlike the Shi-Jie Zhang study presented earlier, this study printed voxels between the ends of a 'U' like structure shown in Figure 4.12. This results in a fixed-fixed boundary condition where the capillary forces act on the height of the voxel and deform the beam is toward the bottom of the 'U'. This approach demonstrates a very clear free and pinned condition which can be measured with any optical system. The drawback to this approach is the full elastocapillary number, N_{EC}, include residue stress, σ_R [56]

$$N_{EC} = \frac{128Eg^2b^3}{15\gamma_l \cos\theta_c l^4(1+b/h)}\left[1+\frac{2\sigma_R l^2}{7Eb^2}+\frac{108g^2}{245b^2}\right] \quad 4.1$$

where E is the elastic modulus, g the horizontal gap below the beam, b the voxel width, γ the liquid surface tension, θ_c the liquid contact angle, and h the voxel height. Additionally, this equation does not account for non-linear elastic material.

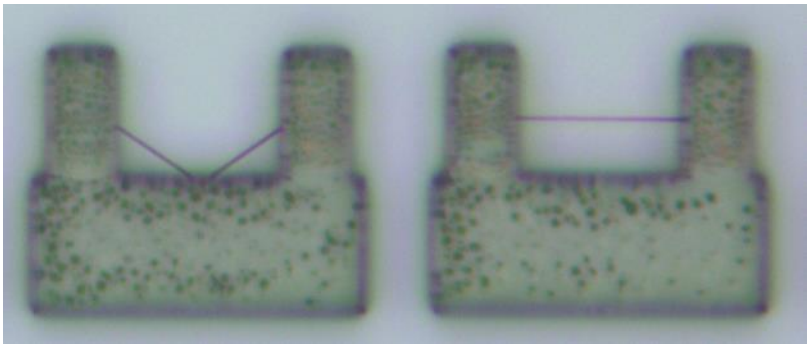

Figure 4.12: Top down image of free (right) and pinned (left) voxel printed between 'U' like structure.

To simplify the approximation of *E* for comparison between printing parameters, the elastocapillary number from Equation 2.1 is solved with a 2.5 scaling factor. [50]

$$E_{EC} \approx \frac{39L_{crit,EC}^{4}[9\gamma_l \cos\theta_c(1 + b/h)]}{2g^2b^3} \quad 4.2$$

Traditionally, stiction test is conducted by changing the critical length, L_{crit}, due to the high sensitivity of the elastic modulus to the critical length. The approach cannot be taken because the Nanoscribe GT galvanometer mode is limited to a print area of 140 x 140 μm^2. Consequently, the g is used as the sensitive parameter in this study. Different voxel lengths are used in this study, but only as a result of large improvements in *E*.

Prior to starting the stiction studies, voxels were printed between the end pads and imaged in the SEM to determine voxel width versus printing power at 100 μm/s and 10 mm/s. The features sizes for 100 μm/s range from 100 - 450 nm and 150 - 450 nm for the 10 mm/s for different print powers. A coarse and fine stiction study was conducted with the following post cure conditions: 1) Green, 2) 10 minutes in IPA with UV only, and 3) 10 minutes in IPA with UV with radical generators. The samples are imaged after drying to determine if the beams are pinned or free and if any deformation in the beams is present. Deformation of the beam would represent loading into the plastic regime. The results from the test are plotted in Figure 4.13.

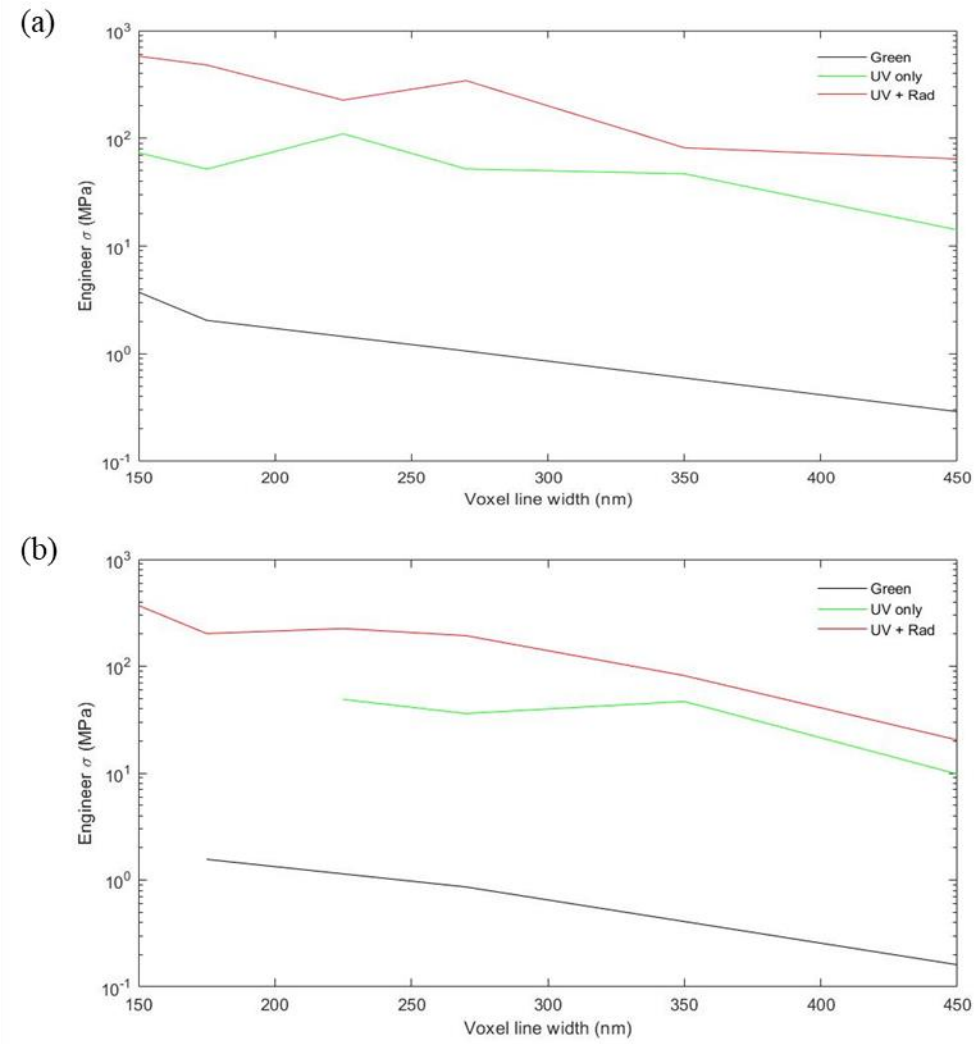

Figure 4.13: Plot of E_{EC} versus voxel width for Green, UV only, and UV with radicals for (a) 100 μm/s and (b) 10 mm/s.

The main takeaways from this test are 1) low speed produces higher modulus parts than high speed, 2) Green and UV with radicals show size effects at both speeds, 3) UV with radicals shows the largest improvement, and 4) this method is able to produce a relative measurement between the different print conditions but does not provide an accurate measurement of the elastic modulus since there is a large disparity between the E_{EC} measured in this test and previously reported values of 0.8 – 2.34 GPa for IP-Dip [4],

[25]. This can be attributed to a) not accounting for σ_R in the approximation and b) the loading and unloading behavior in the non-linear and/or plastic regimes of the material. Plastic deformation and elastic/plastic recovery is easily observable in Figure 4.12. The pinned voxel is 150 nm wide, 30 μm long, and has $g = 8$ μm so it has to stretch almost 30% but the free case at $g = 9\ \mu m$ recovers completely.

However, some valuable trends were determined in this data such as the increase in E_{EC} from 10 mm/s to 100 μm/s writing speeds. The speed shift follows the trend from the structural tests. However, the power trend is opposite with increasing power, and size, reducing E_{EC}. This could be due to the uncertainty in the magnitude of E_{EC} or the presence of a size effects. The size effect is present in E_{EC} for Green and UV with radicals. On both plots in Figure 4.13, UV with radicals clearly produced the largest values of E_{EC}. This also matches the structural trends.

From the qualitative results in Figure 4.13, the speed and post cure test were run at 270 nm. All three post cure conditions should be tested to capture elastic and plastic behavior. These results also support the need for testing changes in power with respect to the voxel size and post cure methods, primarily the UV with radicals.

4.6.3 Tensile Testing

All tensile tests conducted in this work are quasi-static with a $2x10^{-4}$ (2 nm/s) strain rate applied to the 10 μm voxel line. The effects of speed and post cure were studied on 377 nm wide voxel lines. Two speeds were selected: (1) low speed at 100 μm/s to represent research scale writing and (2) high speed at 10 mm/s for high throughput manufacturing. The writing powers are 8 mW (370 ± 9 nm) and 40.44 mW (384 ± 8 nm) respectively to maintain line widths within 16 nm of 377 nm. The green state and UV with PI or radical generators are tested to capture the effect of additional polymerization.

Size effect is studied for the high speed writing and post cure conditions by varying the writing power. The voxel widths (power) were measured using the line edge function in NI Vision of SEM images and are 194 ± 14 nm (15.67 mW), 245 ± 7 nm (20 mW), 306 ± 5 nm (27.21 mW), 377 ± 9 nm (44 mW), and 444 ± 10 nm (50 mW). The power, line width, and line heights are summarized in Table 4.4. The UV with radicals post cure was also selected for further study due to the size effect trends shown in the stiction study and to provide a condition with a smaller range of degree of conversion.

The studies are wrapped up by measuring the elasticity of the 306 ± 5 nm line by loading and unloading the voxel with steadily increasing strains until voxel demonstrates buckling. The voxel is printed at high speed and tested at the green state, UV post cure with radicals, and UV post cure only. Adding the UV only post cure can provide insight into the presence of any remaining photoinitiator in the green state polymer network. Elasticity measurements will also determine if IP-Dip has any non-linear characteristics and how the post curing may affect that behavior.

Speed (mm/s)	*Power* (mW)	*Width* (nm)	*Height* (μm)
0.1	8	370 ± 9	1.09 ± 0.028
10	15.67	194 ± 14	0.4 ± 0.04
10	20	245 ± 7	0.643 ± 0.022
10	27.21	306 ± 5	0.9 ± 0.017
10	40.44	384 ± 8	1.23 ± 0.02
10	50	444 ± 10	1.42 ± 0.02

Table 4.4: Summary of writing speed, power, and voxel dimensions for tensile tests.

4.6.3.1 Part Geometry

For all the tests, the 10 μm long voxel lines are printed between the support pads on the load and displacement shuttle tips. The support pads are used to improve adhesion by transmitting the in-plane shear across a surface area 40 times greater than the voxel cross-section. A CAD model, an optical image, and an SEM image of a printed structure are shown in Figure 4.14. During writing, the voxel has a 1 μm offset from the surface of the tips, which may generate a bending moment. The bending moment at the maximum load (250 μN) only generates sub nanometer out-of-plane deflection of the shuttle tip due to the torsional stiffness of the folded flexure bearing. At this displacement, the uniaxial force is orders of magnitude greater than the bending moment, and the role of the bending stress is considered negligible.

4.6.3.2 Testing Procedure

All of the tests follow the writing procedure discussed in Section 4.2. Two hours after the part has dried, the package is press-fit onto the male-male header pins using the 3D printed press-fit setup. Next, the package is mounted to the heat pipe with a layer of Artic MX-4 thermal paste and secured using two M3 bolts with washers. The unit is then connected to the custom sensing PCB mounted on the Keyence stage, Figure 4.1. The stage is moved to position the tester with the load cell tip offset to the middle to align the autofocus as shown in Figure 4.4. Images are then captured of the tester position and the voxel length.

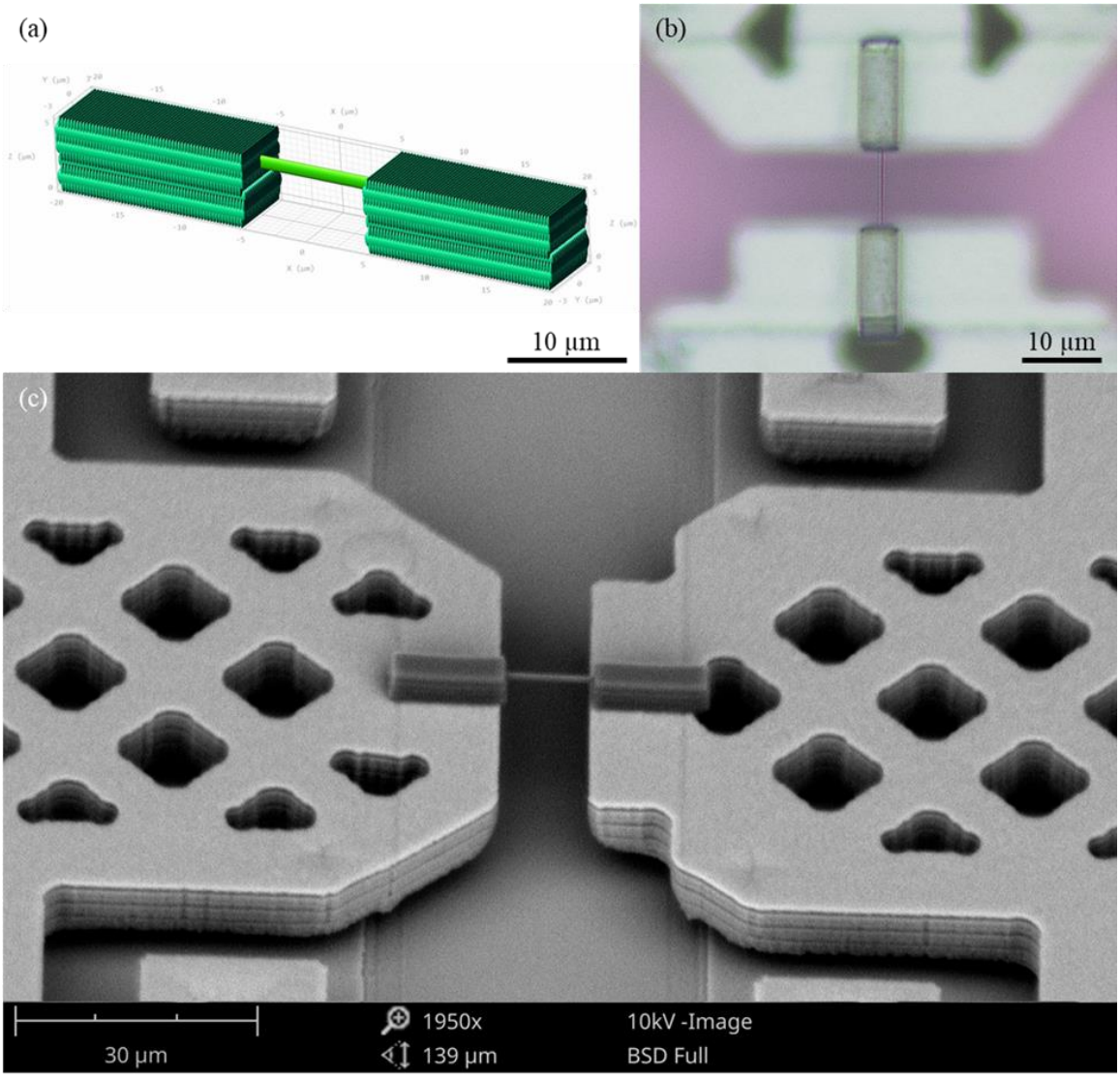

Figure 4.14: (a) CAD model, (b) optical top-down view, and (c) SEM isometric view of a printed tensile part.

Next, ice is loaded into the 3D printed condenser cube with chilled water filling any empty space. After 5 minutes, the condenser is placed onto the heat pipe for 1 minute, taken off for 3 minutes, and put back on for 1 minute before starting the LabVIEW code. This procedure was developed during the calibration phase to cool the chip temperature while preventing condensation. When the LabVIEW code starts it calculates the LED driver

voltage using the displacement calibration curve for that specific device to produce a nominal strain rate of $2x10^{-4}$ for both loading and unload. The LabVIEW code also initiates a Python script to auto-focus and capture images every 20 nm from 0 - 0.7 μm and every 100 nm for 0.7 – 3.3 μm for loading and unloading. At the end of the test the condenser is removed and images of the tester position and voxel profile and length are captured.

For the elasticity tests, the procedure remains the same except for the image capture and maximum displacement. The maximum displacement in each loading cycle is increased by 50 nm until the beam buckles during unloading. Images are captured every 25 nm instead of 20 nm to capture the image at the 50 nm increments. There is approximately a 30 second to 1-minute gap between the end of one cycle and the start of the next to adjust the maximum displacement and to check for buckling. Once buckling has been observed, an additional cycle is run to measure the residual strain in the voxel.

4.6.4 Data Processing Methodology

Data processing starts by analyzing the images captured during the tensile test with digital image correlation (DIC). The NI Vision script returns a .csv file with information on the image name, if the analysis passed or failed, centroid position of the match features from the top left corner, length between each centroid, and angle from a positive x running left to right and positive y running top to bottom. More details about the imaging processing are presented in the Section 4.3.3. There are three centroid lines: the displacement shuttle to the fixed point (*disp*), the load cell to the fixed point (*load*), and the displacement shuttle to the load cell (*elongation*). The length in the loading direction, the y axis in this case, for each position is calculated by multiplying the centroid lengths by the sine of the centroid angle. The displacement for each length is calculated by $\delta_i = y_i - y_0$, where y_0 is the length captured within 5 seconds of the test.

The resolutions are 1.8 nm, 1.3 nm, and 2.2 nm for displacement (*disp)*, load (*load*), and elongation (*e*), respectively. The load cell displacement, δ_{load}, is converted into force by multiplying by that specific tester's stiffness, K_{load}. At this point, force-displacement curve is plotted with δ_e as the voxel displacement.

Next, the engineering stress - strain curve (σ_{eng} - ε_{eng}) is constructed for a uniaxial load. δ_e is divided by the initial voxel length, l_0, measured prior to the beginning of the test to calculate ε_{eng}. Force is divided by the ovoid cross section of the voxel with the nominal width and height in Table 4.4 to calculate the stress. The σ_{eng} - ε_{eng} data is used to calculate the following material properties: elastic modulus, yield strength at 0.2% offset, toughness up to 20% strain, elastic and plastic strain, and fracture strength and elongation at break.

4.6.4.1 Force-Displacement

A force – displacement curve generated for the low speed (370 ± 9 nm line width) voxel in the green state is shown in Figure 4.15.a. The curve shows a polymeric behavior with a relatively high linear slope and large plastic deformation regime. There is some evidence of hardening at the $\delta_e > 2\ \mu m$. This plot is used to calculate the stiffness of the voxel. The error bars quantify the DIC uncertainty and the ± 5.5% uncertainty in K_{load}.

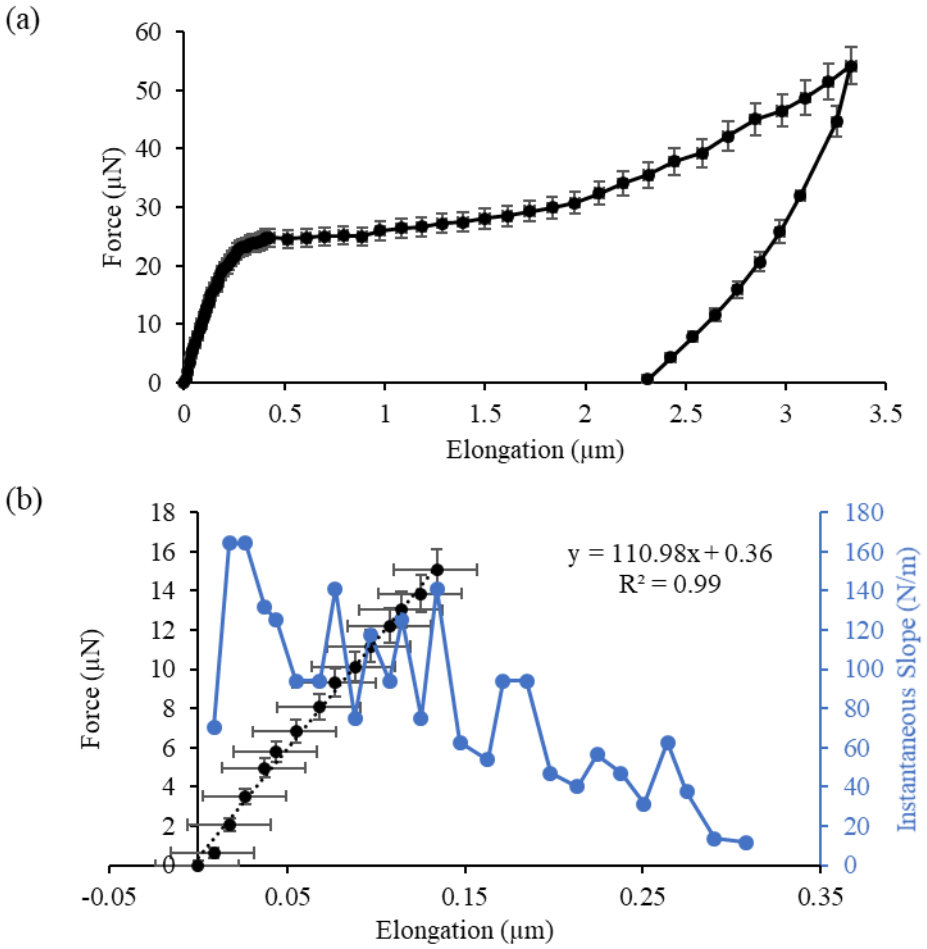

Figure 4.15: (a) Force – displacement curve for 370 ± 9 nm voxel at 100 µm/s Green cure and (b) linear regime of the force – displacement curve and the instantaneous slope.

The stiffness of the voxel, K_s, is calculated from the linear region of the loading cycle. First, the instantaneous slope of the curve is calculated and plotted versus displacement. When the force – displacement curve transitions from linear to non-linear behavior, the instantaneous slope shows a drop off, seen in Figure 4.15.b. Due to noise in the data and low voxel stiffness, the exact cutoff can be challenging to determine. This is accounted for by requiring the coefficient of determination, R^2, of the linear regression fit

to be at least 95%. In Figure 4.15.b, the linear region is terminated at the highest peak prior to the large peak, which is treated as noise, of the instantaneous slope and $K_s = 111\ N/m$.

4.6.4.2 Engineering Stress – Engineering Strain

The engineering stress and engineering strain data are calculated using the equations below with the data generated in the force – displacement section above.

$$\sigma_{eng,i} = \frac{K_{load}\delta_{i,load}}{A_c}, where\ A_c = 0.25\pi h_s b_s \quad 4.3$$

$$\varepsilon_{eng,i} = \frac{\delta_{i,e}}{L_0}\ or = \frac{\delta_{i,disp} - \delta_{i,load}}{L_0} \quad 4.4$$

σ_{eng} is calculated using the uniaxial stress equation with an ovoid cross-sectional area, A_c, voxel height, h_s, and voxel width, b_s. ε_{eng} is calculated by dividing the distance between the displacement shuttle and load cell by the length of the voxel prior to the test, L_0. The distance between can be taken from δ_e or the difference between $\delta_{disp} - \delta_{load}$. The maximum average difference between the two elongation measurements is < 20 pm, which is negligible compared to the resolution of the measurement.

After repeating this process for the entire test, the $\sigma_{eng} - \varepsilon_{eng}$ is generated for the 370 ± 9 nm voxel in the green condition at written at 100 μm/s shown in Figure 4.16.a. The linear region during loading is used to calculate the elastic modulus and generate the slope required to set a 0.2% yield stress. Numerical integration of the area under the stress-strain curve is applied up to 20% ε_{eng} to calculate the toughness. The unloading cycle is used to measure the elastic and plastic strain at $\sigma_{eng} = 0$ and capture the buckling stress and strain. If the voxel fails, the fracture strength and elongation at break are also measured. Error bars account for the DIC uncertainty and variance in K_{load}, voxel length, width and height.

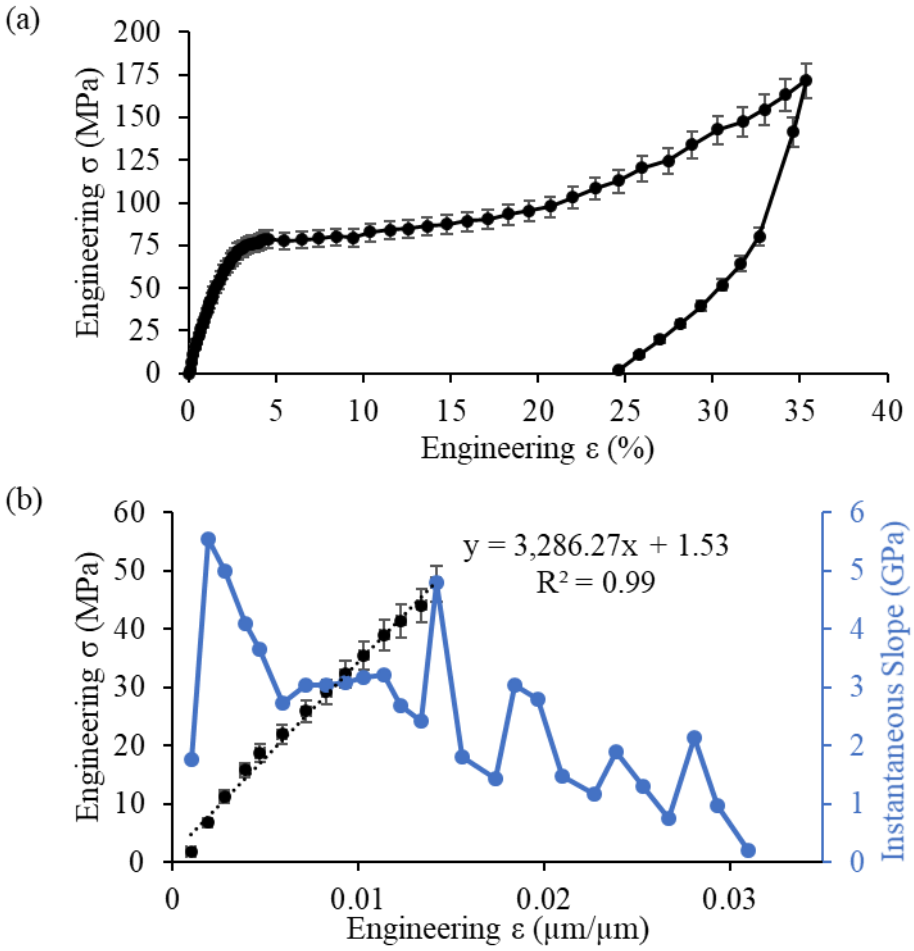

Figure 4.16: (a) $\sigma_{eng} - \varepsilon_{eng}$ curve for 370 ± 9 nm voxel at 100 μm/s with Green cure and (b) linear regime of the $\sigma_{eng} - \varepsilon_{eng}$ curve and the instantaneous slope.

4.6.4.3 Elastic Modulus

The elastic modulus, *E*, is generated using the same procedure as stiffness. First, the instantaneous slope of the $\sigma_{eng} - \varepsilon_{eng}$ curve is calculated and plotted versus ε_{eng}. When the curve transitions from linear to non-linear behavior, the instantaneous slope shows a sharp drop off and saturation, seen in Figure 4.16.b. Additionally, the presence of a toe at the beginning of the curve can be detected and removed. Due to noise in the data, the exact cutoff may be challenging to determine. This is accounted for by requiring the coefficient

of determination, R^2, to be at least 95% for a linear regression. E for the 370 ± 9 nm voxel with no post cure at 100 μm/s is 3.29 GPa and determined using the instantaneous slope in Figure 4.16.b.

4.6.4.4 Yield Strength

Yield strength, $\sigma_{eng,y}$, in this case study is the stress at the intersection between the $\sigma_{eng} - \varepsilon_{eng}$ curve and the 0.2% (0.002 μm/μm) offset line of the elastic modulus linear fit curve, as shown in Figure 4.17. With the E linear fit generated in the previous section, the next step is to generate a 2nd order polynomial fit for the $\sigma_{eng} - \varepsilon_{eng}$ curve near the intersection. The intersection is calculated by subtracting the linear fit from the polynomial and solving the quadratic equation for x, or ε_{eng}, which intercepts the two curve fits. Both curve fits and the intersection for the 100 μm/s green state are shown in Figure 4.17.

4.6.4.5 Toughness

Toughness, U_T, is the ability of a material to absorb energy and plastically deform without fracturing [25]. In this study, $U_{T,20\%}$, is calculated by a numerical integration of $\sigma_{eng} - \varepsilon_{eng}$ curve with a limit of 20% strain. This value is selected in order to make fair comparisons between different writing conditions since all of the samples tested were able to survive up to at least this level of strain. The numerical integration is completed using the *trapz* function in MATLAB, which generates trapezoids between neighboring points to approximate the area under the curve. Figure 4.18 illustrates the area under the loading cycle of the $\sigma_{eng} - \varepsilon_{eng}$ curve integrated by the *trapz* function between 0 to 20% ε_{eng}. The cumulative area under the curve is $U_{eng,T}$.

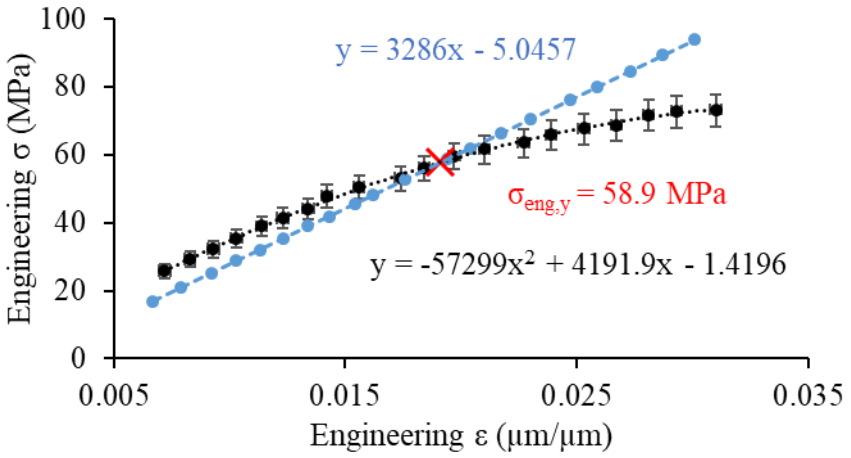

Figure 4.17: $\sigma_{eng} - \varepsilon_{eng}$ curve for 370 ± 9 nm voxel at 100 µm/s with Green cure with a 0.2% ε_{eng} offset linear curve producing the yield strength intersection show in the inset. The red 'X' is the intersection between the two curves.

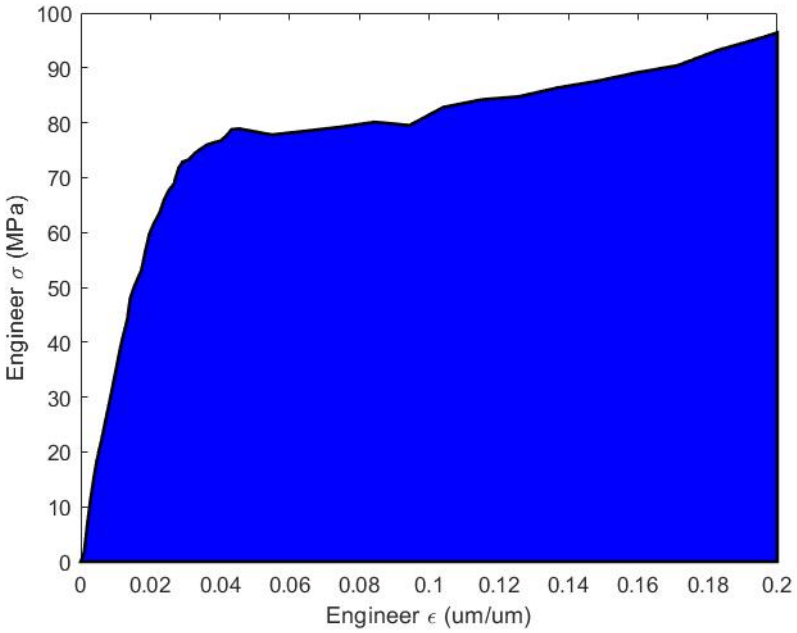

Figure 4.18: $\sigma_{eng} - \varepsilon_{eng}$ curve for 370 ± 9 nm voxel at 100 µm/s with Green cure up to 20% with blue colored trapezoids under the curve to illustrate the toughness.

4.6.4.7 Elastic and Plastic Strain

The unloading cycle of the $\sigma_{eng} - \varepsilon_{eng}$ curve is used to measure the elastic and plastic strain. The elastic strain, $\varepsilon_{eng,elastic}$, is the strain recovered during unloading, while the plastic strain, $\varepsilon_{eng,plastic}$, represents the plastic deformation during the test. A simple relationship with the total strain, $\varepsilon_{eng,total}$, is

$$\varepsilon_{total} = \varepsilon_{elastic} + \varepsilon_{plastic} \quad 4.5$$

$\varepsilon_{eng,elastic}$ can be seen in Figure 4.19 as the strain from the maximum loading strain during the tests to the unloading strain at $\sigma_{eng} = 0\ MPa$. The $\varepsilon_{eng,plastic}$ is illustrated by the remaining strain at $\sigma_{eng} = 0\ MPa$. For this study, $\varepsilon_{eng,elastic}$ is equal to $\varepsilon_{eng,max}$ minus ε_{eng} at $\sigma_{eng} = 0\ MPa$, which makes $\varepsilon_{eng,plastic}$ equal to ε_{eng} at $\sigma_{eng} = 0\ MPa$. A linear interpolation is used to calculate the value of ε_{eng} at $\sigma_{eng} = 0\ MPa$.

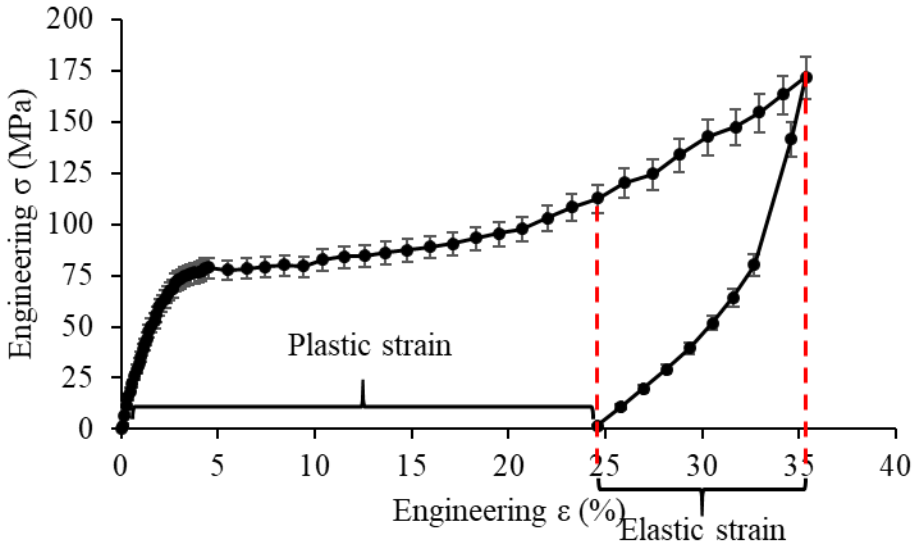

Figure 4.19: $\sigma_{eng} - \varepsilon_{eng}$ curve for 370 ± 9 nm voxel at 100 μm/s with green state with regions indicating elastic, $\varepsilon_{eng,elastic}$, and plastic strain, $\varepsilon_{eng,plastic}$.

4.6.4.8 Fracture Strength and Elongation at Break

For certain writing parameters and post cures, the voxels fracture at very high stresses. The stress and strain values at the failure point are defined as the fracture strength, $\sigma_{eng,f}$, and elongation at break, $\varepsilon_{eng,b}$, respectively.

4.6.4.9 Elastic Limit

Elasticity captures the ability for a material to return to its original shape after being exposed to an external load. This property is represented by both the modulus and the elastic limit, which occurs prior to the onset of permanent deformation. For polymer materials like TPP resists, permanent deformation occurs after the linear regime of the $\sigma_{eng} - \varepsilon_{eng}$ curve. The cyclic loading and unloading in the elasticity tests results can capture three phases of material behavior, see Figure 4.20. First, the $\sigma_{eng} - \varepsilon_{eng}$ curve has a linear loading and unloading cycle, which defines the elastic region and elastic limit. Second, the unloading curve begins to demonstrate hysteresis, but returns to within uncertainty of the starting stress and strain. This is an example of linear viscoelastic behavior. Finally, the material experience plastic deformation, and the increase in voxel length generates a negative stress. However, most of the cycles experience strain recovery prior to the next loading cycle. The test is concluded after the voxel has buckled, which is captured by a near 0 slope.

The elastic modulus, E, for each cycle is calculated using the instantaneous modulus. The average value is collected until the negative stress is not recovered or the voxel buckles as shown in Figure 4.21. The elastic limit measures the strain at the final linear loading-unloading cycle. An additional value of interest is the maximum recoverable strain of the first cycle to buckling, which is referred to as the buckling strain in this work and shown by blue curve in Figure 4.21.

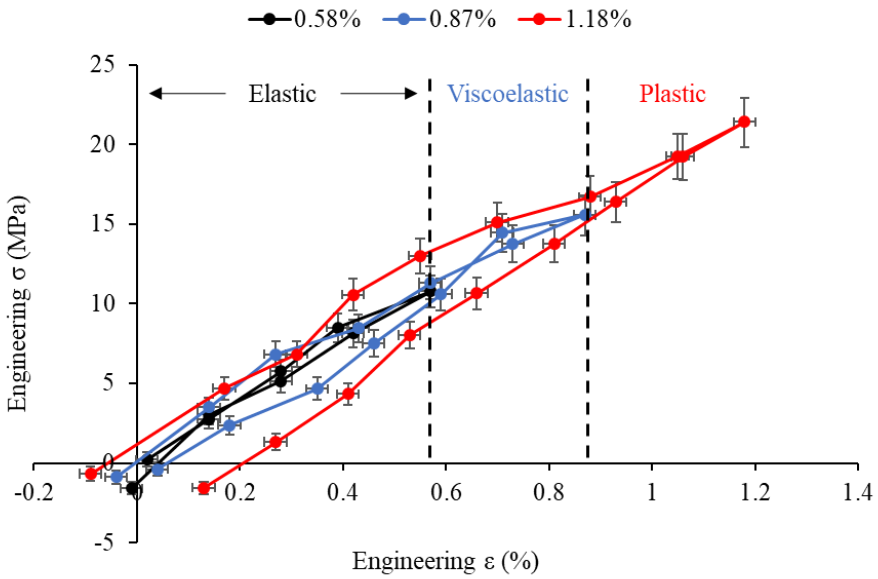

Figure 4.20: $\sigma_{eng} - \varepsilon_{eng}$ curves with elastic, viscoelastic, and plastic loading-unloading cycles up to 0.58%, 0.87% and 1.18% strain respectively. Viscoelastic is represented by hysteresis in the unloading cycle, and plastic deformation is demonstrated by the unloading cycle returning with residual strain.

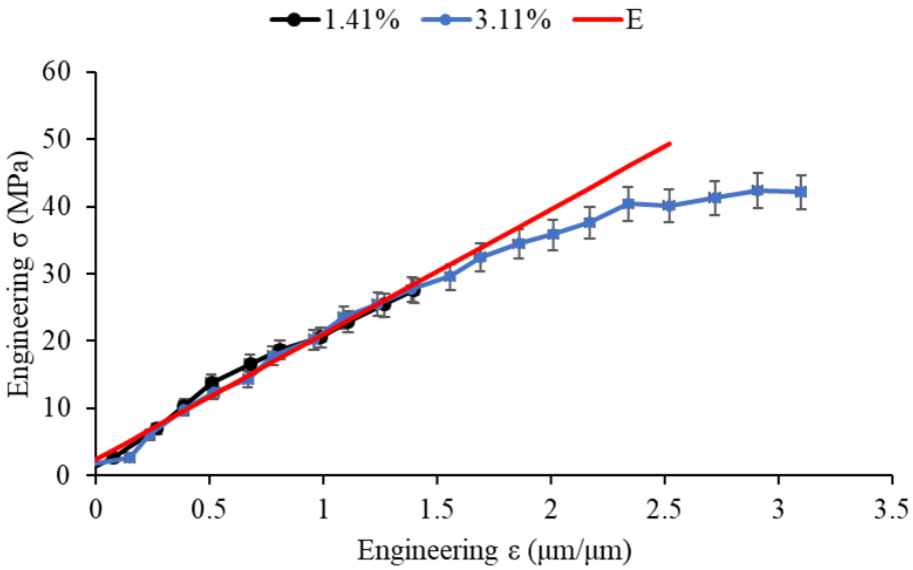

Figure 4.21: Linear and non-linear loading $\sigma_{eng} - \varepsilon_{eng}$ cycles for 384 ± 8 nm voxel at 10 mm/s with green state with the elastic modulus linear fit.

4.7 Results and Discussion

4.7.1 Speed & Post Cure Trends

In the speed study, 377 nm wide voxels were printed at 100 μm/s and 10 mm/s and treated with no cure (the green state) and UV post cure with radical generators provided by a common OPA photoinitiator, DMPA (irgacure 651). Each test was done up to 3.3 – 3.5 μm of displacement which resulted in between 20 – 35% strain on the samples. Using the methodology presented in the previous section, load-displacement and engineering stress-engineering strain curves were generated for all four conditions. It is important to note only one sample per condition was tested with the standard deviation is based off of the MEMS tensile tester calibration and not the variation in material properties. Repetitions of these tests are planned as part of the future work.

The loading cycles for 100 μm/s and 10 mm/s prints reveal three trends:

1. Low speed writing follows the structural trend of having higher modulus and strength compared to high speed.
2. High speed writing can exceed low speed elastic modulus when treated with UV + Rad post cure.
3. Degree of conversion (DC) in the green state may play a role in the yield strength and toughness after UV + Rad post cure.

The first trend is captured by plotting the loading cycle and elastic modulus fit at 100 μm/s and 10 mm/s for each post cure method (Figure 4.22). From the full loading cycle, the 100 μm/s case exceeds the 10 mm/s in the elastic modulus, yield strength, and toughness at 20% strain. E and $\sigma_{eng,y}$ increased by a factor of 3.6 and 3.2 respectively, while $U_{T,20\%}$ increased by 1.9 GPa·μm$^{0.5}$ as shown by the grey hatched area. $E_{LS} = 3.29 \pm 0.004$ *GPa* exceeds the previously reported values of 0.8 – 2.34 GPa for IP-Dip by Kraft *et al* [4], [25].

Consequently, the initial results are comparable to literature at the voxel level. The increase in properties from high speed to low speed matches the structural trends presented by Zhang [6] and Jiang [14].

By testing at voxels with the same cross-sectional area for each writing speed, the improvements are isolated to increases in DC. While both the write velocity and the power effect DC, the difference in velocity between the two writes is two order-of-magnitude which is significantly greater than factor of 2 increase in power required to write the same size features from low to high speed. Therefore, the effects on DC from write power are much smaller than the effects from write speed.

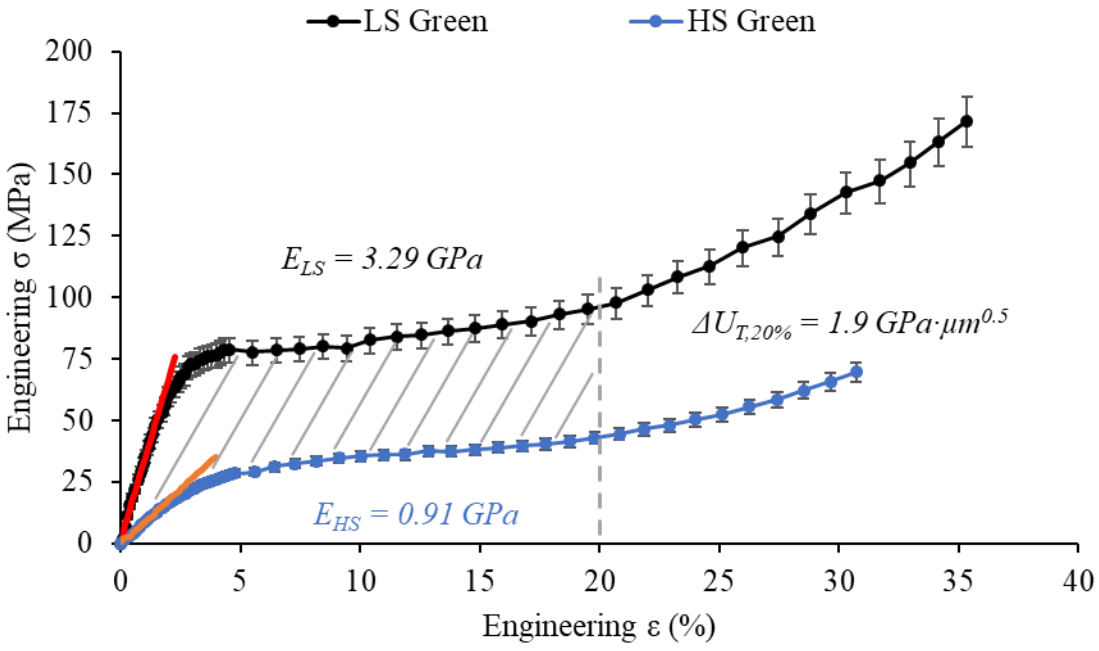

Figure 4.22. Engineering σ - engineering ε curve for 377 ± 16 nm voxel lines printed at 100 μm/s (black) and 10 mm/s (blue). The red and orange lines are the linear fits for the elastic moduli, and the grey hatched area highlights the change in toughness from high to low speed writing.

The most impactful trend comes after conducting the UV + Rad post cure for both write speeds. All four loading curves are plotted in Figure 4.23 with a summary of material properties in Table 4.5. In the plot, the high speed UV + Rad curve is on par with both the low speed no cure and UV + Rad curves. When comparing material performance, the high speed UV + Rad has a greater elastic modulus, yield strength, and toughness than the low speed green state. This result is critical because it shows that the process throughout can be increased without sacrificing performance if a post cure is performed. This result is likely because with the UV + Rad cure, the DC for all writing speeds should be similar. The large increase in the high speed case and hold in the low speed case may be attributed to the initial DC.

The DC in the low speed green state is much higher than the high speed green state and similar to the UV + Rad conditions for both. If this hypothesis is true, any increase in in DC will most likely produce more cross-linking between polymer chains with limited polymer chain growth. This would result in a similar elastic moduli between green and UV + Rad through polymer chain stretching, and the increase in yield strength and toughness due to a larger number of cross-links with stronger covalent bonds as opposed to the van der Waals bonds between neighboring chains [25]. Both of these trends are captured for the low speed UV + Rad results in Table 4.5. The 0.26 GPa dip in elastic modulus from low speed green to UV + Rad most likely due to the repeatability of the writing process and additional tests are required to capture the uncertainty for each writing condition. The high speed UV + Rad results show a large increase in elastic modulus, yield strength, and toughness from the green case. The elastic modulus for the high speed UV + Rad case has the highest elastic modulus of all of the conditions studied at 4.01 ± 0.004 GPa, which surpasses both low speed moduli by ~1 GPa. The larger elastic modulus may suggest the

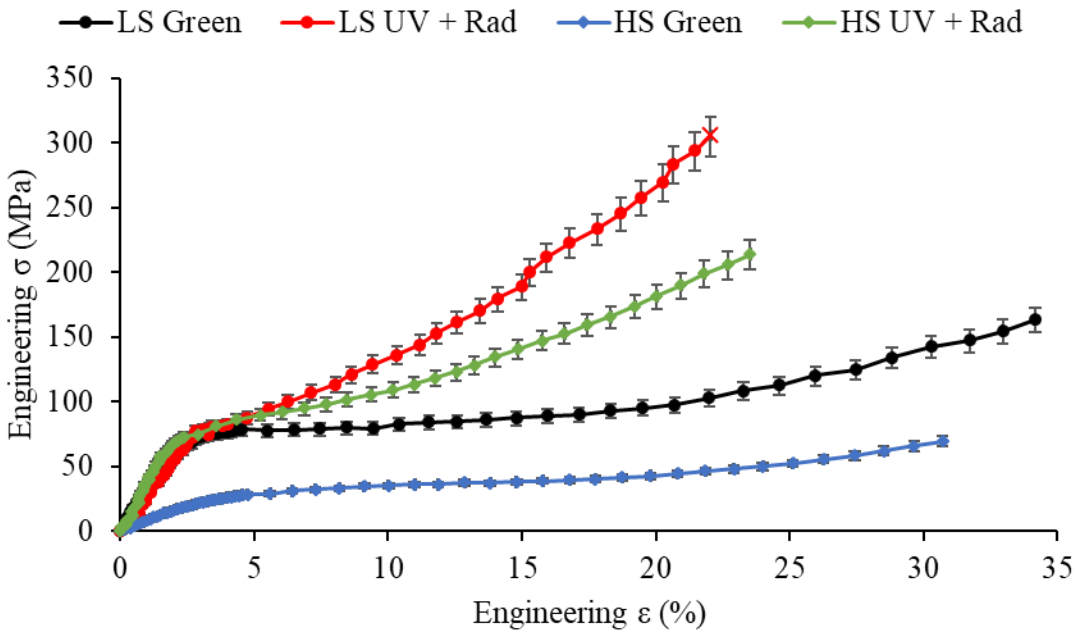

Figure 4.23: Engineering σ - engineering ε curve for 377 ± 16 nm voxel lines printed in the green case (circles) for 100 µm/s (black) and 10 mm/s (blue) and UV with radicals (diamonds) at 100 µm/s (red) and 10 mm/s (green).

Speed (mm/s)	*Power* (mW)	*Width* (nm)	*Cure* -	*E* (GPa)	$\sigma_{eng,y}$ (MPa)	$U_{T\text{-}20\%}$ (GPa·µm$^{0.5}$)	$\varepsilon_{eng,elastic}$ (%)	$\varepsilon_{eng,plastic}$ (%)	$\sigma_{eng,f}$ (MPa)
0.1	8	370 ± 9	Green	3.3 ± 0.004	57.8 ± 4	2.99 ± 0.004	11.0 ± 0.02	24.3 ± 0.02	-
0.1	8	370 ± 9	UV + rad	2.94 ± 0.004	75.6 ± 4	5.15 ± 0.004	(2.2 µm)	-	305 ± 4
10	40.44	384 ± 8	Green	0.91 ± 0.001	18.0 ± 1	1.09 ± 0.001	14.5 ± 0.02	16.2 ± 0.02	-
10	40.44	384 ± 8	UV + rad	4.01 ± 0.004	66.6 ± 4	3.78 ± 0.004	7.05 ± 0.02	16.5 ± 0.02	-

Table 4.5: Summary of the material properties and stiffness values calculated for the speed and post cure test.

initial DC affects the final cross-linked network or the green state voxel aligns any additional polymer chains.

Some evidence to support the hypothesis that there is a similar DC between the low speed green state and the writing conditions with the UV + Rad post cure is the yield strengths of the lines written using these conditions. All of the yield strength values for these conditions fall within 17.8 ± 4 MPa of each other which suggests the transition from stretching to slipping and a similar level of cross-linking. However, the strain hardening after yield for both UV + Rad conditions suggests that the length of the polymer chains created under different writing conditions might be significantly different even if the DC is similar. However, further investigation is still needed to determine the root cause for improvement in material properties, DC, and chain length.

4.7.2 Size Effects

To capture size effects in the TPP resist IP-Dip, voxels were printed at 10 mm/s with power ranging 15.67 – 50 mW to produce line widths ranging 194 – 444 nm, see Table 4.3. The five lines widths selected 194 ± 14 nm (15.67 mW), 245 ± 7 nm (20 mW), 306 ± 5 nm (27.21 mW), 377 ± 9 nm (44 mW), and 444 ± 10 nm (50 mW). The range is limited to this range because < 150 nm features are too low as stiffness to measure with this tensile tester and 50 mW is the maximum writing power of the Nanoscribe GT laser system. Each voxel line width is tested in the green state and after UV post cure with radicals. Using the methodology presented in a previous section, load-displacement and engineering stress-engineering strain curves were generated to capture size effects.

The analysis of the loading cycles for 10 mm/s writing with UV + Rad revealed size effects in elastic modulus, yield strength, toughness, and elastic strain. The trends for E, $\sigma_{eng,y}$, and $U_{T,20\%}$ are plotted in Figure 4.24. The size effect trends directly oppose the current structural trends where larger power, and larger voxel size, leads to increased structural properties, which supports the role of this work in capturing material properties

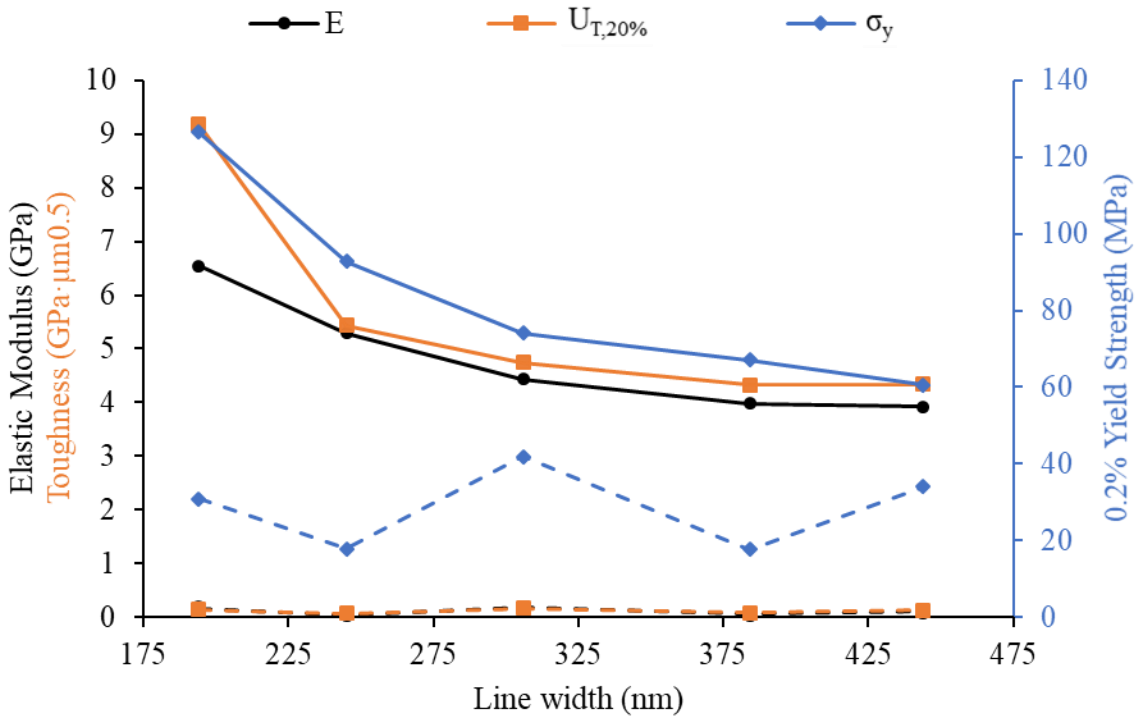

Figure 4.24: Size effect of elastic modulus (black circles) and toughness (orange squares) plotted with the left vertical axis and $\sigma_{eng,y}$ (blue diamonds) for 10 mm/s green state (dashed lines) and UV + Rad post cure (solid line) condition.

independent of structure. With a size effect characterized, the design of 3D structures can incorporate high resolution features to locally increase desired properties or improve the accuracy of the mechanical model of the TPP structures produced with material properties of the structures linked to voxel size.

In further analysis of the size effect curves for the UV + Rad post cure case, all three curves show an increase in slope for voxels smaller than 300 nm. An even more pronounced improvement for $\sigma_{eng,y}$ and $U_{T,20\%}$ is observed below 200 nm. E only increases by a factor of 1.67 across the voxel lengths, but it more than doubled the previous values of 2.34 GPa [4], [25] for IP-Dip at E_{196nm} = 6.54 ± 0.01 GPa. From the material property

summary Table 4.6, $\sigma_{eng,y}$ and $U_{T,20\%}$ improved by factors of 2.08 and 2.12, respectively, as the voxel size decreased from 444 nm to 194 nm. However, the results from the green case show no clear trends in the material properties. This is expected since the degree-of-conversion in the green case is not constant across all writing powers as it is with the fully cured UV + Rad case. Therefore, the size effect is competing with the degree-of-conversion effect in the green case giving no clear size trends as the line width and power is varied. However, in the UV + Rad case, all of the writing powers produce similar levels of DC since most of the conversion is done by the post cure process. Therefore, the size effects can dominate the trends in the UV + Rad case.

There are a few mechanisms which may help to explain and/or contribute to the observed size effects in the UV + Rad post cure case such as alignment of polymer chains in the part caused by the polymer chain length being on the same size scale as the part

P (mW)	*Width* (nm)	*Cure* -	*E* (GPa)	$\sigma_{eng,y}$ (MPa)	$U_{T\text{-}20\%}$ (GPa·μm$^{0.5}$)	$\varepsilon_{eng,elastic}$ (%)	$\varepsilon_{eng,plastic}$ (%)	$\sigma_{eng,f}$ (MPa)	K_s (N/m)
15.67	194	Green	2.35±0.005	30.9±4.9	2.04±0.005	31.8±0.02	0	-	13.4
20	245	Green	0.67±0.002	17.9±1.7	1.10±0.002	19.2±0.02	12.6±0.02	-	8.8
27.21	306	Green	2.47±0.005	41.8±2.4	2.42±0.005	7.5±0.02	28.0±0.02	-	55.4
44	384	Green	0.91±0.001	17.8±1.2	1.24±0.001	13.7±0.02	17.1±0.02	-	31.4
50	444	Green	1.5±0.002	34±1.9	1.80±0.002	12.1±0.02	16.9±0.02	-	75.9
15.67	194	UV+rad	6.54±0.01	126±10	9.18±0.01	(2.728 μm)	-	751±10	39.6
20	245	UV+rad	5.29±0.005	92.7±5.5	5.43±0.005	8.53±0.02	19.5±0.02	-	65.6
27.21	306	UV+rad	4.43±0.003	74±3.4	4.74±0.003	7.28±0.02	19.5±0.02	-	124
44	384	UV+rad	4.0±0.002	67.1±2.2	4.33±0.002	6.5±0.02	17.0±0.02	-	152
50	444	UV+rad	3.92±0.003	60.7±2.5	4.34±0.003	4.87±0.02	15.7±0.02	-	232

Table 4.6. Material properties for green and UV with radicals for 194 ± 14 nm (15.67 mW), 245 ± 7 nm (20 mW), 306 ± 5 nm (27.21 mW), 377 ± 9 nm (44 mW), and 444 ± 10 nm (50 mW) voxel lines.

diameter. S. Ushiba *et al.* [69] captured a change in polymer orientation with respect to voxel size in PMMA lines using polarized Raman microspectroscopy. The results show an increase in alignment with the writing direction from the bulk, a polymer wall, to a suspended voxel ranging from 350 – 400 nm, which suggest the voxel size or writing path may affect the alignment of polymer chains. Further investigation is need to determine if the alignment is size dependent below 500 nm.

With Ushiba demonstrating alignment of polymer chains to the voxel axis, the increase in polymer chain length and cross-linking during UV with radical generators post curing could led to further alignment of the polymer chains. This behavior would be attributed to the spatial confinement of the green state voxel and any initial alignment during writing. Any improvement in alignment would cause the tensile load to go into stretching the polymer chain as opposed to bending it and since the polymer chain it stiffer in bending than stretching this polymer chain alignment would cause the elastic modulus of the material to increase. Improved polymer chain alignment could also result in longer polymer chains forming during the post cure process which would allow the polymer to stretch further before plastic deformation leading to an improvement in the elastic limit and yield strength.

Overall, the mechanism behind the changes in material properties with voxel size can be linked to multiple complex factors which require high resolution characterization methods to capture. Special consideration should be given to future tests to aid in the understanding of how the polymer alignment and chain lengths effect the mechanical properties of the TPP resist structure.

In addition to a size effect trend, the values of E across the voxel width range are greater than the previously recorded values [4], [25]. The UV post cure with radicals produce moduli from 4.0 ± 0.002 GPa at 444 nm to 6.54 ± 0.01 GPa at 194 nm voxel lines.

These trends combined with the results from the speed test show that UV with radicals post curing can be used in high throughput writing to maintain or exceed material performance while increasing throughput of the TPP system. These results also show that power and speed can be used to tune the voxel size at a given throughput without affecting the mechanical performance of the voxel. However, additional testing is still required to increase the accuracy of the results and to further explore the size trends.

4.7.3 Elasticity

The elasticity of IP-Dip was studied by loading and unloading the voxel with steadily increasing thermal actuator displacements until buckling was visible. The lines were written at 10 mm/s with 27.21 mW to produce 306 ± 5 nm line widths. Green state, UV with radicals generators, and UV only post cures were tested. The thermal actuator displacement was increased by 50 nm/cycle steps up to 700 nm and 100 nm/cycle steps after 700 nm until buckling for all tests. Using the methods described in Section 4.5, the elastic modulus, linear elastic limit, and elastic limit were captured.

The elasticity tests captured three phases of material behavior for the TPP resist ID-Dip: 1) an elastic regime, 2) a viscoelastic regime, and 3) a plastic regime. The elastic regime is less than 1% strain for all post cures. The viscoelastic material behavior, which has hysteresis in the unloading cycle but no plastic deformation (see Figure 4.20), has both linear and non-linear behavior. This viscoelastic behavior is observable in the green case but not for the post cured cases where more crosslinking is present and dynamic testing would be required to measure viscoelasticity. However, simply demonstrating viscoelastic and non-linear elastic at the material level expands the applications for researchers. The results for the different post cures, shown in Figure 4.25, may provide additional understanding of the polymer and DC.

Figure 4.25 presents the changes in the final loading cycle before buckling. The two UV post cures increase the elastic modulus, which follows the trends from the previous tests. The elastic modulus increase from UV only suggests unused photoinitiator (PI) is inside the voxel, and the 18% improvement from UV only to UV + Rad are a result of the additional PIs. The elastic modulus values are shown in Figure 4.25. An additional result to consider is the strain prior to buckling, which is increased by 63% for UV + Rad and 20% for UV only compared to the green state. These two results show the impact that adding PI to generate additional radicals during a UV post cure on improving the materials resistance to plastic deformation. The improvement is resistance caused by additional crosslinking of the polymer may also result in the strain hardening captured in the speed and size study for the post cured writes. Additional testing is required to determine the sensitivity of the additional radicals during post cure, but the results from the speed tests and this test suggest it may be dependent on initial DC and possibly size.

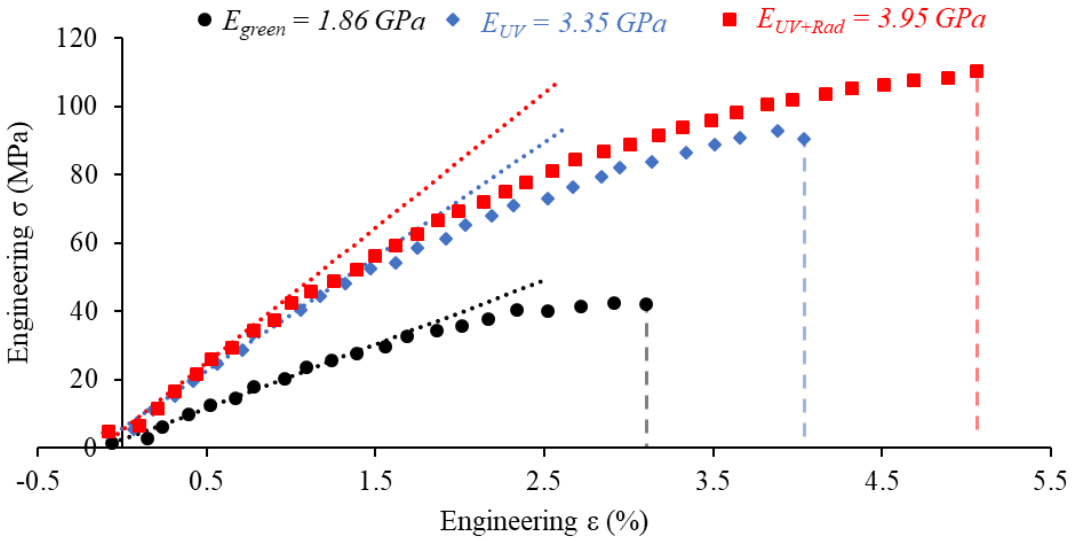

Figure 4.25: Loading $\sigma_{eng} - \varepsilon_{eng}$ curve the green state (black circles), UV only (blue diamonds), and UV + Rad (red squares) at 10 mm/s with 306 ± 5 nm line widths.

After the viscoelastic regime, the voxel plastically deforms and buckles. The unloading σ_{eng} - ε_{eng} curve captures this behavior with a near 0 slope shown in Figure 4.26.a. An image of the buckled voxel is shown in Figure 4.26.b. After buckling, the voxel is exposed to an additional cycle to capture the residual strain in the toe region of the loading curve. Residual strain decreases from 0.34% at the green state down to 0.16% for UV + Rad post cure.

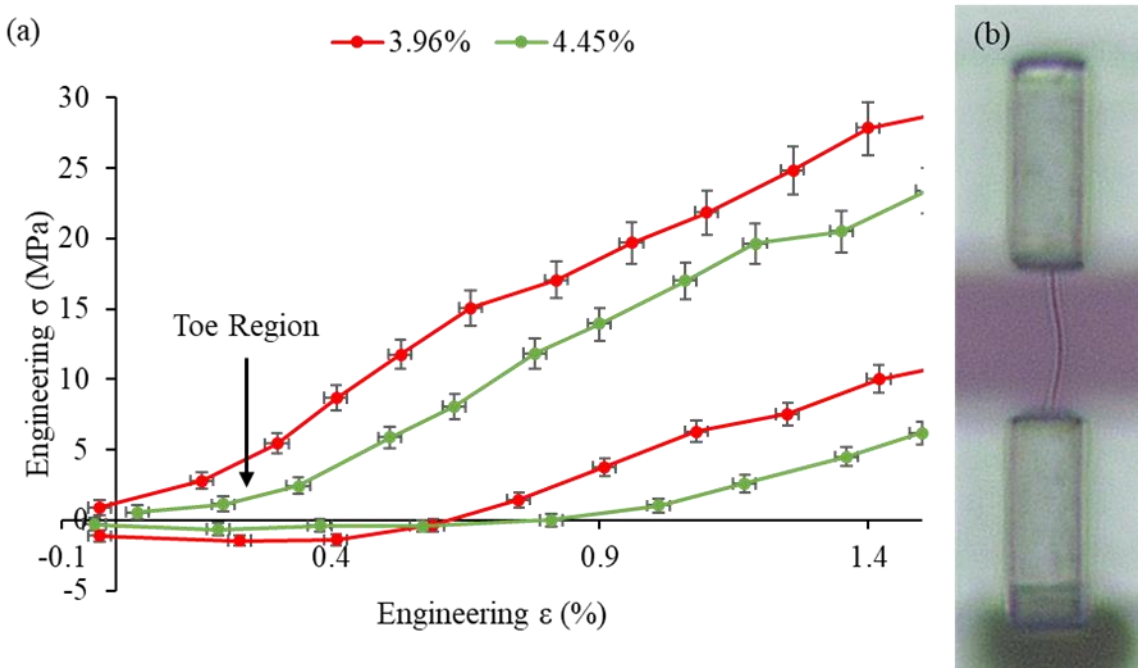

Figure 4.26: (a) Close up on at the beginning and end of the loading (left) and unloading (right) $\sigma_{eng} - \varepsilon_{eng}$ curves for the green state. 3.96% cycle (red) shows ~ 0 slope at the end of the unloading cycle which results in the toe region of 4.45% (green). (b) Buckled voxel beam.

4.8 SUMMARY

The tests presented in this chapter captured the following trends:

1. Low speed writing follows the structural trend of having higher modulus and strength compared to high speed writing.
2. UV with radical generator post cure should be used with high speed writing to achieve high throughput without decreasing material properties.
3. The green state degree-of-conversion (DC) appears to impact the improvements from UV with radical post curing in elastic modulus, yield strength, and toughness.
4. Size effects captured with UV with radicals post curing demonstrate material properties improve with decreasing size instead of increasing power as shown by structural trends.
5. The size effect trend is most prominent below 200 nm.
6. Linear and non-linear viscoelastic behavior was captured for IP-Dip for the green state.
7. The improvement in elastic modulus in the UV only post cure suggests residual photoinitiators are present in the voxel structure.

The effect of UV post curing and voxel size on the mechanical performance of TPP structures are the biggest takeaways from this research. UV post curing with radicals enables a 100x increase in writing speed without losing performance in yield strength and increasing elastic modulus and toughness. The presence of size effects for post cured samples changes the role of writing power to be a method for setting the voxel size instead of needing to increase the power to improve material properties. Voxels below 300 nm showed improvement with the largest improvement occurring at the 194 nm voxel. By using the size effect, an elastic modulus of 6.54 ± 0.01 GPa was achieved for the smallest

voxels tested with the UV+Rad post cure, which is more than twice the previously reported maximum value of 2.34 GPa for IP-Dip [4]. Additionally, the changes from the green state to the UV post cure with radicals state suggest that the initial degree-of-conversion (DC) impacts the level of improvement in elastic modulus and yield strength. These trends could potentially aid researchers in selecting high throughput writing conditions to achieve high strength structures with sub-300 nm voxels and develop custom resists to better understand the post curing process.

Chapter 5 – Conclusion and Future Work

5.1 SUMMARY

As researchers continue to push the resolution and application space for two-photon polymerization (TPP), a better understanding of the link between writing parameters, post cure method, and size on the mechanical properties of TPP resists is needed. With an established size to material property relation, researcher could continue to develop nanolattices with decreasing densities at production level throughputs without sacrificing performance. However, current characterization approaches are limited to structural testing which does not accurately capture size effects.

The purpose of this thesis is to characterize TPP resist material properties by testing single voxel lines. In order to accomplish this goal, a custom microelectromechanical system (MEMS) tensile tester was developed that could be directly integrated with the TPP writing process and completely remove the need for sample handling from the characterization process. The tester is composed of a thermal actuator, a load sensor, and a displacement sensor to capture stress and strain data. Stiction constraints and anti-stiction features were implemented during the tester design to prevent failure during the liquid emersion processes in TPP. The force and displacement are measured by tracking the position of the sensors with digital image correlation (DIC). The average load and displacement resolution are 132 ± 7 nN and 1.8 nm, respectively.

Using the MEMS tensile tester, the effect of writing speed, power, post cure method, and size were characterized. When comparing speed, low speed writing in the no cure, or green condition, out performs high speed writing. However, high speed writing with UV post cure with radical generators exceeds the green low speed in elastic modulus, yield strength, and toughness. The addition of a post cure is critical for ramping TPP up

from write speeds of 100s μm/s currently used in most research processes to the 10s mm/s required for high throughput manufacturing applications. The improvement in material properties between the green and UV + Radicals post cure conditions is due to the increase in degree-of-conversion (DC) of the TPP resist, which is linked to cross-linking within the polymer network. This work purposes that the initial DC in the writing processes contributes to the factor of improvement after post cure, but future investigation is still required to determine the validity of this claim.

To determine the impact of size on the mechanical properties of TPP resists, voxels were written from 194 – 444 nm in width by varying the writing power at 10 mm/s. The results from the voxels treated with the UV post cure with radicals condition demonstrated a clear size effect for elastic modulus, yield strength, and toughness. The elastic modulus increased by a factor of 1.7 and reached 6.54 ± 0.01 GPa at the 194 ± 14 nm voxel, which is more than twice the highest previously reported value for IP-Dip. The impact of size effect trend is particularly significant below 300 nm. The improvement in material properties as a function of size has the potential to change how researcher approach writing parameters and resist chemistries. Instead of sacrificing size for increased power, the parameters can be tuned to achieve both high power and thin voxel sizes to take advantage of both improvements.

The possible mechanisms for the size effects are still not known but could be linked to polymer alignment during writing and post cure process due to the polymer chain lengths approach or exceeding the voxel width. Polymer alignment with the voxel axis may be generated by the writing direction and the voxel polymerization as the size continues to decrease. If polymer alignment is occurring in the green condition, any chain growth during the UV post cure should align as well with the voxel write axis. Additionally, with the presence of a transition size around 300 nm, the polymer chains may be approaching a

critical length compared to the voxel width. Support for this claim stems from the large increase in yield strength and toughness below 300 nm, specifically the 194 ± 14 nm voxel. Further testing is required to determine if polymer alignment is present and to determine the length of the polymer chains in the TPP resists under different curing conditions.

In addition to large strain tensile testing, low strain cyclic testing was conducted to examine the elasticity. During the cyclic testing, the voxels demonstrated linear elastic, linear and non-linear viscoelastic, and plastic behavior in the green condition. However, for the UV only and the UV with radicals post cure conditions, only elastic and plastic behaviors were observed likely do the increased crosslinking of the polymer in the post cured samples. With the material demonstrating linear and non-linear viscoelastic effects, researchers have additional material properties and behaviors to utilize in the design of their structures. Much like the previous tests, post curing increased the linear elastic modulus by a factor of 2.1 for UV with radicals and by 1.8 for UV only. The similar factors of improvement suggest unused radical generating photoinitiator (PI) remain inside the green condition voxel.

From the speed, power, and elasticity results, the main takeaways are the impact of post cure method and size on TPP materials. Post cure methods make high throughput writing possible without losing low speed performance. By comparing the elastic and plastic deformation of green and post cured voxel, insights may be gained on the changes in the polymer network. The observed improvement in material properties for decreasing voxel size opposes the current approach of sacrificing voxel size for higher power. Researchers can now tune writing parameters to the sub-300 nm regime and allow size effects to improvement material properties by using a post cure instead of modulating power to increase the degree-of-conversion in the TPP resist structures.

5.2 MEMS TENSILE TESTER IMPROVEMENTS

5.2.1 Design for DIC Parametric Testing

From the knowledge gained during the TPP writing and testing process in this work, switching to a DIC only tensile tester has several advantages for high quantity parametric testing. First, device characterization and calibration after fabrication is simplified to thermal actuation and load cell stiffness, which can be completed in a few hours. This is ideal decreasing the time required for a single test. Second, the number of testers and yield would be increased by removing the capacitive fingers. With the differential capacitor design, a 100 mm wafer produces 78 devices with testers that are each over 12 mm long, and the capacitive fingers can ruin a tester by trapping debris and/or residue. Without the capacitive sensors, the length would reduce by 2 – 3 times and failure due to debris and residue trapping would greatly decrease. With an increase in viable testers during each fabrication run, material uncertainty testing and boarder parametric studies could be conducted more easily. In addition, multiple load cell stiffnesses could be selected to increase the measurement accuracy across the board voxel stiffness range (8.8 – 232 N/m).

Parametric studies could by conducted on 3D structures with only a few modifications: 1) larger gaps between the load cell and displacement sensor, 2) mN range thermal actuator, and 3) higher stiffness load cell. A 58-beam thermal actuator capable of 25 mN, and a 12.9 kN/m load cell were designed during this work, but no results were reported because the drying solvent pooled at the load sensor capacitor electrodes and pinned the load cell. In a DIC only design, the capacitor electrodes would not be required, and resistance to stiction would improve. Additionally, an updated load cell stiffness should be selected based upon the material properties collected in this work.

5.2.2 Thermal Management

5.2.2.1 Changes in Fabrication

Due to the large area of the thermal actuator (0.7 x 0.84 mm^2), the conduction through air increases the substrate temperature and prevents true isothermal testing. The ideal solution would be to increase the air gap between the thermal actuator and the substrate to reduce the heat transfer from the thermal actuator to the substrate. However, the deep oxide etching tools are not always available. Instead, two different approaches can be taken: 1) additional thermal insulation and 2) reducing the conduction through air by etch features under the thermal actuator beams. The first approach deposits a low temperature oxide (LTO) layer below the silicon nitride layer to increase the thermal resistance between air and the silicon substrate. However, the heat can still conduct in-plane through the nitride layer and raise the temperature of the support structures for the thermal actuator, heat sink beams, and flexure bearings.

The new approach would be to etch trenches or fins below the thermal actuator prior to the nitride deposition, see Figure 5.1. The etch depth of the trench would increase the thermal resistance by a factor equal to the trench depth divided by original air gap for that length of the thermal actuator beam. This will both decrease the chip temperature and lower the required power to the thermal actuator. A new finite element analysis (FEA) model will need to be developed to determine the new shape factor, S, as a function of number of trenches and trench width, depth, and pitch. The width should be constrained to $< 2 \cdot g$ to be filled by the sacrificial oxides layer. If selected properly, at the end of the oxide deposition the surface under the thermal actuator beams will be relatively planar. A schematic of the trenches below the thermal actuator beams is shown in Figure 5.1.

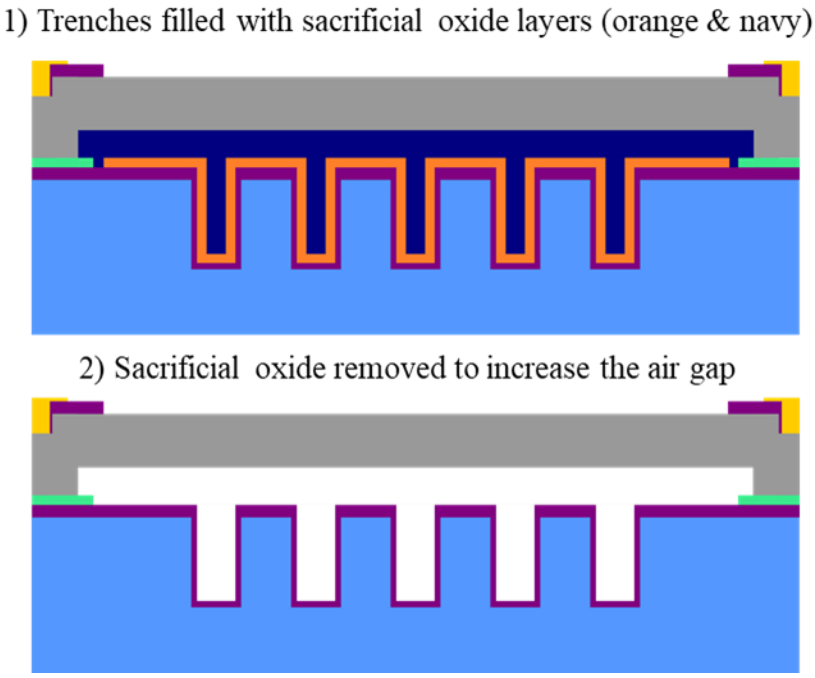

Figure 5.1: Cross-section view of trenches etched below the thermal to increase thermal isolation from the chip. Image (1) demonstrates how the sacrificial oxides (navy and orange) will fill the gaps to produce a relatively planar surface, and (2) shows the suspended polysilicon thermal actuator beam (grey) with increased air gaps.

5.2.2.2 Active Thermal Management

Improvements in the fabrication process should reduce the increase in tip temperature during testing. However, an active thermal management system, such as a Peltier cooler/heater, would provide a dynamic system capable of setting and maintaining the chip temperature. This is advantageous for studying viscoelastic and thermal effects on TPP resists. In order to implement an active system, the PCB package and electrical setup need to be modified to increase the working area below the PCB package. The passive thermal management system was implemented in this work due to the small working area.

5.2.3 Chip Layout

The current chip layout is to dense and does not account for the solvent pooling during drying. The first improvement is to only feature one tensile tester/chip. While only one tensile tester was presented in this work, each chip had two testers, see Figure 4.1. In the new design, the tensile tester can be centered and electrodes placed on both sides. This rearrangement increases the area available for handling, reduces the pooling of solvents during drying, and may reduce parasitic capacitance between electrodes. To further reduce the impact of pooling solvents, the device layer portion of the electrodes can be shortened to increase the gap between the end of the electrode and the suspended features.

5.3 FUTURE TPP TESTING

The speed, power, and elasticity tests generated trends, captured size and strain recovery effects, and material properties for the research community. However, further testing is still required to determine the role of degree-of-conversion (DC) on the material properties, characterize nonlinear effects, and investigate the mechanism for size effects. Investigation into the size effect mechanism will requires additional testing instruments, such as the polar Raman spectroscopy, and MEMS tensile testers with lower load cell stiffnesses to increase the accuracy of measurements for the low stiffness, the green state voxels. However, additional testing to examine DC and viscoelastic properties can be done with the current MEMS tensile testers.

5.3.1 Custom Resists

One approach for investigating DC and voxel size is the addition of radical inhibitors, or quenchers, to IP-Dip to reduce the voxel size at a given power. During the propagation step of two photo polymerization, the radical quencher limits the diffusion of radicals away from the laser focal volume, which causes the polymerization reaction to

only occur near center of the voxel [70]. Prabhakaran *et al.* demonstrated this behavior with TEMPO as the quencher in SCR 500 photoresist. With just 0.2 wt% of TEMPO, the writing threshold power was increased to 150 mW, and the average voxel width was decreased to 122 nm from 189 at 30 mW for the resist without the quencher. The mechanical stability of the voxel is attributed to a higher DC and the reduction of the voxel size [70].

To investigate this effect, a tensile test was conducted on a voxel written at $P = 20$ *mW* with 0.025 wt% of 4-Methoxyphenol, MEHQ, added to IP-Dip. The engineering stress – engineering strain curves comparing IP-Dip and IP-Dip + MEHQ are shown in Figure 5.2. The elastic modulus increased from 0.67 GPa to 1.58 GPa with the addition of MEHQ. Yield strength and toughness also increase. Interestingly, the IP-Dip + MEHQ does not strain harden until after 25% strain. SEM images of the voxel size do not show a substantial change in line width, but that may be attributed to uncertainty in the scale bar. However, even if the voxels are very similar in size, the improvement through the addition of a radical quencher has been replicated.

This test was conducted without a post cure condition. The post cure test still needs to be conducted to determine the impact of a higher initial DC independent of size. Based upon the speed test study in Section 4.7.1, the properties for IP-Dip after UV curing with radicals may be similar or exceed IP-Dip + MEHQ. If the MEHQ still exhibits higher properties, the test should be expanded to higher powers to monitor the factor of improvement compared to initial DC. There is potentially a threshold at which the increased initial DC through radical quenching hinders the improvement of the UV post cure with radicals. If these trends are captured, resist chemistries could increase quencher concentration to achieve a specific voxel size at the initial DC threshold and post cure to further improve the mechanical properties of the TPP resists.

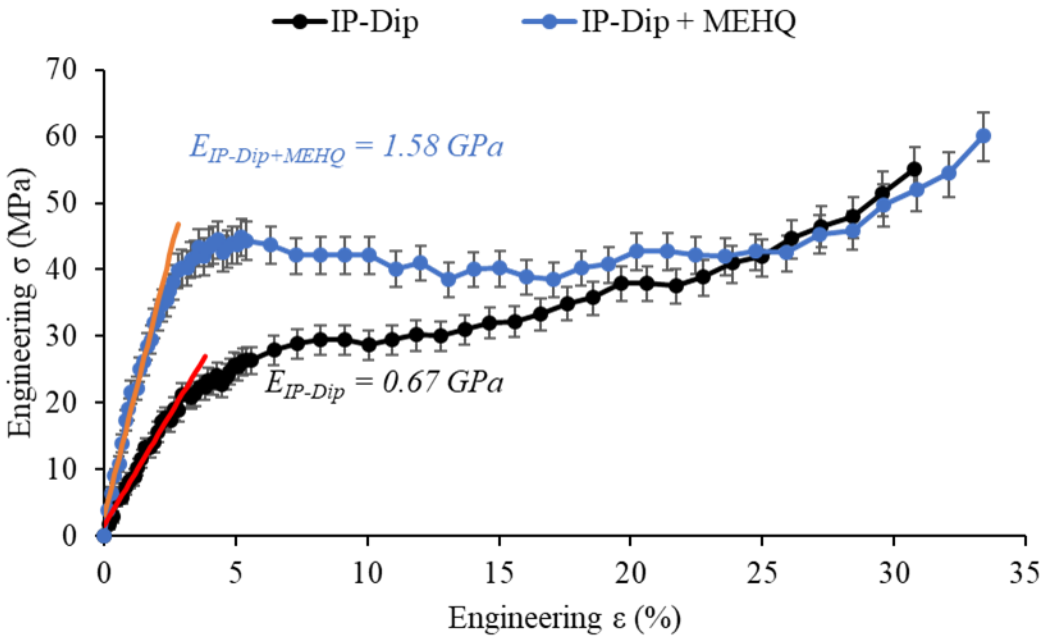

Figure 5.2: Engineering stress – engineering strain curve for IP-Dip (black) and IP-Dip + MEHQ (blue) radical inhibitor. The addition of the inhibitor, or quencher, increases the elastic modulus, yield strength, and toughness for the same writing power (20 mW).

5.3.2 Viscoelastic Properties

The nonlinear elastic regime captured by the elasticity test presents a case for the TPP resists having viscoelastic material properties. One of the prominent methods for measuring viscoelastic properties is dynamic mechanical analysis (DMA) [71]. DMA is a dynamic test that measures a materials response to an oscillating load. Viscoelastic properties, such as damping, complex modulus, complex shear modulus, complex viscosity, and complex compliance, are derived by measuring the phase lag between the stress and strain. Common frequency ranges for polymers range from 0.001 – 10 Hz. In this range, the current DIC setup will not have the accuracy or sampling rate required to make these measurements. A high speed DIC could be designed, or the differential

capacitor sensors on the current MEMS tester with the lock-in amplifier circuit can be used to make the dynamic measurements of the TPP resists. With the sensors and lock-in amplifier, the sensor resolution and lock-in sample rate will determine the phase lag resolution of the system.

With the MEMS tensile tester and lock-in amplifier circuit calibrated, DMA testing can be conducted by varying the oscillation frequency with constant temperature or maintaining the frequency with steadily increasing temperature. These two tests can be used to characterize the thermal transitions of a polymer. An example of an ideal temperature scan is shown in Figure 5.3. These transitions are related to the free volume changes or relaxation times of the polymer, and could aid in understanding the spacing between molecules with respect to size, initial DC, and post cure methods. Further development of the circuit and thermal management system are required to accurately conduct a time or temperature scan on a TPP written voxel; however, the MEMS tensile tester from this work may offer the required resolution and temperature control needed for these measurements.

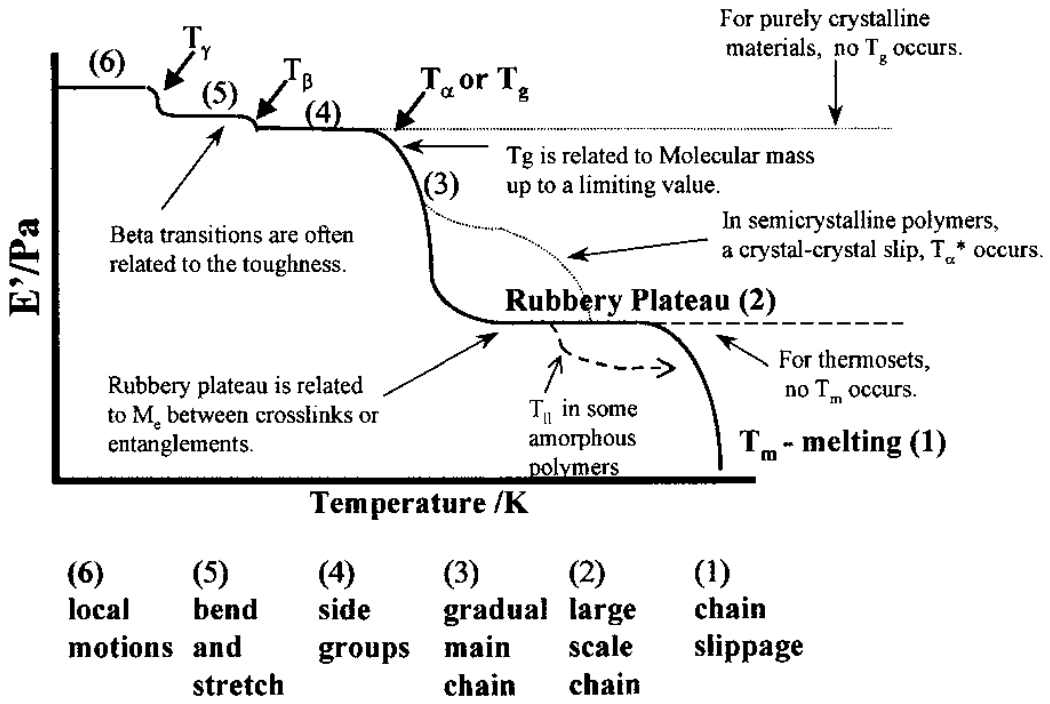

Figure 5.3: Ideal temperature scan of a polymer with DMA. From the low initial temperature, the modulus begins to decrease at the molecules gain more free volume. The curve is divided into six transition regions: (6) local motions, (5) bond bending and stretching, (4) movement of side chains, (3) the glass transition region, (2) coordinated movement in the amorphous portion of the chain, and (1) the melting region [71].

5.4 Possible Future Applications

5.4.1 Tensile Tester for Structural Characterization

With the lessons learned from this thesis, a tensile tester for testing 3D structures could developed. Using the same design process as Chapter 2, the load cell flexure bearings and thermal actuator could be sized to produce a mN range force with μN resolution. As mentioned in Section 5.2.1, the design and fabrication a 3D structure tensile tester was completed in this thesis. The fabricated device and 1 degree of freedom rotation bearing are shown in Figure 5.4. While the tester was not able to generate stress – strain

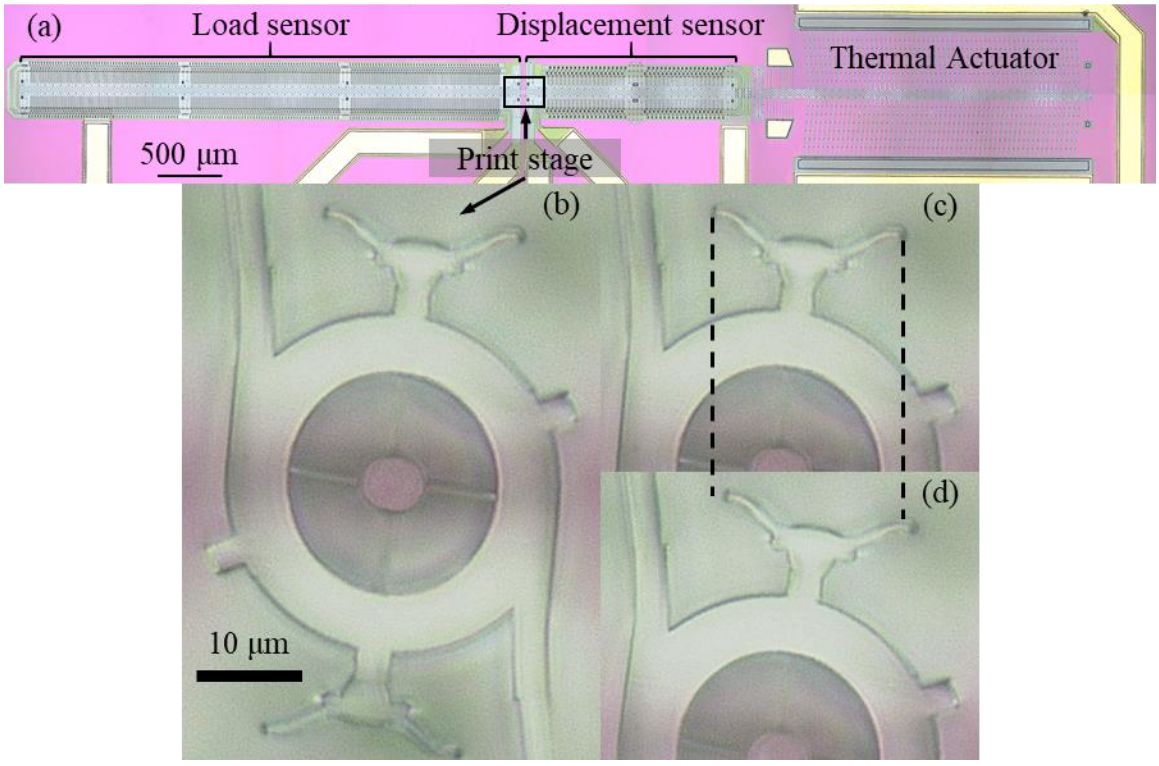

Figure 5.4: (a) MEMS tensile tester for 3D structures and (b) 1 degree of freedom rotation bearing.

data, it was still able to load the bearing and generate rotation motion shown in Figure 5.4.c-d.

With a few modifications to improve yield and part size, the 3D tester would be a valuable instrument for studying the different overlapping, or 'stitching', techniques required for millimeter scale parts. For large parts, it is common to write layer-by-layer with a defined vertical spacing, or slice, between layers and an in-plane spacing setting the voxel pitch. Both of these parameters can be used to modify density and writing time. With a 3D tester, a parametric study could be performed to capture the tradeoffs in structure properties and density/writing time as a function of different slicing heights and voxel

pitch. Similar to the speed test, this would result in trends that could be valuable for developing high throughput writing processes.

5.4.2 MEMS and TPP Integration

The MEMS integration with TPP demonstrated in this work could expand applications in both fields. For TPP, MEMS offers actuating and sensing techniques. Additional material and structural characterization instruments can be development. With an on-chip actuator, 3D structures, such as photonic crystals, could deformed under displacement controlled to change shape, or change the bandgap.

From a MEMS standpoint, TPP is an additively manufacturing process capable of writing 3D structures at and below traditional MEMS fabrication scale. With stiction analysis or modifications to the fabrication process, 3D structures could be used as a support structure for atomic layer deposition of sensing materials to increase the sensing surface area. A more direct and potentially impactful work is the integration of high strain 3D lattices as flexures and bearing to increase the range or tune the motion path of suspended structures. An example of a TPP 1 degree of freedom rotation bearing is shown in Figure 5.4.b-d.

5.5 CONCLUSIONS

This work provides a new material characterization method for TPP resists that captured speed and size effect of single voxel lines. High speed writing with UV post cure with radicals can increase throughput by 100x without decreasing material properties. Size effects were measured for elastic modulus, yield strength, and toughness below 450 nm with larger improvement below 300 nm. These results provide insight into the effects of degree-of-conversion and voxel size. However, future work still needed to utilize degree-

of-conversion to improve resist chemistry and examine potential mechanisms for the size effect, such as polymer alignment.

The characterization method integrated MEMS and TPP by adding a thorough stiction analysis and anti-stiction features to the tensile tester design. These steps are needed to prevent failure when exposed to the resist and liquids apart of the writing process. Consequently, the combination of fields could lead to future characterization instruments, tunable TPP structures, support structures for high surface area sensing, and TPP written flexures and bearing to increase displacement range or complex motion paths. Both material characterization and MEMS + TPP integration offer a wide range of valuable research.

Appendices

APPENDIX A: MICROFABRICATION MASKS

A.1 Poly 1 – Polysilicon structural and electrical base

Poly 1 is used to align the mask pattern to the wafer, define the structural and electrical base layers of each chip, and define the alignment features for the subsequent step. The full Poly 1 mask for a 5" mask is shown in Figure A.1. The features are centered onto a 100 mm wafer. Lines are patterned at the top and bottom of the white space to align with the minor and major flats. All of the tensile tester chips are located 1.58 mm from the edge to account for clamp rings in plasma etching processes. In this arrangement, each wafer produces 52 chips with 10 μm gaps between the load sensor and displacement sensor, 12 chips with 5 μm gaps, 12 chips with 2 μm gaps, and 4 chips with a 10 x 10 x 8 μm3 polysilicon beam connecting the two sensors. Six of the 2 μm and 5 μm chips have additional electrodes at the tips.

The Poly 1 pattern for a single chip is shown in Figure A.2. The thermal actuator located on the right side has two electrical base layers to connect the electrode to the thermal actuator beams and support structure for the heat sink beams. The sensors have three separate structures connecting the two sets of stationary capacitive fingers and the suspended shuttles. The central structure acts as capacitive plate below the stationary fingers. Additional features are located on the wafer above the octagon, the sensor tip coordinates, and the cross pattern to find the coordinates.

Alignment features for all of the subsequent photolithography steps, shown in Figure A.3, are also patterned on the Poly 1 layer. A simple cross and box approach is used for alignment. Four boxes and the mask number are patterned on the Poly 1 layer, and the corresponding cross and number outline are pattern on the remaining masks. The gaps

between the boxes range from 50 µm down to 10 µm for mask 1 – 2 and 5 µm masks 3 – 6 respectively.

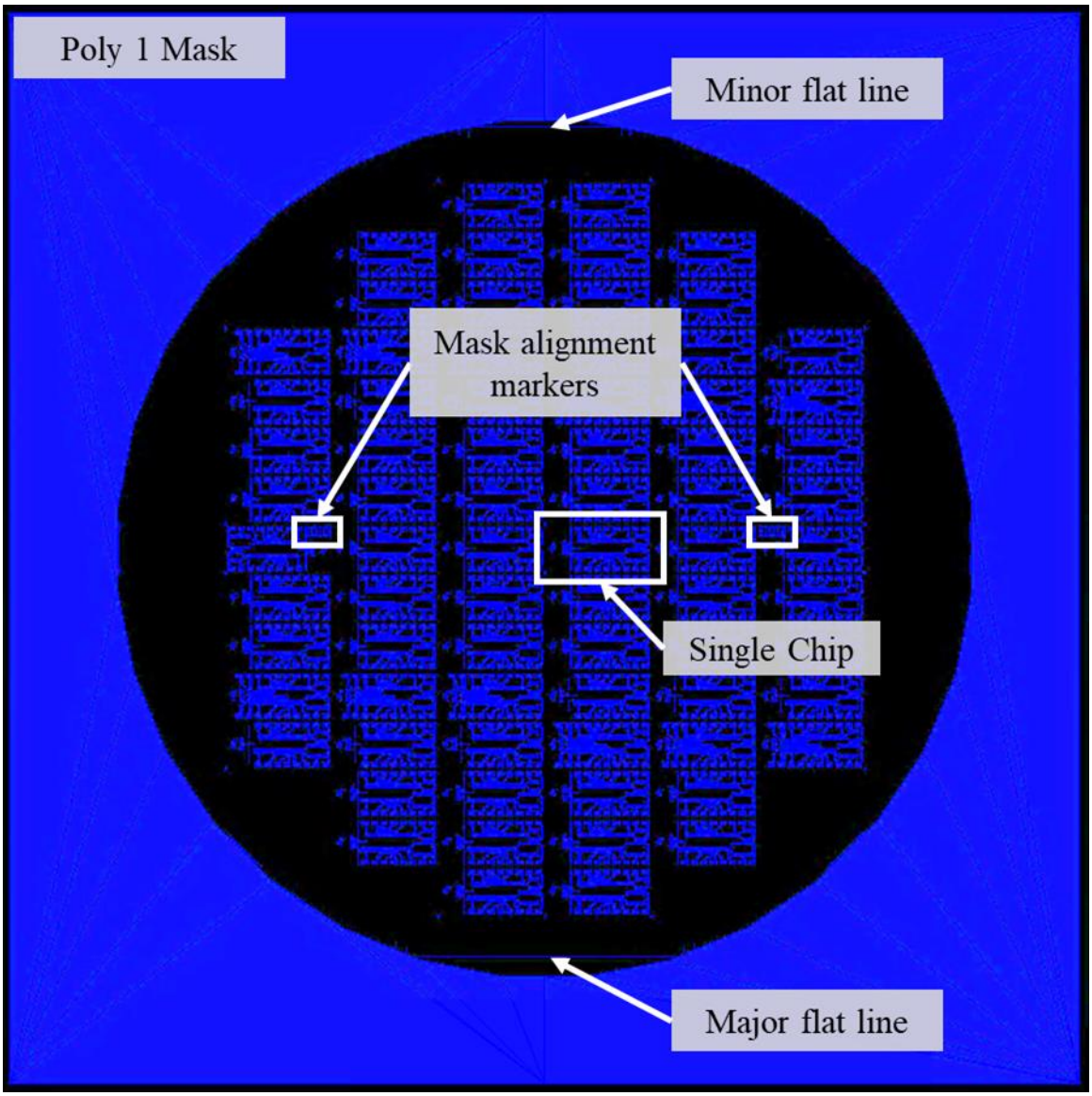

Figure A.1: Poly 1 mask defining the polysilicon base layer and aligning to the 100 mm wafer with the major and minor flats.

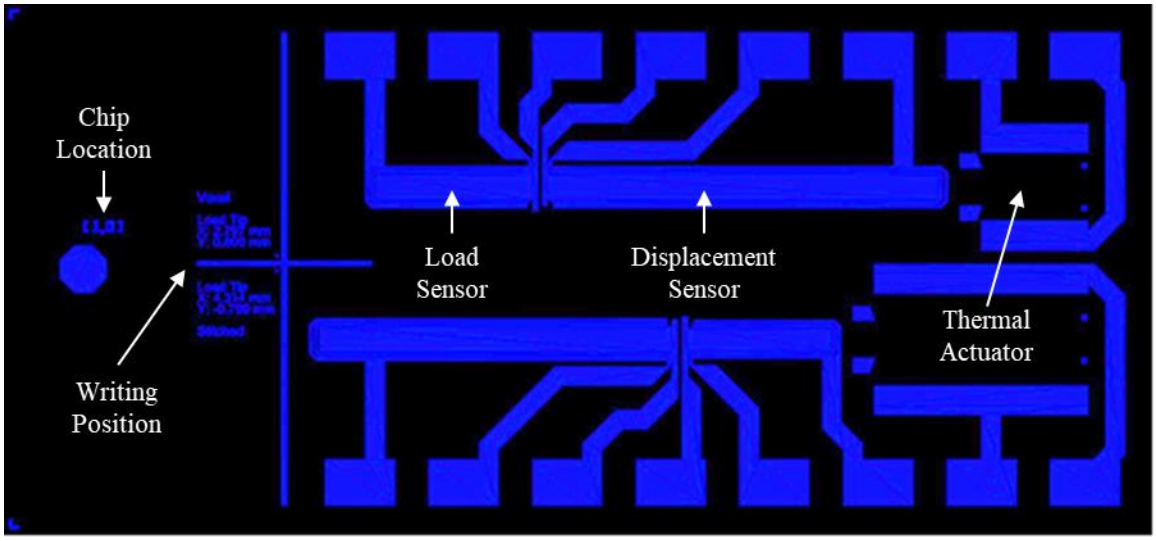

Figure A.2: Close up on a single chip.

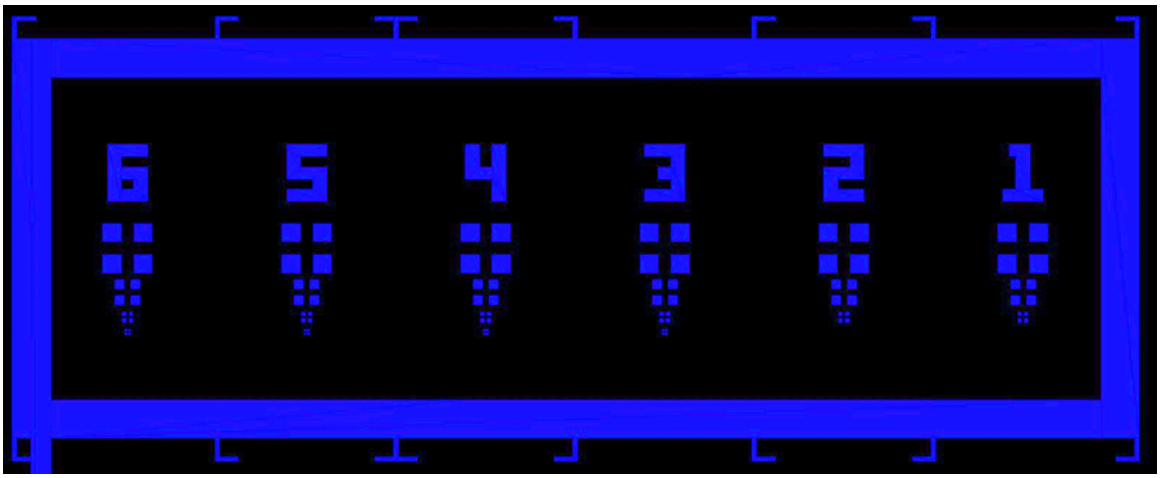

Figure A.3: Alignment features for subsequent masks.

A.2 Oxide 1 – Oxide planarization layer

Oxide 1 mask is used to define oxide structures to locally planarize features. The focus on this step is to form a 1 μm layer of oxide between the thermal actuator pads which matches the 1 μm layer of polysilicon under the capacitive sensor shuttle. A close up of an individual chip is shown in Figure A.4. The pattern is essentially the negative image of

Poly 1 with the addition of a 100 μm gap around the edge of each chip. This gap maps the cut path used during the dicing of the wafer. The cross and number outline alignment features are shown in Figure A.5. The box surrounding the alignment feature protects reference elements in the Poly 1 layer.

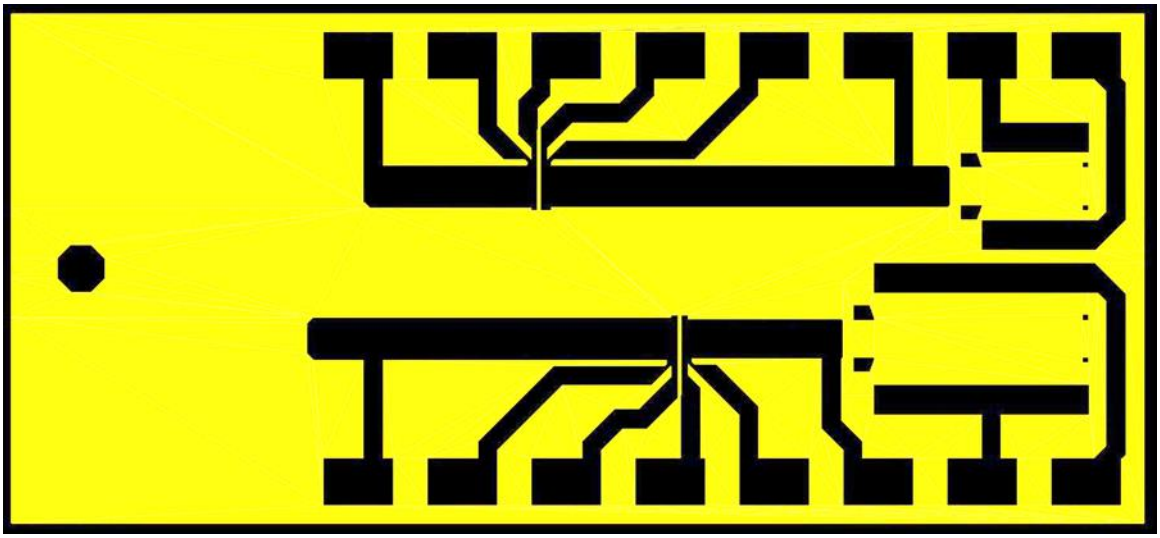

Figure A.4: Close up on a single chip.

Figure A.5: Alignment features for Oxide 1.

A.3 Oxide 2 – Oxide air gap

Oxide 2 mask creates the 2.5 µm air gap between the Poly 1 support layer and the Poly 2 device layer. The solid features shown in Figure A.6 are etched with a reactive ion etching (RIE) to form contact pads between the Poly 1 and Poly 2 layers. The pads are located at the base of every capacitive finger, the fixed position of the flexure bearings, the heat sink pads, and the electrodes. A negative mask is fabricated to allow for positive curing photoresist. The alignment feature in Figure A.7 includes a solid feature around the number and boxes that is converted into window to the substrate by the negative mask.

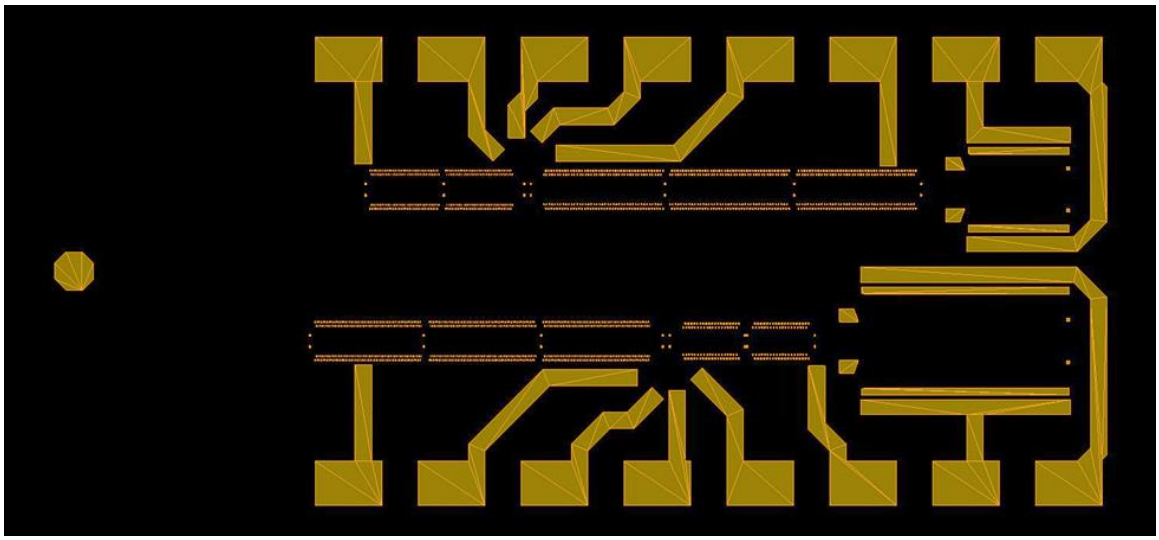

Figure A.6: Close up on the Oxide 2 mask of a single chip.

Figure A.7: Alignment features for Oxide 2.

A.4 Dimple – Dimple patterns

Dimple mask creates 2 x 2 μm^2 square patterns to form holes in the surface of Oxide 2. A wet etch forms 750 nm deep concave hemispheres, which are filled by the Poly 2 device layer to form the anti-stiction dimples. A single chip mask is shown in Figure A.8. The mask is converted into a negative of this file, similar to Oxide 2. The alignment feature uses the same approach as Oxide 2, but with mask number 3.

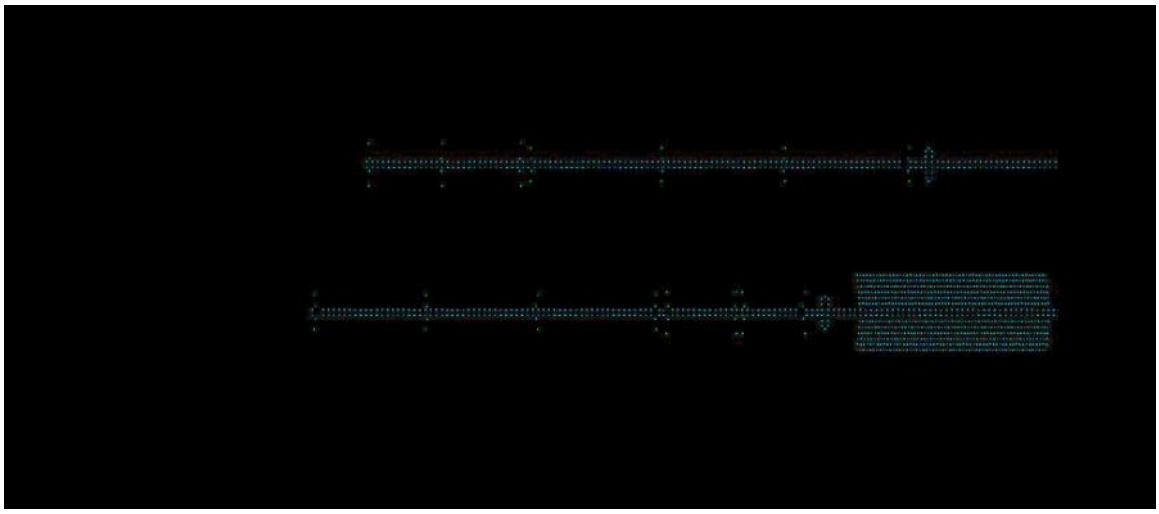

Figure A.8: Close up on the Dimple mask of a single chip.

A.5 Nitride 2 – Nitride insulation/adhesion layer

Nitride 2 mask defines electrical insulation and adhesion features along electrodes. Additionally, for the 12 total chips with electrodes at the sensor tips, the Nitride 2 layer insulates the electrode from the capacitive sensors. A standard chip mask is shown in Figure A.9. The number outline and cross alignment features are shown in Figure A.10. Unlike Poly 1, this mask does not require the additional box because the Oxide 1 and 2 are still protecting the reference features.

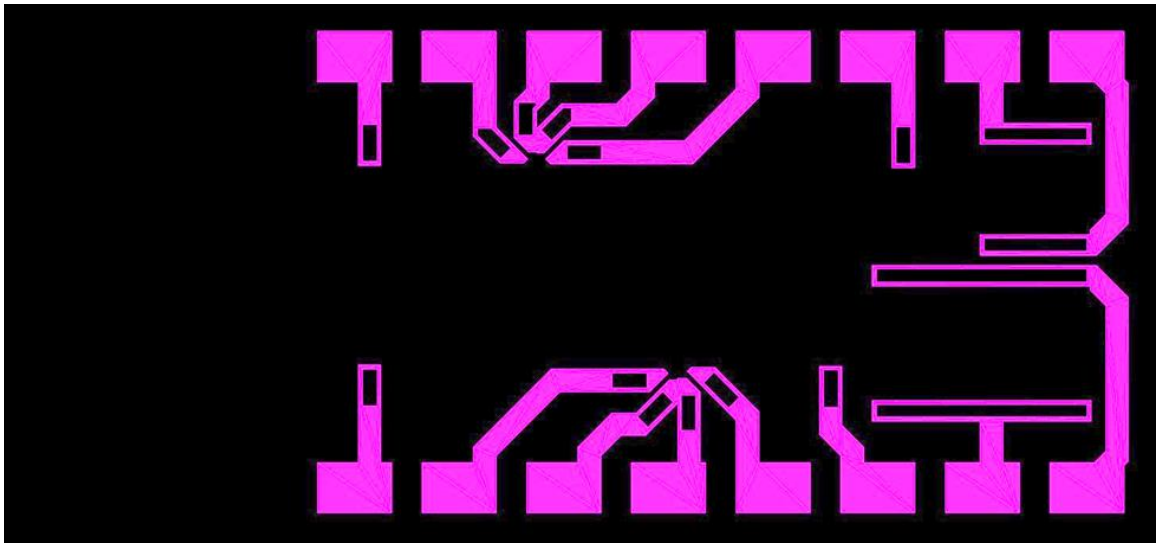

Figure A.9: Close up on Nitride 2 for a standard chip.

Figure A.10: Alignment features for Nitride 2.

A.6 Gold 1 – Gold metallization

Gold 1 mask uses a liftoff pattern to open areas on the electrodes and form electrical traces. Additional pads are placed at the heat sink for probing. A single chip mask is shown in Figure A.11, and the mask is converted to a negative like Oxide 2 and Dimples. The Oxide 2 alignment feature is also used, but with the mask number 5.

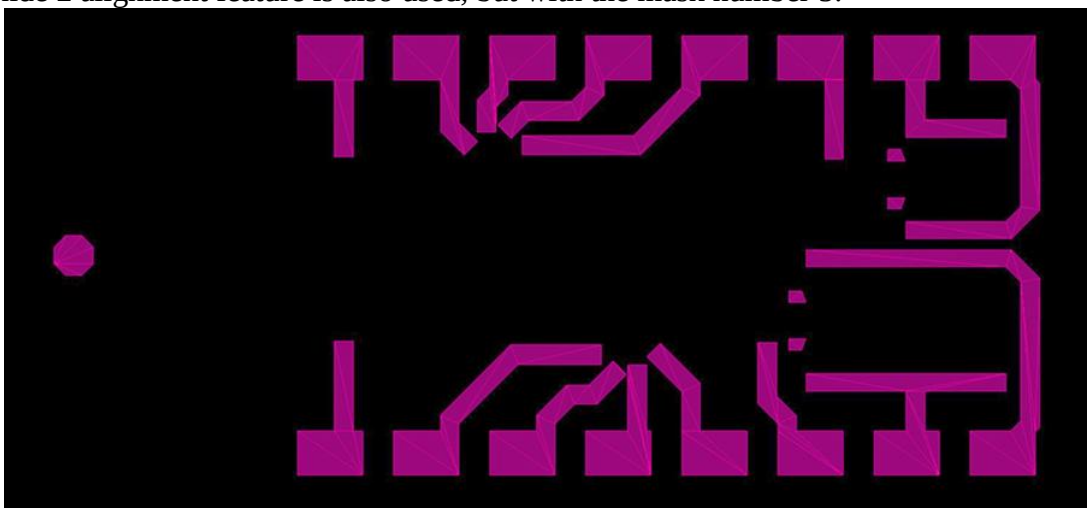

Figure A.11: Close up on Gold 1 for a single chip.

A.7 Poly 2 – Polysilicon device layer

Poly 2 mask is used to pattern the device layer and the suspended features of the tensile tester. This mask includes the thermal actuator beams, capacitive fingers, flexure bearings, shuttles, and final electrode profile. A close up of an individual chip is shown in Figure A.12. The alignment feature is the same style as Nitride 2 with a mask number 6.

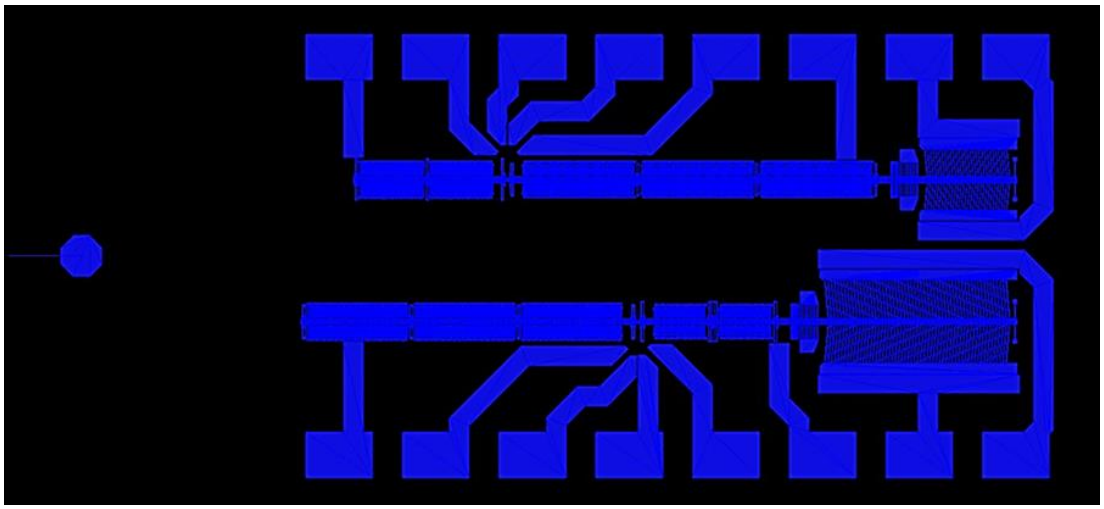

Figure A.12: Close up on Poly 2 for a single chip.

APPENDIX B: PCB PACKAGING

A custom printed circuit board (PCB) package was designed to improve the MEMS thermal management of the tensile tester. The PCB arrives from the supplier with perforated tabs around the edge, which need to removed and sanded flush. An image of the PCB package after sanding is shown in Figure B.1. Next, a piece of aluminum 4.2 x 12.3 x 1.6 mm^3 is adhered to the heat spreader location with epoxy resin. A tapper is sanded onto the bottom of the aluminum heat spreader to improve the seal made with the epoxy. Kapton tape is used to protect the alignment pin holes and SMD pads during this process. The epoxy is allowed 24 hours to cure before preparing to mount to tensile tester chip.

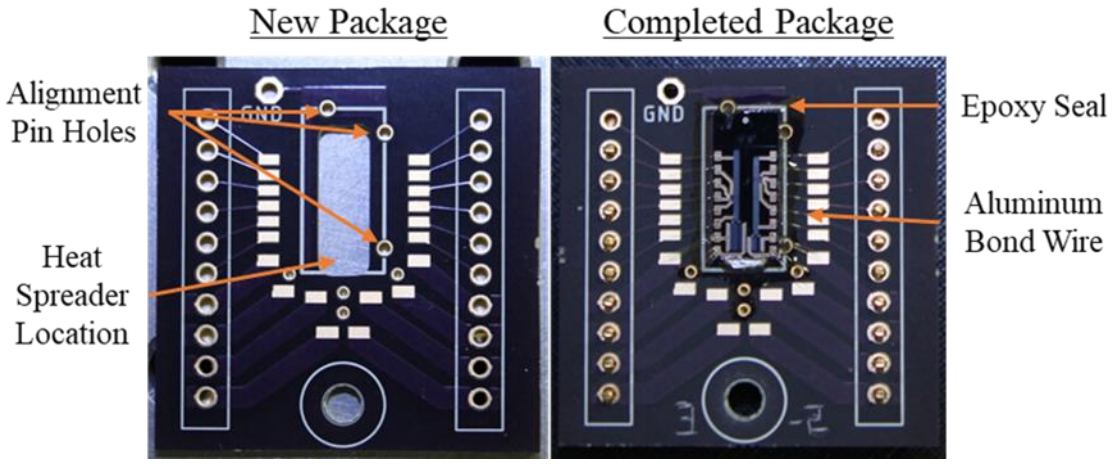

Figure B.1: A new PCB package on the left and a completed package on the right.

Excess epoxy and the Kapton tape are removed, and IPA is used to clean the surface of package. A thin layer of Artic MX-4 thermal paste is applied on top of the Al heat spreader to reduce the contact resistance between the base of the tensile tester chip and the top of the heat spreader. To further reduce the contact resistance, grooves are made in the backside of the chip with a diamond scribe. The package with thermal paste is loaded onto the 3D printed alignment jig with a single male header pins located above the chip location and two pins to the right. The chip is placed onto the thermal paste and moved around to spread and thin the paste. Next, the chip is slid into contact with the three alignment pins, and epoxy is added along the free edges of the chip. After 10 minutes, the chip and package pair are removed and the remaining edges are sealed. The alignment holes and vias near the chip are also filled to prevent thermal paste on the heat pipe from leaking through to the front, see Figure B.1.

Packaging is completed by wire bonding after letting the epoxy cure for at least 24 hours. Aluminum ball bonding is completed at Lawrence Livermore National Laboratory. All of the sensor pads are connected with one wire with an emphasis placed on placing

leads with similar lengths. 3 wires connect the thermal actuator electrode to the package to prevent damage during current loading.

APPENDIX C: FLEXURE BEARING MEASUREMENTS

The Keyence VK-X250 Laser Microscope was used to measure the length and width of the load cell flexure bearings. The 50x objective was used to measure the length, and the 100x objective was used for the flexure width. An example of both are presented in Figure C.1.a and b. For both scans, the expert laser scanning mode of the Keyence was used. In the laser intensity mode, the upper and lower planes were set above the top shuttle surface and below the base of the suspended features. The base was determined by scanning past the focal point on the nitride layer below the polysilicon base layer.

After the scan was complete, the profile measurement was extracted from the height map. Both are indicated in Figure C.1. There are two curves in the profile measurement that capture the height of the flexure beams with (green) and without (blue) the laser intensity. The length and width of the flexure beam were measured for both curves. The transition from low to high intensity was used for the green curve, and the transition from red to blue in the height map was used for the blue curve. Both have uncertainty, so the average value was selected for the length and width. In the width measurement, both beams in the image were measured. The recorded values for the devices used in this work are shown in Table C.1. The average values for the flexure beam length, L_{fb}, and beam width, b_{fb}, are 150 ± 1.1 µm and 4.7 ± 0.54 µm respectively. The designed values were 149.5 µm and 5 µm resulting in a deviation of < 1% for length and 6% for width.

The laser scan was also used to capture the variance in the vertical distance from the substrate. The result was ± 56 nm across 9 devices which span the 100 mm wafer. The height of the flexure beam, h_{fb}, was measured with SEM images of the shuttle tips, which

(a) Length

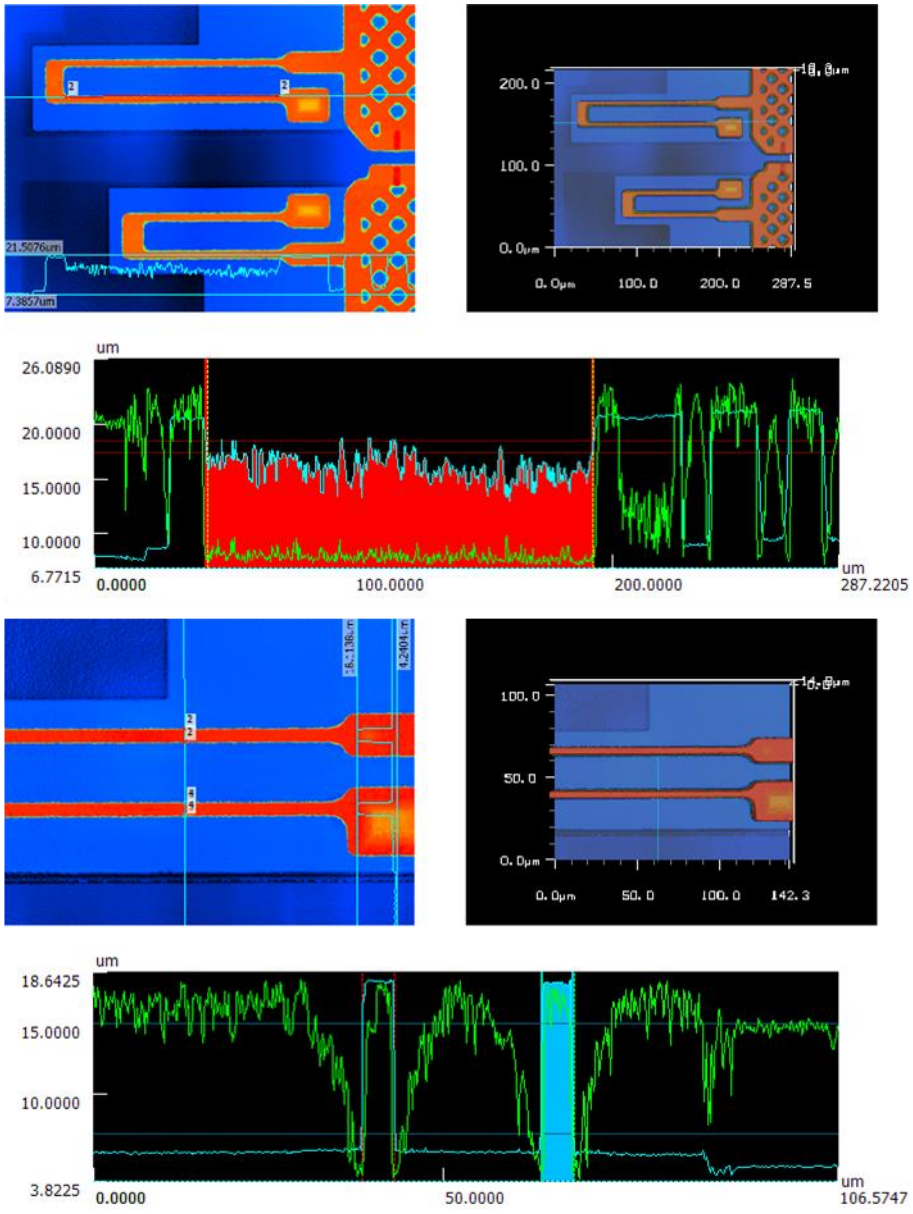

(b) Width

Figure C.1: Top view of a 2D and 3D height map with the profile measurement for the (a) flexure bearing length and (b) width. The profile measurement contains a blue curve based off of the height map and a green curve which accounts for the laser intensity.

offer better isolation for improved focusing as seen in Figure C.2. Using the SEM height and device variance from the laser scans, the average h_{fb} = 9.01 ± 0.06 µm. This is 1 µm larger than the designed value; however, the additional height provides extra out-of-plane stiffness to prevent stiction.

Device (#)	Length (µm)	Width (µm)	Height from surface (µm)
1	149.0	4.74	12.1
2	151.3	4.45	12.0
3	149.4	4.17	12.0
4	151.3	5.19	11.9
5	149.4	5.75	11.9
6	149.6	4.02	12.0
7	148.6	4.52	12.1
8	149.0	5.17	12.1
9	149.4	4.42	12.1
Average	150 ± 1.1	4.7 ± 0.54	12 ± 0.06

Table C.1: Summary of flexure bearing lengths, width, and height from substrate.

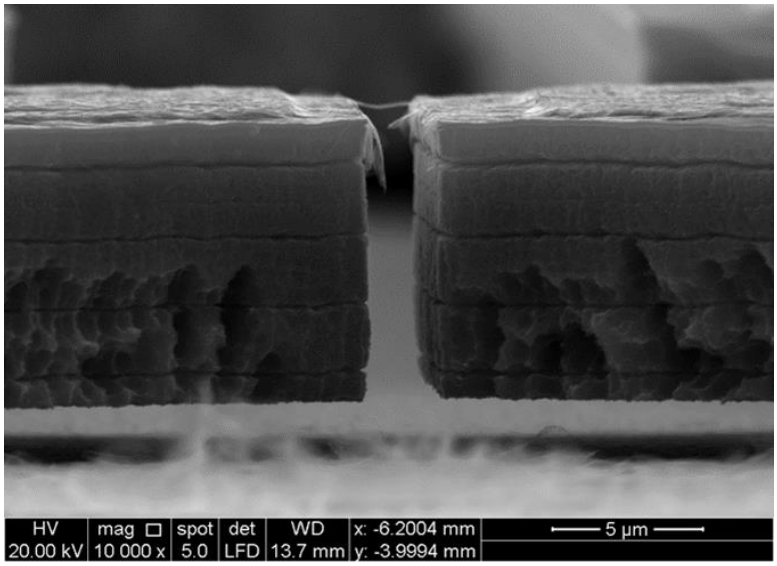

Figure C.2: SEM images of load and displacement shuttle tips.

APPENDIX D: MS3110 IC DIFFERENTIAL CAPACITANCE CALIBRATION

The MS3110 IC chips were calibrated using an evaluation board and without any sensors connected. First the reference voltage, V2P25, and current were adjusted to 2.25 ± 0.01 V and 10 ± 2 μA respectively using the Universal Capacitive Readout software from Irvine Sensors [67]. The last bias setting adjusted the oscillator frequency to 100 ± 10 kHz. After all the biases were set, two gain checks were conducted. The first gain check used a gain of 1 V/pF to determine the MS3110 chips were behaving properly. To produce the change in voltage, the on-chip capacitor CS1, see Figure 2.13, was adjusted while CS2 was fixed to generate a change in capacitance. All 5 chips produced gains within 10% of the desired 1 V/pF, which is within tolerance of Equation 2.29 when considering the ± 3.8 fF tolerance for each capacitor value.

The second gain check tuned the feedback capacitance and buffer gain in Equation 2.29 to produce 10 V/pf, or 1.0 mV/0.1 fF, gain. This is the gain selected for testing the load and displacement sensors. Figure D.1.a and D.1.b presents change in voltage versus the change in capacitance curves for a positive and negative gain for two different evaluation boards and chips to simulate sensing on both sensors. The resulting gains are 9.2 ± 0.002 V/pF and -9.27 ± 0.001 V/pF. Again, these values are within tolerance.

With the chips and boards calibrated, double shielded jumper wire connected the tensile tester sensors to the evaluation boards. After an initial adjustment of CS1 and CS2 to balance the circuit, the same gain check was conducted for the load sensor. The gain decreased to an average of 6.58 ± 0.72 V/pF across three tensile testers. The curves are plotted in in Figure D.2, which is a 28% decrease from the check without connecting to the tensile tester. The shift initially was related to possible leakage or noise in the circuit. Next, the displacement sensor was connected to the MS3110 IC evaluation board, but the signal was saturated across all values of CS1 and CS2.

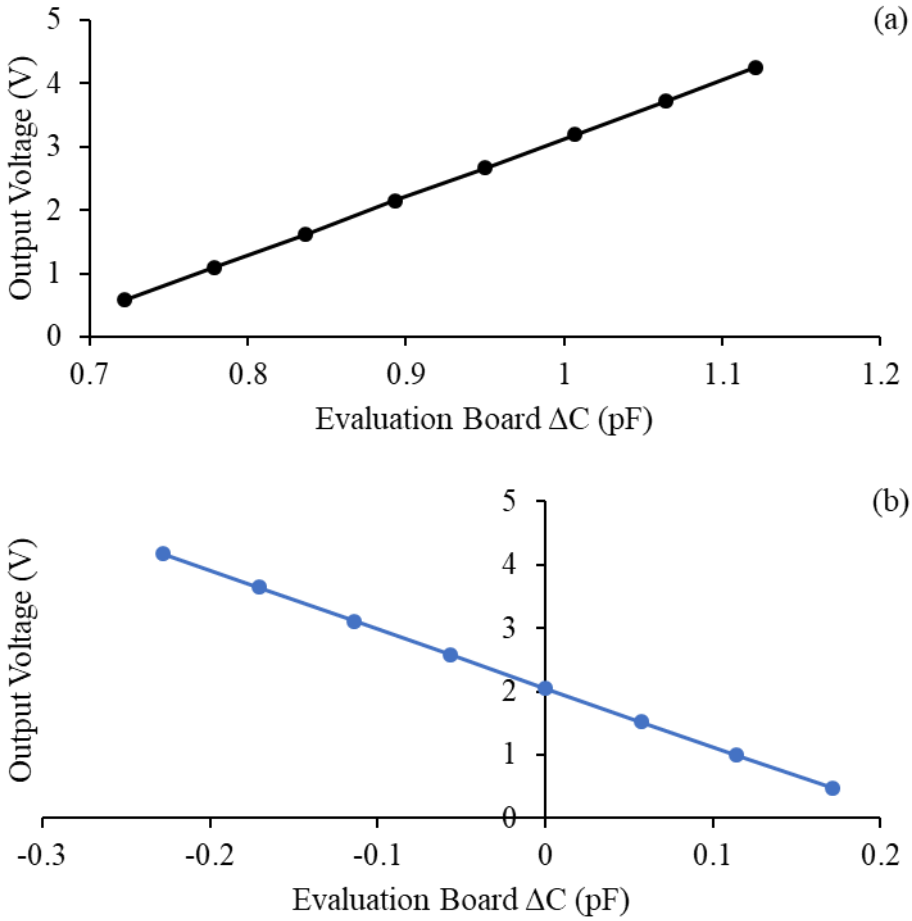

Figure D.1: (a) Positive gain and (b) negative gain curves from the MS3110 IC chips.

With the appearance of a saturated signal, the individual capacitance values were measured. A SMD Smart probe with pF resolution measured capacitance values of *70 - 90 pF* for the load sensor and *170 - 200 pF* for the displacement sensor. Those values are almost two orders of magnitude greater than the design values and greatly exceed the 10pF input sensing capacitance range of the MS3110 IC.

Interestingly, even with capacitance values 7 to 9 times greater than the limit on the IC, the load sensor was not saturated. The calibration tensile tester, which has a polysilicon

connection across the tips, was used to investigate if the output of the MS3110 IC would match the gain for the on-chip test. Step voltages were applied to the thermal actuator to change the capacitance of the load sensor. However, the output voltage measured in LabVIEW did not change over a 1.5 μm displacement range.

To determine if this behavior is based on the device or the MS3110 IC, the SMD smart probe was used to measure the capacitance during actuation. The 1 pF resolution probes were able to capture $\Delta C_1 \approx 1\ pF$. This result demonstrated the capacitors were changing, and the signal in Figure D.2 was an artifact of variations in the tuning capacitors. At this point, DIC was selected as the sensing method due to time and resolution in the sub 2.2 nm range.

References

[1] M. Deubel, G. von Freymann, M. Wegener, S. Pereira, K. Busch, and C. M. Soukoulis, "Direct laser writing of three-dimensional photonic-crystal templates for telecommunications," *Nat. Mater.*, vol. 3, no. 7, pp. 444–447, 2004.

[2] L. R. Meza, S. Das, and J. R. Greer, "Strong, lightweight, and recoverable three-dimensional ceramic nanolattices," *Science (80-.).*, vol. 345, no. 6202, pp. 1322–1326, 2014.

[3] J. Bauer, a. Schroer, R. Schwaiger, and O. Kraft, "Approaching theoretical strength in glassy carbon nanolattices," *Nat. Mater.*, vol. 15, no. 4, pp. 438–443, 2016.

[4] J. Bauer *et al.*, "Push-to-pull tensile testing of ultra-strong nanoscale ceramic-polymer composites made by additive manufacturing," *Extrem. Mech. Lett.*, vol. 3, pp. 105–112, 2015.

[5] M. M. Stevens and J. H. George, "Exploring and Engineering the Cell Surface Interface," *Science (80-.).*, vol. 310, pp. 1135–1138, 2005.

[6] S. J. Zhang *et al.*, "Controlling Young's modulus of polymerized structures fabricated by direct laser writing," *Appl. Phys. A Mater. Sci. Process.*, vol. 118, no. 2, pp. 437–441, 2014.

[7] D. Jang, L. R. Meza, F. Greer, and J. R. Greer, "Fabrication and deformation of three-dimensional hollow ceramic nanostructures," *Nat. Mater.*, vol. 12, no. 10, pp. 893–898, 2013.

[8] K. Cicha, T. Koch, J. Torgersen, Z. Li, R. Liska, and J. Stampfl, "Young's modulus measurement of two-photon polymerized micro-cantilevers by using nanoindentation equipment," *J. Appl. Phys.*, vol. 112, no. 9, 2012.

[9] S. K. Saha, C. Divin, J. a. Cuadra, and R. M. Panas, "Effect of Proximity of Features on the Damage Threshold During Submicron Additive Manufacturing Via Two-Photon Polymerization," *J. Micro Nano-Manufacturing*, vol. 5, no. 3, p. 031002, 2017.

[10] H. D. Espinosa, Y. Zhu, and N. Moldovan, "Design and operation of a MEMS-based material testing system for in-situ electron microscopy testing of nanostructures," *J. Microelectromech. S.*, vol. 16, no. 5, p. 1231, 2007.

[11] D. Zhang, W. Drissen, J.-M. Breguet, R. Clavel, and J. Michler, "A high-sensitivity and quasi-linear capacitive sensor for nanomechanical testing applications," *J. Micromech. Microeng. J. Micromech. Microeng*, vol. 19, no. 19, pp. 75003–10, 2009.

[12] M. Naraghi, T. Ozkan, I. Chasiotis, S. S. Hazra, and M. P. de Boer, "MEMS platform for on-chip nanomechanical experiments with strong and highly ductile nanofibers," *J. Micromech. Microeng.*, vol. 20, no. 12, p. 125022, 2010.

[13] Y. Zhu and T.-H. Chang, "A review of microelectromechanical systems for nanoscale mechanical characterization," *J. Micromechanics Microengineering*, vol. 25, no. 9, p. 093001, 2015.

[14] L. J. Jiang *et al.*, "Two-photon polymerization: investigation of chemical and

mechanical properties of resins using Raman microspectroscopy.," *Opt. Lett.*, vol. 39, no. 10, pp. 3034–7, 2014.
[15] D. S. Gianola and C. Eberl, "Micro- and nanoscale tensile testing of materials," *Jom*, vol. 61, no. 3, pp. 24–35, 2009.
[16] H. Gao, B. Ji, I. L. Jager, E. Arzt, and P. Fratzl, "Materials become insensitive to flaws at nanoscale: Lessons from nature," *Proc. Natl. Acad. Sci.*, vol. 100, no. 10, pp. 5597–5600, 2003.
[17] D. Zhang, "A Nano-Tensile Testing System for Studying Nanostructures inside an Electron Microscope : Design , Characterization and Application," 2010.
[18] J. S. Oakdale *et al.*, "Direct Laser Writing of Low-Density Interdigitated Foams for Plasma Drive Shaping," *Adv. Funct. Mater.*, vol. 27, no. 43, pp. 1–10, 2017.
[19] L. J. Jiang, J. H. Campbell, Y. F. Lu, T. Bernat, and N. Petta, "Direct writing target structures by two-photon polymerization," *Fusion Sci. Technol.*, vol. 70, no. 2, pp. 295–309, 2016.
[20] X. Zhou, Y. Hou, and J. Lin, "A review on the processing accuracy of two-photon polymerization," *AIP Adv.*, vol. 5, no. 3, 2015.
[21] A. Spangenberg *et al.*, "Recent Advances in Two-Photon Stereolithography," *Intech*, vol. 6, pp. 111–133, 2013.
[22] S. Wu, J. Serbin, and M. Gu, "Two-photon polymerisation for three-dimensional micro-fabrication," *J. Photochem. Photobiol. A Chem.*, vol. 181, no. 1, pp. 1–11, 2006.
[23] J. S. Oakdale, J. Ye, W. L. Smith, and J. Biener, "Post-print UV curing method for improving the mechanical properties of prototypes derived from two-photon lithography," *Opt. Express*, vol. 24, no. 24, pp. 186–194, 2016.
[24] C. N. LaFratta and T. Baldacchini, "Two-photon polymerization metrology: Characterization methods of mechanisms and microstructures," *Micromachines*, vol. 8, no. 4, 2017.
[25] A. Schroer, J. Bauer, R. Schwaiger, and O. Kraft, "Optimizing the mechanical properties of polymer resists for strong and light-weight micro-truss structures," *Extrem. Mech. Lett.*, vol. 8, pp. 283–291, 2016.
[26] R. K. Jayne, T. J. Stark, J. B. Reeves, D. J. Bishop, and A. E. White, "Dynamic Actuation of Soft 3D Micromechanical Structures Using Micro-Electromechanical Systems (MEMSs)," *Adv. Mater. Technol.*, vol. 1700293, pp. 1–6, 2018.
[27] A. M. Yu *et al.*, "Linked references are available on JSTOR for this article : Strength and Breaking Mechanism of Multiwalled Carbon Nanotubes Under Tensile Load," vol. 287, no. 5453, pp. 637–640, 2016.
[28] S. Hoffmann *et al.*, "Fracture strength and Young's modulus of ZnO nanowires," *Nanotechnology*, vol. 18, no. 20, 2007.
[29] T. Tsuchiya, Y. Ura, K. Sugano, and O. Tabata, "Electrostatic tensile testing device with nanonewton and nanometer resolution and its application to C 60 nanowire testing," *J. Microelectromechanical Syst.*, vol. 21, no. 3, pp. 523–529, 2012.
[30] M. Yilmaz and J. W. Kysar, "Monolithic integration of nanoscale tensile

specimens and MEMS structures," *Nanotechnology*, vol. 24, no. 16, 2013.
[31] S. Nakanishi, S. Shoji, S. Kawata, and H. B. Sun, "Giant elasticity of photopolymer nanowires," *Appl. Phys. Lett.*, vol. 91, no. 6, pp. 10–13, 2007.
[32] O. Kraft, P. a. Gruber, R. Mönig, and D. Weygand, "Plasticity in Confined Dimensions," *Annu. Rev. Mater. Res.*, vol. 40, no. 1, pp. 293–317, 2010.
[33] T. Zhu and J. Li, "Ultra-strength materials," *Prog. Mater. Sci.*, vol. 55, no. 7, pp. 710–757, 2010.
[34] W. Kang, J. Rajagopalan, and M. T. A. Saif, "In Situ Uniaxial Mechanical Testing of Small Scale Materials—A Review," *Nanosci. Nanotechnol. Lett.*, vol. 2, no. 4, pp. 282–287, 2010.
[35] Y. Zhu and H. D. Espinosa, "An electromechanical material testing system for in situ electron microscopy and applications.," *Proc. Natl. Acad. Sci. U. S. A.*, vol. 102, no. 41, pp. 14503–8, 2005.
[36] Z. Yong, L. Xinyu, R. Changhai, Z. Yan Liang, D. Lixin, and S. Yu, "Piezoresistivity Characterization of Synthetic Silicon Nanowires Using a MEMS Device," *J. Microelectromechanical Syst.*, vol. 20, no. 4, pp. 959–967, 2011.
[37] B. Pant, B. L. Allen, T. Zhu, K. Gall, and O. N. Pierron, "A versatile microelectromechanical system for nanomechanical testing," *Appl. Phys. Lett.*, vol. 98, no. 5, pp. 5–8, 2011.
[38] E. Hosseinian and O. N. Pierron, "Quantitative in situ TEM tensile fatigue testing on nanocrystalline metallic ultrathin films," *Nanoscale*, vol. 5, no. 24, pp. 12532–12541, 2013.
[39] J. H. Han and M. T. a Saif, "In situ microtensile stage for electromechanical characterization of nanoscale freestanding films," *Rev. Sci. Instrum.*, vol. 77, no. 4, 2006.
[40] M. Kiuchi, S. Matsui, and Y. Isono, "Mechanical characteristics of FIB deposited carbon nanowires using an electrostatic actuated Nano Tensile testing device," *J. Microelectromechanical Syst.*, vol. 16, no. 2, pp. 191–201, 2007.
[41] Y. Zhu, A. Corigliano, and H. D. Espinosa, "A thermal actuator for nanoscale *in situ* microscopy testing: design and characterization," *J. Micromechanics Microengineering*, vol. 16, no. 2, pp. 242–253, 2006.
[42] Y. Zhu, N. Moldovan, and H. D. Espinosa, "A microelectromechanical load sensor for in situ electron and x-ray microscopy tensile testing of nanostructures," *Appl. Phys. Lett.*, vol. 86, no. 1, 2005.
[43] G. Cheng, T. H. Chang, Q. Qin, H. Huang, and Y. Zhu, "Mechanical properties of silicon carbide nanowires: Effect of size-dependent defect density," *Nano Lett.*, vol. 14, no. 2, pp. 754–758, 2014.
[44] S. Krödel, L. Li, A. Constantinescu, and C. Daraio, "Stress relaxation in polymeric microlattice materials," *Mater. Des.*, vol. 130, no. April, pp. 433–441, 2017.
[45] P. J. French, "Polysilicon : a versatile material for microsystems," *Sensors and Actuators*, vol. 99, no. A, pp. 3–12, 2002.
[46] J. Ouyang and Y. Zhu, "Z-shaped MEMS thermal actuators: Piezoresistive self-sensing and preliminary results for feedback control," *J. Microelectromechanical*

Syst., vol. 21, no. 3, pp. 596–604, 2012.
[47] I. S. Ladner, J. H. Cho, D. R. Cayll, V. H. Nguyen, M. A. Cullinan, and S. K. Saha, "Mechanical Characterization of Additively Manufactured Microstructures Using a Process Integrated Mems Tensile Tester," no. 0097, pp. 269–271, 2018.
[48] C. H. Mastrangelo and C. H. Hsu, "A simple experimental technique for the measurement of the work of adhesion of microstructures," *Technical Digest IEEE Solid-State Sensor and Actuator Workshop*. pp. 208–212, 1992.
[49] O. Raccurt, F. Tardif, F. a d'Avitaya, and T. Vareine, "Influence of liquid surface tension on stiction of SOI MEMS," *J. Micromechanics Microengineering*, vol. 14, no. Copyright 2004, IEE, pp. 1083–1090, 2004.
[50] N. Tas, T. Sonnenberg, H. Jansen, R. Legtenberg, and M. Elwenspoek, "Stiction in surface micromachining," *J. Micromechanics Microengineering*, vol. 6, no. 4, pp. 385–397, 1996.
[51] *Chapter 2 PolyMUMPs Design Guidelines and Rules*, Rev. 13.0., vol. 1. .
[52] ASTM D 638 -02a, "Standard test method for tensile properties of plastics," *ASTM D 638 -02a*, vol. 08, pp. 46–58, 2003.
[53] M. Naraghi, I. Chasiotis, H. Kahn, Y. Wen, and Y. Dzenis, "Novel method for mechanical characterization of polymeric nanofibers," *Rev. Sci. Instrum.*, vol. 78, no. 8, pp. 0–7, 2007.
[54] G. Sun, J. H. Cho, and M. Cullinan, "A Method to Manufacture Repeatible Graphene-Based NEMS Devices at the Wafer-Scale," *Proc. ASME 2016 Int. Manuf. Sci. Eng. Conf.*, pp. MSEC2016-8567, 2016.
[55] P. J. French and A. G. R. Evans, "PIEZORESISTANCE IN POLYSILICON AND ITS APPLICATIONS TO STRAIN GAUGES," *Solid. State. Electron.*, vol. 32, no. 1, pp. 1–10, 1989.
[56] Z. Yapu, "Stiction and anti-stiction in MEMS and NEMS," *Acta Mech. Sin.*, vol. 19, no. l, pp. 1–10, 2003.
[57] M. S. Baker, R. A. Plass, T. J. Headley, and J. A. Walraven, "Final Report : Compliant Thermo- Mechanical MEMS Actuators LDRD # 52553," 2004.
[58] Q. Huang, N. Ka, and S. Lee, "Analysis and design of polysilicon thermal flexure actuator," *J. Micromech. Microeng.*, vol. 9, pp. 63–70, 1999.
[59] D. A. (David A. Reay, P. A. (Peter A. . Kew, and P. D. (Peter D. . Dunn, *Heat pipes.*, 5th ed. Oxford: Butterworth-Heinemann, 2006.
[60] M. F. Pantano, R. A. Bernal, L. Pagnotta, and H. D. Espinosa, "Multiphysics design and implementation of a microsystem for displacement-controlled tensile testing of nanomaterials," *Meccanica*, vol. 50, no. 2, pp. 549–560, 2015.
[61] T. Universal and C. Readout, "MS3110 Universal Capacitive Readout TM IC," 2001.
[62] Filmtronics, "SPIN-ON DIFFUSANTS," no. July, pp. 1–51, 2004.
[63] F. Klein *et al.*, "Elastic fully three-dimensional microstructure scaffolds for cell force measurements," *Adv. Mater.*, vol. 22, no. 8, pp. 868–871, 2010.
[64] J. Lee, T. Beechem, T. L. Wright, B. A. Nelson, S. Graham, and W. P. King, "Electrical, thermal, and mechanical characterization of silicon microcantilever

heaters," *J. Microelectromechanical Syst.*, vol. 15, no. 6, pp. 1644–1655, 2006.
[65] B. W. Chui, M. Asheghi, Y. S. Ju, K. E. Goodson, T. W. Kenny, and H. J. Mamin, "Intrinsic-carrier thermal runaway in silicon microcantilevers," *Microscale Thermophys. Eng.*, vol. 3, no. 3, pp. 217–228, 1999.
[66] V. a Henneken, M. Tichem, and P. M. Sarro, "In-package MEMS-based thermal actuators for micro-assembly," *J. Micromechanics Microengineering*, vol. 16, no. 6, pp. S107–S115, 2006.
[67] M. Q. S. Guide, "Quick Start Guide Quick Start Guide for MS3110BDPC-USB Operation and Installation September 26 , 2012 Quick Start Guide," 2012.
[68] M. Ehmann, P. Ruther, M. von Arx, and O. Paul, "Operation and short-term drift of polysilicon-heated CMOS microstructures at temperatures up to 1200 K," *J. Micromech. Microeng.*, vol. 11, pp. 397–401, 2001.
[69] S. Ushiba, K. Masui, N. Taguchi, T. Hamano, S. Kawata, and S. Shoji, "Size dependent nanomechanics of coil spring shaped polymer nanowires," *Sci. Rep.*, vol. 5, pp. 1–5, 2015.
[70] P. Prabhakaran, Y. Son, C. W. Ha, J. J. Park, S. Jeon, and K. S. Lee, "Optical Materials Forming Tightly Polymerized Voxels during Laser Direct Writing," *Adv. Eng. Mater.*, vol. 20, no. 10, pp. 1–13, 2018.
[71] K. Menard, *Dynamic mechanical analysis: a practical introduction*. 2008.